# Novel Nano-Structured Silicon and $Co_3O_4$ Materials as Anode for High-Performance Lithium Ion Batteries

by

Kun Feng

A thesis

presented to the University of Waterloo

in fulfillment of the

thesis requirement for the degree of

Master of Applied Science

in

Chemical Engineering - Nanotechnology

Waterloo, Ontario, Canada, 2014

## Author’s declaration:

I hereby declare that I am the sole author of this thesis. This is a true copy of the thesis, including any required final revisions, as accepted by my examiners.

I understand that my thesis may be made electronically available to the public.

## Abstract:

Lithium ion batteries (LIBs) play an essential role in modern life. Although relatively unknown throughout past decades, LIBs have supplanted several categories of chemically rechargeable batteries including lead-acid, nickel-cadmium and nickel-hydrogen batteries. Nowadays, LIBs dominate the market of portable electronic devices such as mobile phones, digital cameras and laptops. As the price of petroleum keeps increasing, electrically powered or assisted vehicles using LIBs are similarly gaining in the automotive market. However, current state-of-art LIBs using graphite as their electrical anode and Li metal oxides as the cathode are facing major challenges. For example, the current LIBs are approaching their capacity limit. Batteries that can maintain high charge and discharge rates are in great demand, which has not been adequately addressed by modern LIBs. Safety issues with these current batteries are being reported even from some market leaders such as Boeing and Tesla.

Herein, several categories of novel anode materials have been investigated in a search for promising candidates to enable evolution of the next generation of lithium ion batteries. This research included silicon-carbon based materials, especially silicon-graphene (Si-G) materials and their derivatives, and transitional metal based materials, *e.g.*, cobalt oxide ($Co_3O_4$).

In this proposed work, Si-G composites were synthesized via a freeze-drying method; the conditions of the synthesis were controlled and adjusted to obtain a Si-G composite with the most promising morphology as well as battery performance. Based on preliminary results, graphene wrapped silicon electrodes showed significantly improved cycling performance than bare silicon electrodes. At high charge and discharge rates it was found that Si-G composites also showed superior stability and capacity retention over bare silicon electrodes. After 200 cycles, the optimized Si-G composite maintained a capacity retention close to 100%, with a capacity of

800 mAh $g^{-1}$ at a 0.2 C rate and 600 mAh $g^{-1}$ at a 1 C rate. This observation was a prominent increase from the performance of commercial graphite-based batteries at a theoretical capacity 372 mAh $g^{-1}$. Considering the facile fabrication method and increasing use of commercial silicon nano-particles (Si-NPs) into account, Si-G composites could be a promising candidate for the anode material in LIBs. Extended work on the Si-G project also involved further decorations based on the Si-G composite synthesized from the method previously mentioned, as well as improvement on the synthesis method to make it more applicable for industrial purposes.

Cobalt Oxide ($Co_3O_4$), a transitional metal oxide which has a theoretical capacity of 890 mAh $g^{-1}$, draws attention as an anode material in LIBs due to its capacity compared to graphite and heavily reduced degradation compared to silicon. A novel electrode fabrication procedure was adopted in this research together with a simple material-synthesizing methodology. Similar to common silicon electrodes, $Co_3O_4$ suffers from poor electron conductivity volume change upon cycling. Herein the $Co_3O_4$ active material is directly deposited on stainless steel mesh, serving as both a current collector and a substrate for the active material. Through adapting the electrode fabrication process by directly depositing on the stainless steel electron conductor, the traditional conductive carbon material and binder requirements can be avoided. As a result, the process is reduced in both cost and complexity. The presented novel electrode design facilitates both ion diffusion and electron transportation, improving the overall performance of the material in LIBs. After 100 cycles of charge and discharge, $Co_3O_4$ on stainless steel mesh shows a capacity around 770 mAh $g^{-1}$, which is more than twice that of graphite. The capacity retention was around 90% in this case.

## Acknowledgements:

The work reported herein was financially supported by General Motors Global Research & Development Center, Natural Sciences and Engineering Research Council of Canada, Waterloo Institute for Nanotechnology, and the University of Waterloo.

The author would like to thank Dr. Zhongwei Chen, and Dr. Aiping Yu for their meticulous guidance and tremendous assistance in the Master's study.

Many thanks go to author's colleagues including, Heywoong Park, Drew Higgins, Fathy Hassan, Hadis Zarrin, Qianqian Hu, Moon Gyu Park, Rongyue Wang, Ja-Yeon Choi, Vuqar Ismayilov, Ariful Hoque, Siamak Ghorbani, Yun-seok Jun, Jared Lenos, Jason Wu, Dongun Lee, Gaopeng Jiang, Rasim Batmaz, Raihan Ahmed, Abdul Rahman Ghannoum, Abel Sy, Gregory Lui, Jinyun Liao, Brian Kim, Joseph Kim, Xiaolei Wang, Abdel Rahman Elsayed, Guihua Liu, Victor Chabot, Min Ho Seo, Pouyan Zamani, Salah Abureden, Zhiyu Mao and many other friends for their assistance and support.

I would also like to thank my great parents, Qichuan Feng and Xingxiang Wu for their consistent love and support for me. They provide every single possibility for whatever I have achieved so far.

Moreover I would like to acknowledge support from my reviewers, including Professor Zhongwei Chen, Professor Aiping Yu, and Professor Yuning Li.

# Table of Contents

# List of Figures

# List of Tables

## List of Abbreviations, Symbols and Nomenclature

| | |
|---|---|
| LIBs | Lithium ion batteries |
| SEM | Scanning Electron Microscopy |
| TEM | Transmission Electron Microscopy |
| XRD | X-ray Diffraction |
| TGA | Thermal Gravimetric Analysis |
| CNT | Carbon nanotube |
| SWNT | Single-walled carbon nanotube |
| CVD | Chemical vapour deposition |
| EDAX | Energy dispersive X-ray spectroscopy |
| SAED | Selected area electron diffraction |
| FTIR | Fourier transform infrared spectroscopy |
| BET | Brunauer–Emmett–Teller |
| CV | Cyclic voltammetry |
| EIS | Electrochemical impedance spectroscopy |
| NMP | N-Methyl-2-pyrrolidone |
| PVDF | Polyvinylidene fluoride |

| | |
|---|---|
| Si-G | Silicon graphene |
| NW | Nanowire |
| NP | Nano particle |
| SEI | Solid electrolyte interphase |
| SS | Stainless steel |
| 3D | Three dimensional |
| EC | Ethylene carbonate |
| DEC | Diethyl carbonate |
| DMC | Dimethyl carbonate |
| FEC | Fluoroethylene Carbonate |
| VC | Vinylene carbonate |
| CMC | Carboxymethyl cellulose |
| GO | Graphene oxide |

## 1.0 Introduction

The ever soaring price of fossil fuels and increasing global environmental awareness have resulted in significant efforts to develop and adopt alternative energy technologies, *e.g.* widespread implementation of nuclear, solar and wind energy. A proactively increasing ratio of clean energy is both produced and consumed within recent decades. However, the energy storage and power supply technology has developed relatively slowly compared to the progress of alternative energies. It is a universal recognition that gas emissions from countless automobiles are accentuating localized air pollution as well as global warming. The high dependence on oils also leads to social problems and make the continued development of modern society unsustainable. These concerns stimulated the exploration of applicable electrically powered engines to replace the role of combustion engines. Modern electronic devices are most often powered by lithium ion batteries, replacing previous generations of nickel-cadmium, nickel-metal hydride, zinc-manganese batteries *etc*. When compared to the conventional batteries mentioned above, lithium ion batteries have many attractive advantages such as environmental benignity, high volumetric and gravimetric density, fast charging and discharging rates, and no memory effects.[1] Vehicles driven by batteries are gaining increasing market in the past decade. However, compared with internal combustion engines, current batteries are unable to match their energy density, power density or reliability. In addition, electronic devices employing more powerful applications and requirements drain batteries quickly. The urgent demand for high-energy and high-power density batteries from both the electronic and automobile industries drives research on the next-generation of batteries.

This thesis is structured to present readers an explicit idea of the modern battery progress along with ongoing development of energy conversion and storage devices and the fundamental

working mechanism of lithium ion batteries. The thesis then reviews the work reported by peers in this field, *i.e.* the development of novel anode materials, especially the design and application of silicon based and cobalt based materials. The work based on silicon materials focuses on the structural design and electrochemical performance of silicon graphene (Si-G) composites. More specifically, Si-G composites with different ratios were studied, including the synthesis, structural and morphological characterizations, and electrochemical characterizations. The cobalt project revealed a direct growth of active material on the substrate and its use in a battery's anode. Necessary characterizations were accomplished in addition to the sample preparation. In conclusion, the thesis consists of following parts:

i. The development of anode materials in lithium ion batteries. (This section is mainly based on literature review of other people's work)

ii. Research on the advance of silicon based materials and cobalt based materials.

iii. An introduction of all principal characterization techniques.

iv. A detailed description of the Si-G project.

v. A detailed description of the cobalt oxide project.

vi. A summary and an outline for the future direction of the project.

## 1.1 Lithium ion batteries

Researchers were first motivated to explore lithium based batteries because lithium has the highest electropositive potential (-3.04 V versus standard hydrogen electrode (SHE)) and it is the lightest metal in the universe (molecular weight of lithium is 6.94 g mol $^{-1}$ at a density of 0.53 g

$cm^{-3}$). These characteristics promote lithium as it can facilitate the design of batteries with a high energy density.[2] As shown in Figure 1, compared to traditional batteries like lead-acid and nickel-cadmium as well as relatively new batteries such as nickel-hydrogen, lithium based batteries including lithium-metal, lithium-ion, and polymeric lithium-ion batteries demonstrate much higher energy density in terms of both volume and mass. The first prototypes of lithium batteries were created in 1970s. These lithium cells were often referred to as lithium primary batteries, meaning they are non-rechargeable.[3] Due to the intrinsic properties of lithium batteries such as their high capacity and adjustable discharge rate, they were rapidly used to power devices in many fields, *e.g.* watches, implantable medical devices. At the same time researchers found that lithium can react with many compounds in a reversible way, eliciting speculation on the possibility of building rechargeable lithium batteries with these compounds. Intercalation reactions of lithium were first introduced in conference proceedings by Steele and Armand in *Fast Ion Transport in Solids* in 1973.[4]

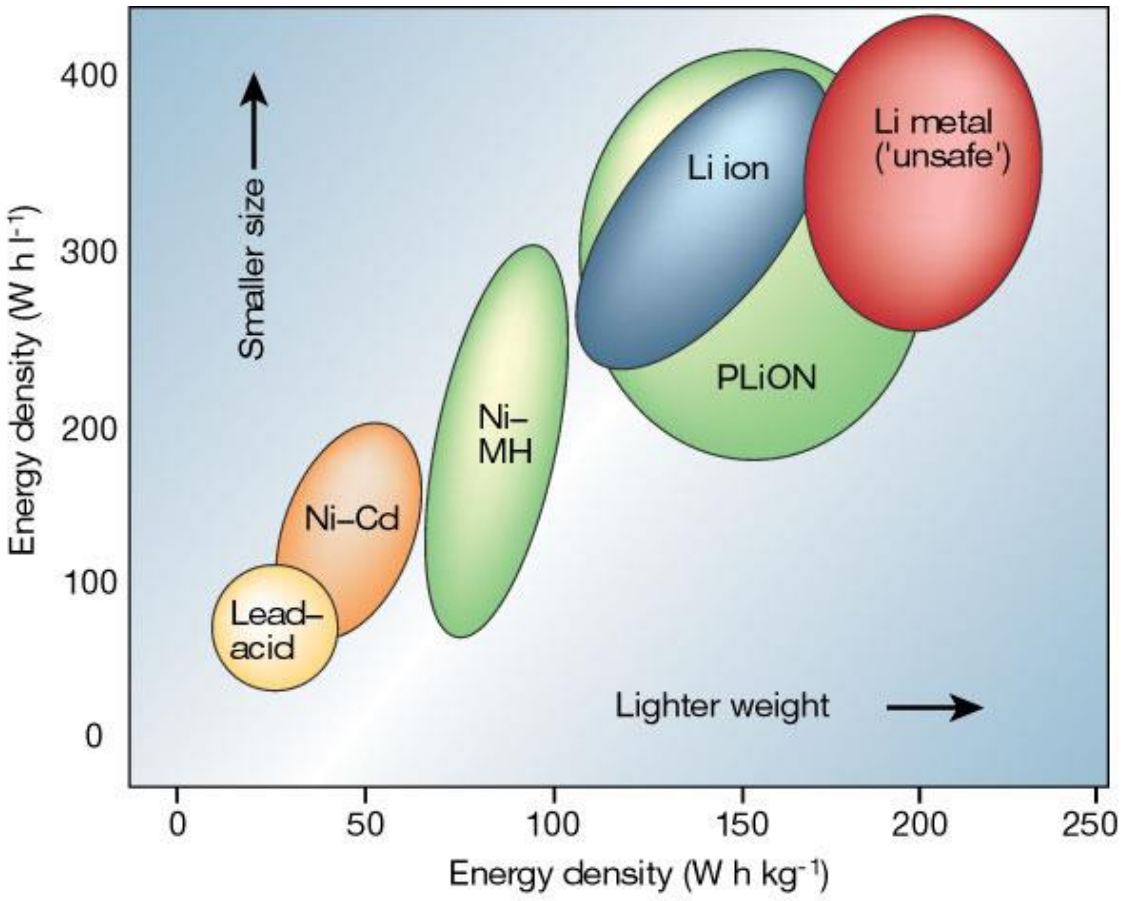


Figure 1: A diagram of volumetric and gravimetric energy density of different battery technologies mostly popular in market, namely, lead-acid, nickel-cadmium, nickel-metal hydride, and lithium based batteries.[2] Permission from Nature Publishing Group.

Whittingham, M. S at Exxon first used $TiS_2$ as a cathode in 1975, lithium metal as an anode and lithium perchlorate in dioxolane as the electrolyte. This prototype lithium metal battery exhibited revolutionary performance and the positive electrode material was incontestable at that era. However, lithium metal as the anode material encountered severe safety issues due to the continuous growth of dendritic lithium following charge and discharge cycles. As shown in Figure 2 (a), dendritic lithium is generated and cumulated on the anode upon cycling. Lithium in

this form is highly reactive, making this kind of battery extremely dangerous for disposal or during use if not properly sealed. The problem was first solved by substituting lithium metal with a lithium-aluminum (Li-Al) alloy.[5] The working mechanism diagram of lithium ion batteries is illustrated in Figure 2 (b). Although the problem of dendrite formation could be solved by using this alloy, the cycle stability of Li-Al caused another issue in lithium batteries due to their severe volume change upon cycling.[6] After the successful development of graphite as an anode material for LIBs, research continues to find that carbon based negative electrodes can be further optimized to improve their performance.[7] Meanwhile, efforts have also been made into the alternatives for carbon materials in a search for materials with enhanced characteristics in terms of capacity, rate capability and safety. Lithium transitional metal compounds were found to have the potential to meet these requirements.[8,9] In addition to carbon materials, Group IV elements such as silicon, germanium and tin also show high promise for application in LIBs.[10-13]

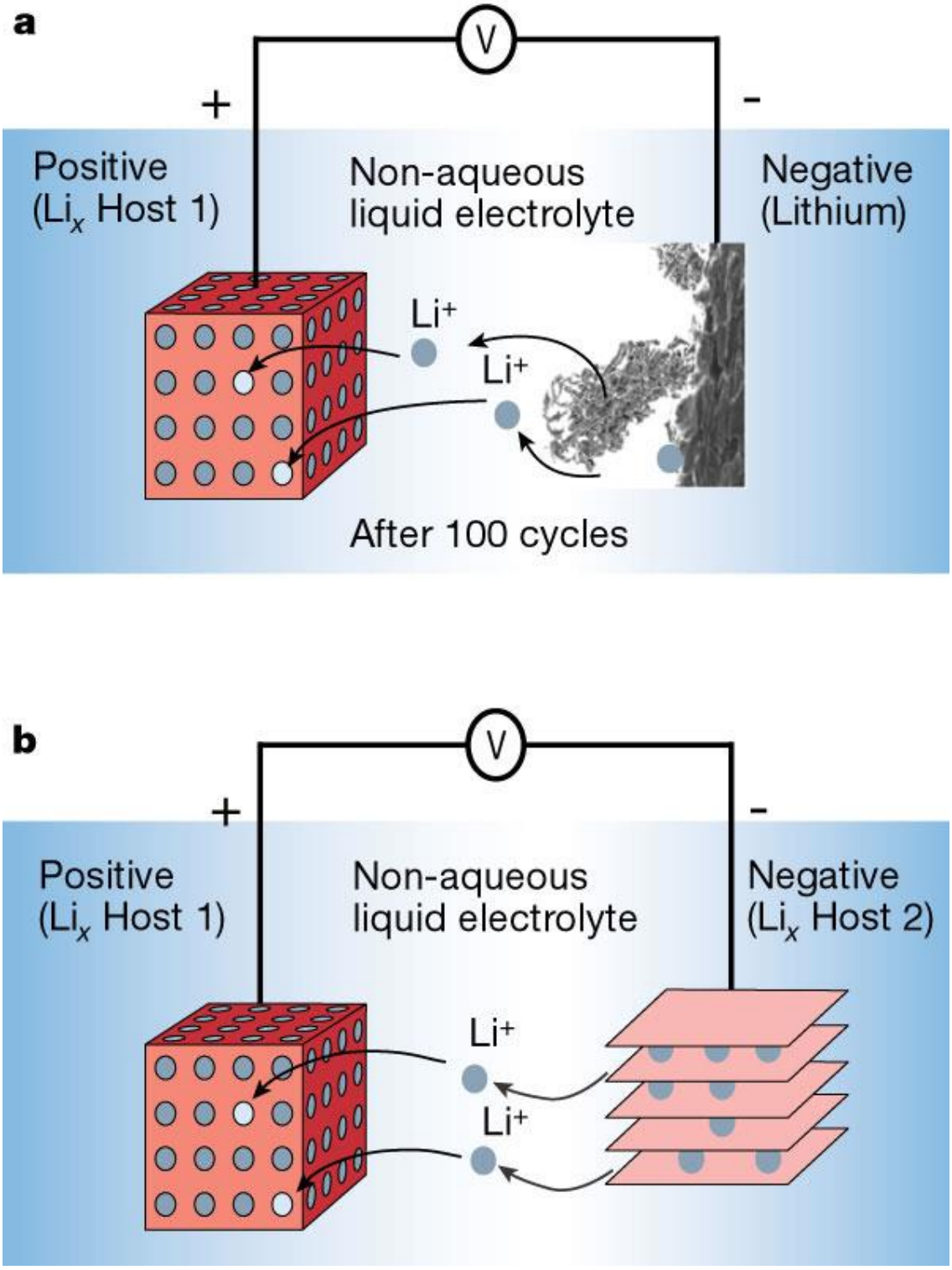


Figure 2: Schematic view of components and operating principals of lithium metal batteries (a) and lithium ion batteries (b).[2] Permission from Nature Publishing Group.

In addition to developments occurring using materials previously mentioned, certain oxides demonstrating high capacity and operating voltage were developed. More importantly, materials with multi-dimensions such as $V_6O_{13}$ were proved to function well as lithium ion battery electrodes.[14] Further on, Dr. John Goodenough in Oxford University developed various lithium metal oxides ($LixMO_2$, where M could be Manganese (Mn), Cobalt (Co) or Nickel (Ni)). These materials still dominate the cathode materials in lithium ion batteries today.[15,16] In the late 1980s and early 1990s, Murphy *et al.* and Scrosati *et al.* demonstrated the concept of replacing metallic lithium with layered insertion material. This was the prototype of modern lithium ion batteries in which elemental lithium can be ionically transported and transformed.[17,18] However, the adoption of insertion materials in the anode inevitably decreased the overall battery potential. In order to make up for the potential loss, lithium metal oxides were further investigated to replace the previously used metal disulphides such as $TiS_2$.[9] In 1983, in addition to $LiCoO_2$, spinel manganese was also discovered to possess the capability of storing and releasing lithium.[16] Its low-cost and good electron and lithium ion conductivity also boosted its promise in real applications, eventually migrating to commercialized cells. The pure manganese spinel faces fading problem upon exposure to cycling yet this problem can be effectively solved by morphology control and chemical decoration.[19,20] Another reason for the delay of wide spread application of these insertion materials was because of the failure of electrolyte. Although graphite was demonstrated as a replacement anode material for lithium metal by Samar in 1977,[21,22] the electrolyte at that time easily decomposed during the charge and discharge of batteries containing anodic graphite. Yazami first developed a rechargeable graphite anode with a solid state electrolyte to prove that lithium could be intercalated into graphite reversibly with

an electrochemical mechanism.[23] The graphite anode developed by Yazami is still exclusively used in commercial batteries owing to its low cost, high abundance and stable performance. Meanwhile, development of stable liquid and solid electrolytes has also played a very important role in promoting the widespread application of lithium ion batteries. Due to lithium ion battery's high operating potential it requires electrolytes to be thermodynamically and kinetically stable over potentials as high as 4.5 V.[24] The most satisfactory electrolyte also needs to meet several vital requirements,[25] for example:

1) High lithium ion conductivity, normally larger than $10^4$ S/cm for all temperatures at which the batteries operate.

2) Capability to retain the interphase of electrode and electrolyte.

3) Chemical stability at all operation temperatures of lithium ion batteries.

4) Cheap and environmentally friendly

5) Nonflammable and non-explosive in case of leaking or breaking.

Based on the cumulative progress of lithium ion battery technology, Sony finally commercially introduced lithium ion batteries into the worldwide market. In their devices they used carbon as an anode material and $LiCoO_2$ as the cathode. The charging voltage was 4.2 V while the operational voltage was 3.7 V, 3 times that of alkaline metal batteries at 1.2 V.[26] As shown in Figure 3, various types of cathode and anode materials are depicted in the diagram with energy density as the X-axis and potential versus lithium as the Y-axis. The potential range of cathode materials is much smaller than that of anode materials and the capacity of cathode materials is generally lower than that of anode materials. This demonstrates one of the main limitations of the overall capacity of modern LIBs, driving meaningful investigation into cathode materials with high capacities. Although the capacity

of anode materials is demonstrably higher, it is still desirable to pursue novel anode materials with high charge and discharge rates and better durability. Despite the capacity setback of cathode materials, the relatively larger potential range of cathode materials introduces a possibility of building batteries with an ultra-high open circuit and working potentials. Since the first success of commercialized LIBs, billions of these batteries have been built to fulfill a foundational role in the evolution of modern electronic and communication industries. However, development on the technology of lithium ion batteries moves much slower than the demand for high-power and high-energy batteries throughout the last two decades. Although many other electrode materials have been found to be electroactive for lithium ion batteries, *e.g.* different carbon materials,[27-31] tin-based materials,[11,12,32] lithium alloys,[33-41] transitional metal oxides,[42-47] lithium metal oxides with low electrochemical potential[48-53] as anode materials and cathode materials including manganese compounds,[54-57] nickel compounds,[58-60] vanadium compounds,[61-64] iron compounds,[65-69] mixed metal oxides[20,70-73] and so on, significant amounts of current lithium ion batteries still use $LiCoO_2$ and graphite as their electrode materials. Applicable electrode materials with high capacity and fast charge and discharge rate have not been widely used commercially due to several fatal drawbacks such as high cost, inadequacy for mass production, poor stability and the possibility of catastrophic internal discharge.

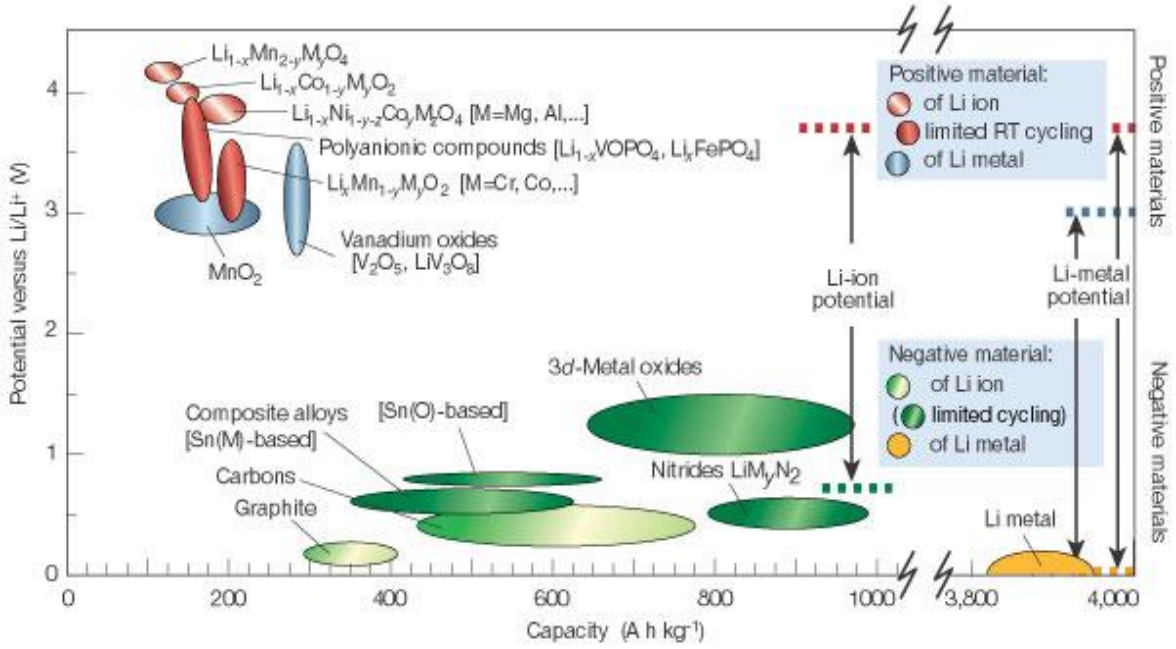


Figure 3: Comparison on electric potential and capacity of typical anode and cathode materials.[2] With permission from Nature Publishing Group.

### 1.1.1 Operational principles of lithium ion batteries

A typical lithium ion battery consists of a cathode, an anode, a separator, electrolyte, and a container. A lithium ion battery based on $LiCoO_2$ and carbon is a typical example of batteries used today.[74] The working mechanism of a lithium ion battery is illustrated in Figure 4. The cathode and anode consist of $LiCoO_2$ and carbon respectively, separated by a porous polymer membrane, commonly made from polypropylene. The electrolyte is not shown in the diagram, but it is worthwhile to know that lithium hexa-fluoro-phosphate ($LiPF_6$) dissolved in alkyl carbonate solvents is used commonly as the electrolyte. Some specific additives may be added to the electrolyte to enhance the electrode material. For example, fluoroethylene carbonate (FEC) is found to exhibit dramatic improvement on the performance of silicon anodes.[75] The container of

a LIB is built to be airproof and waterproof in most cases since both electrode materials and electrolytes are sensitive to air and water. Exposure of battery components to these air or water may lead to explosions or fires. The working mechanism of this type of batteries can be illustrated as follows: When the battery is discharged, the electromotive force from the outer circuit drives the electrons to move from anode to cathode (anode and cathode here represent electrodes inside the battery), and lithium ions are driven from anode to cathode as well. The anode is delithiated afterwards and the cathode becomes $LiCoO_2$ again. The operating voltage decreases, and the chemical energy is transformed to electric energy. When the battery is charged, electrons move from cathode to anode through an external circuit, and lithium ions shift from cathode to anode within the battery. Lithium ions are intercalated into carbon layers and $Li_xCoO_2$ (where x is usually between 0.5 and 1) is formed upon losing lithium ions. Electric energy is released in the form of chemical energy with an increase of open circuit voltage.[76] Surface films on both cathode and anode materials are observed in Figure 4. This phenomenon is due to the complex process that takes place on the surface of both cathode and anode materials, including decomposition of solvents in the electrolyte and dendritic growth of electrode materials, *etc*.[77] The films can protect the electrode from further direct exposure to the electrolyte and prevent side reactions from happening; however, the films can also increase the resistance of lithium ion transportation.[78,79]

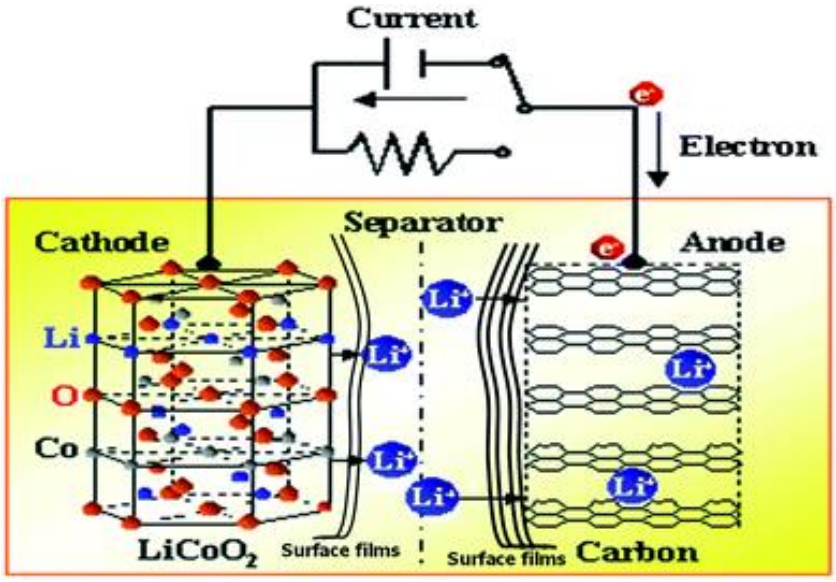


Figure 4: A schematic representation of a lithium ion battery with LiCoO2 as a cathode and carbon as an anode, in its simplest form.[74] Permission from Royal Society of Chemistry is required.

The electrode reaction in the cathode is as follows:

$$LiCoO_2 \leftrightarrow 0.5\ Li^+ + 0.5\ e^- + Li_{0.5}CoO_2 \qquad (1)$$

The maximum electrochemical potential of $LiCoO_2$ against lithium metal is 4.2 V upon delithiation of $LiCoO_2$, in correspondence to the formation of $Li_{0.5}CoO_2$. This process can contribute a capacity of 140 mAh $g^{-1}$ for the cathode.[80,81] The reaction above is the first step of the reactions in a battery, with the oxidation and delithiation of $LiCoO_2$ to $Li_{0.5}CoO_2$. Simultaneously, graphite at the anode obtains lithium ions and electrons and forms $LiC_6$ as a product of the reaction as shown below:

$$Li^+ + e^- + C_6 \leftrightarrow LiC_6 \qquad (2)$$

The overall electrode reaction is:

$$C_6+LiCoO_2 \leftrightarrow LiC_6 + Li_{0.5}CoO_2 \quad (3)$$

The double arrows in these equations represent that those reactions are reversible. The intercalation of lithium into graphite occurs in multiple stages, with formation of $LiC_{27}$, $LiC_{24}$, $LiC_{12}$ and $LiC_6$ respectively.[82] A passivating layer, consisting of electrolyte solution and the lithium source, may irreversibly form to prevent further loss of electrolyte during the first cycle of lithium insertion. The passivating layer is also referred to as the solid electrolyte interphase (SEI).[79,83] Since the formation of SEI consumes lithium, and the lithium source in a lithium ion battery mainly comes from the cathode, it is critical to keep cathode material in excess. Research in maintaining the minimum amount of cathode material is also a meaningful task.

During the early stages of development of lithium ion batteries, finding suitable electrolyte for batteries was a key issue. As shown in Figure 5, several categories of electrolyte systems have been found suitable for LIBs, including ethers based, esters based, alkyl carbonates based, and nitriles based electrolytes. Alkyl carbonate solutions such as ethylene carbonate (EC), dimethyl carbonate (DMC), diethyl carbonate (DEC) and the lithium salt lithium hexafluorophosphate ($LiPF_6$) were found to function impeccably and most widely used in lithium ion batteries.[84,85] The electrochemical stability of different solvents was investigated by D. Aurbach *et al*.[74,86,87]

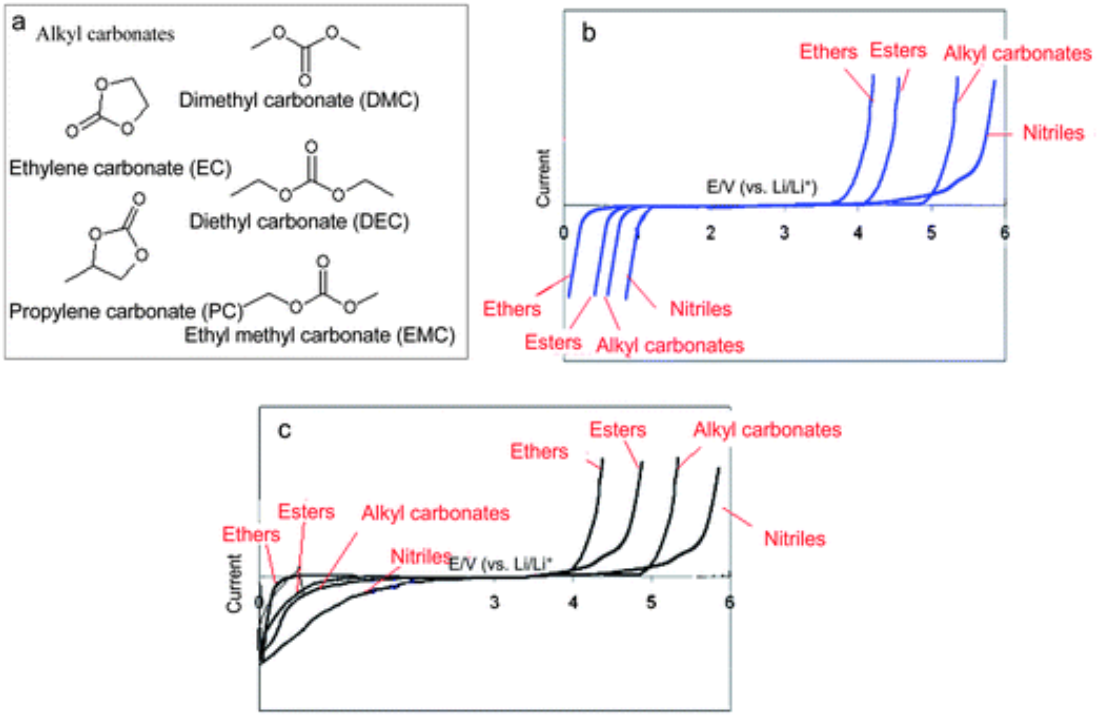


Figure 5: (a) Several typical alkyl carbonates for lithium ion battery electrolyte. (b) Electrochemical windows of various solvents tested with tetra-alkyl ammonium salts. (c) Electrochemical windows of lithium salt solutions if different solvents.

### 1.1.2 Technical challenges, prospects and motivations.

The most popular lithium ion batteries are comprised of graphite anodes and cathodes made from various materials including $LiCoO_2$, $LiFePO_4$ and other less widely used materials. Apart from graphite anodes, other anode materials such as soft carbon and hard carbon have also been adopted in commercial batteries to obtain improved stability and higher capacity. Key criteria include energy density, power density, safety, battery's working potential, cost, and durability. As shown in Figure 6, many attractive solutions to optimize the cost and safety of lithium ion

batteries have been proposed. The most commonly used separators are made from polypropylene and polyethylene. The electrolytes that are currently widely used are alkyl carbonates based solutions with some aprotic lithium salts. To achieve different technical standards and fulfill various applications, batteries are designed with different combinations of cathode and anode materials. For example, $LiMn_2O_4$ and some other cathode materials are used to combine with $Li_4Ti_5O_{12}$ anode to fabricate batteries out of concern for safety. The charging and discharging plateau of $Li_4Ti_5O_{12}$ is at more than 1 V versus lithium metal and there is no destructive SEI formation during charge and discharge.[88] Safer batteries are achieved at the compromise of capacity, *i.e.* a capacity of only around 85 Wh $kg^{-1}$ is achieved in $LiMn_2O_4$/ $Li_4Ti_5O_{12}$ cells compared to that of 140 Wh $kg^{-1}$ in $LiMn_2O_4$/C cells.[89]

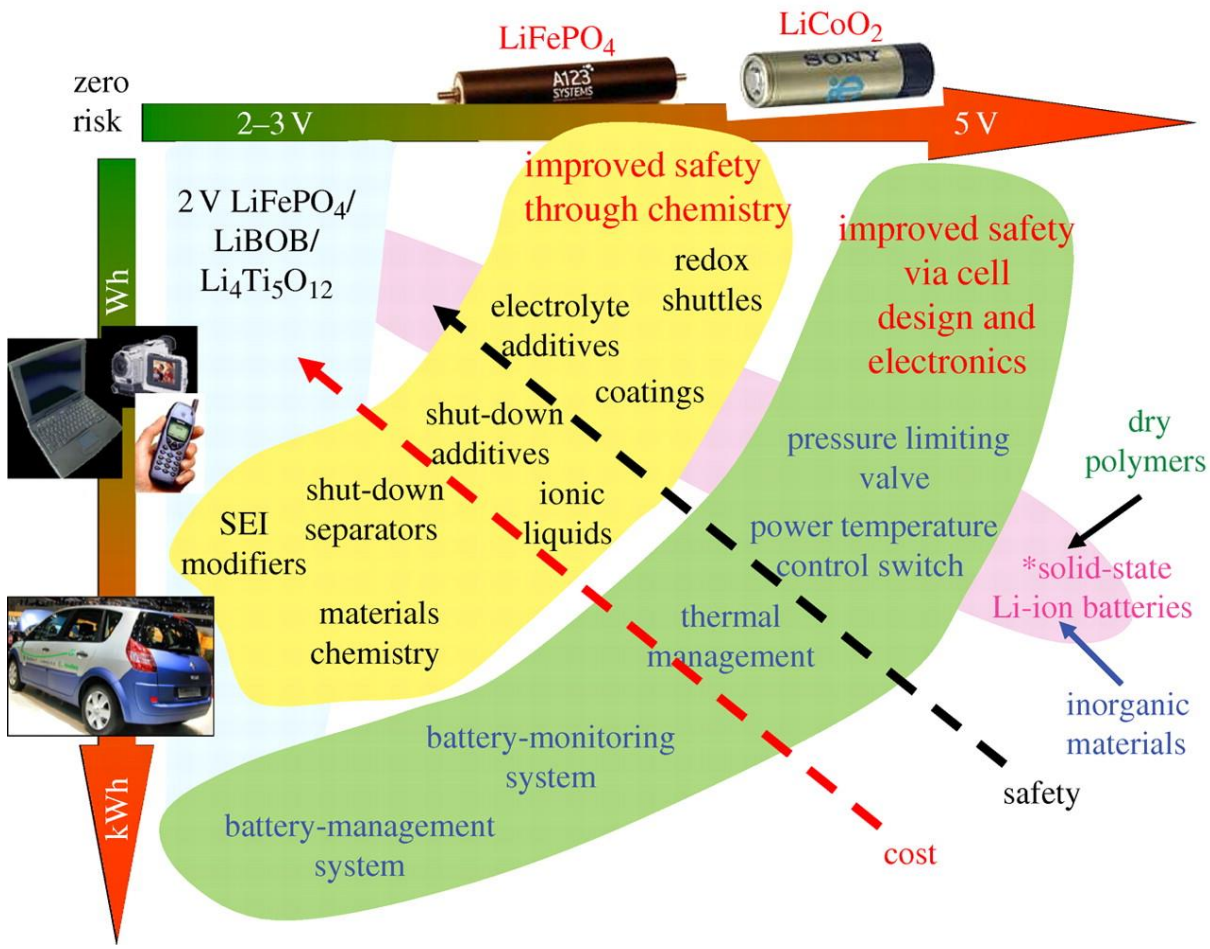


Figure 6: A schematic view of safety concerns on lithium ion batteries and efforts made aiming to build safe batteries.[89] Permission from The Royal Society Publishing if required.

Significant efforts are also seen to be put into the research for novel separators as separators with high wettability for electrolyte solutions are highly desirable.[90] To overcome the intrinsic shortcomings of liquid electrolytes, such as dendrite growth from electrolyte solution upon cycling, poor accommodation for volume change of electrodes, considerable reactivity with electrodes, safety issues and difficult shape control,[91-93] solid state electrolytes are under consideration as a replacement.[94-96] Although solid electrolytes solve many of the issues listed above, there are still certain challenges to overcome:

1) The ionic conductivity. Namely, the conductivity of lithium ions of current solid or polymer electrolytes needs improvement. Commonly used liquid electrolytes have an ionic conductivity of around $10^{-3}$ to $10^{-2}$ S $cm^{-1}$. The solid electrolyte should also have the ionic conductivity close to that value.[97]

2) Transference number. It is also a crucial measure to increase the transference number of the electrolyte. Normally the transference number of both liquid and solid electrolytes is smaller than 0.5.[98,99] It is desirable to have a relatively large transference number to reduce the concentration polarization of electrolytes and provide higher power density.

3) Thermal, chemical, and electrochemical stabilities. The applicable electrolytes should have enough stable potential range to accommodate different kinds of batteries.

4) Mechanical strength. Although the solid electrolytes can be fabricated to be free-standing now. Its mechanical strength still needs to be improved in order to be manufactured with a large scale coating process.

Apart from the challenges from electrolytes, the most critical factor limiting the development of LIBs comes from the electrode materials, namely, cathode and anode materials. In the first generation LIBs, electrodes were composed of millimeter-sized particles. Although the energy density of those batteries was high, the power density of these batteries was less competitive. The limit of the power density came from the intrinsic limitation of lithium ion diffusion rate in the solid state materials. The charge and discharge rate is hence hindered by the slow lithium intercalation or extraction of the electrode material. Modern applications of lithium ion batteries, such as electric and hybrid vehicles demands both high energy and high power density batteries, thus a new concept should be proposed to break the rate limit of LIBs.

Nanomaterials, owing to their reduced dimensions, have been proposed as a cure for the rate problem of conventional batteries. It is a fact that nanomaterials can enable much faster lithium intercalation and extraction rate (graphite or $Li_4Ti_5O_{12}$). The conversion rate of $Li_2O$/metal can also be improved for the electrode materials that undergo conversion reactions (transitional metal oxides), and thus improve the overall performance. In spite of the advantages of nanomaterials for LIBs, it is also worthwhile to learn their disadvantages. With a thorough understanding of both their strengths and weaknesses, we can find suitable strategies to tackle the issues and build LIBs with enhanced performance.

In general, advantages and disadvantages of nanomaterials for lithium ion batteries can be concluded as follows:

Advantages:

1) Nanomaterials can allow reactions to take place that cannot happen for bulky state materials; for instance, β-$MnO_2$ can endure the lithium intercalation and extraction processes and maintain the original rutile structure, which is impossible for bulky $MnO_2$.[100]

This also applies other materials like α-$Fe_2O_3$. As shown in Figure 7 and 8, nanostructured $Fe_2O_3$ demonstrated much better cycling performance than $Fe_2O_3$ at bulky state. In addition, the capacity of nanostructured $Fe_2O_3$ is much higher than that of bulky $Fe_2O_3$. The stability variance is due to the fact that lithium can be intercalated reversibly into the oxide through a single-phase process, while the packing order of $Fe_2O_3$ in the bulky state changes in order to accommodate the volume change due to lithium insertion and extraction. Severe volume change may also lead to the pulverization of the electrode and trigger continuous side reactions at the surface and cause electrode failure. Nanostructured $Fe_2O_3$ can hold up to 1 Li per $Fe_2O_3$, while less than 0.1 Li per

$Fe_2O_3$ can be inserted into bulky $Fe_2O_3$.[101] This finding introduces the possibility that many materials considered unsuitable for lithium storage might fulfill the criteria.

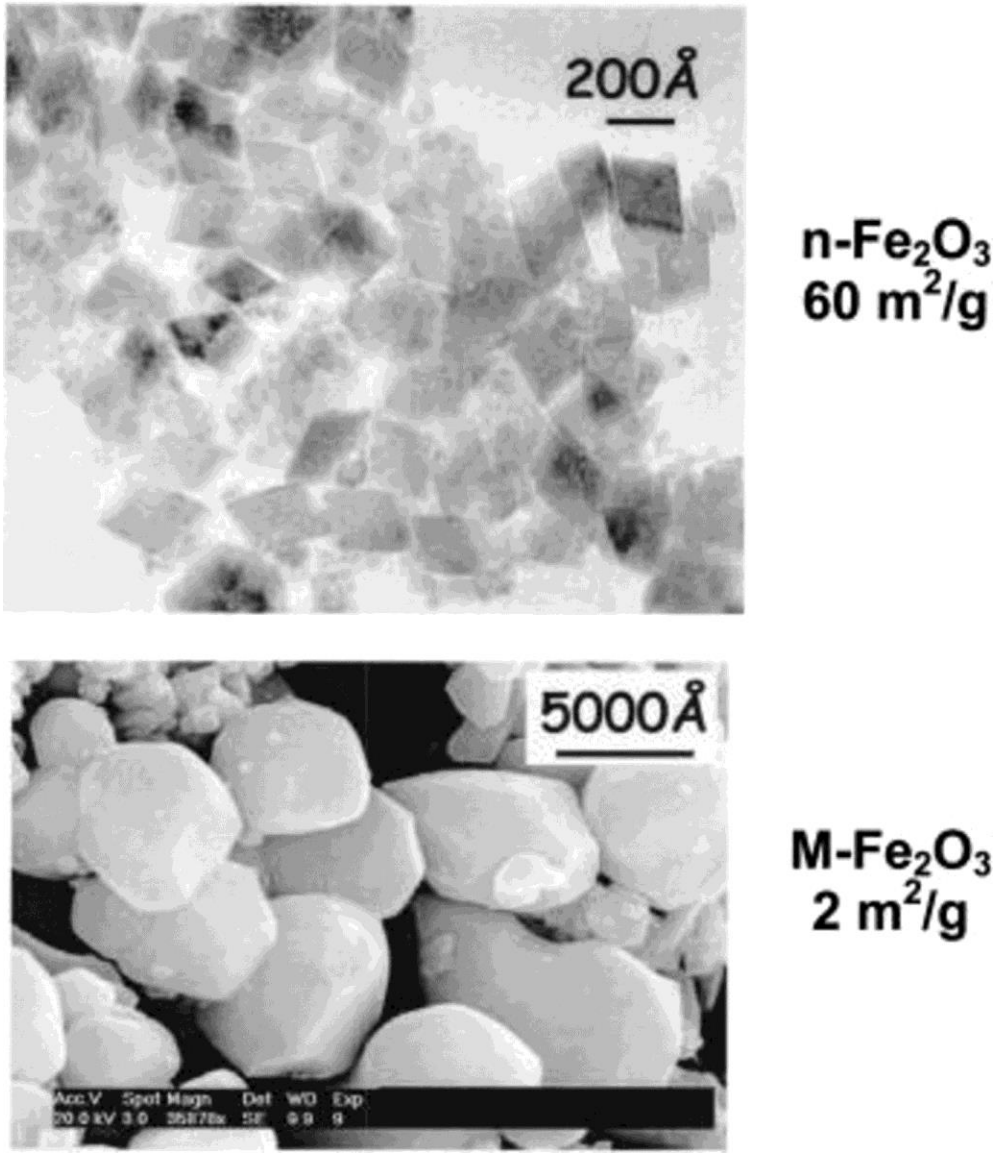


Figure 7: SEM images of nano-sized $Fe_2O_3$ (up) and bulky $Fe_2O_3$ (down).[101] Permission from The Electrochemical Society if required.

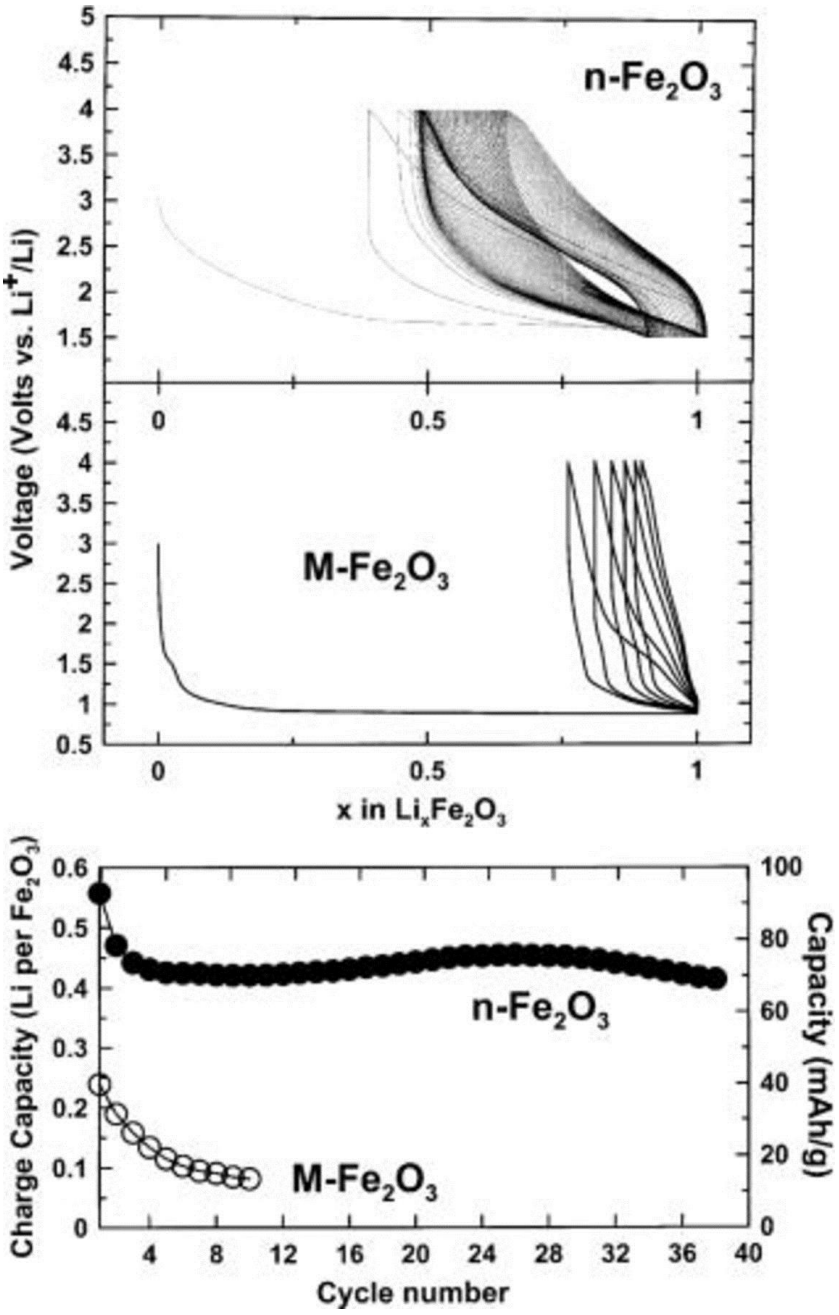


Figure 8: A comparison of electrochemical performance of bulky and nano-sized α-$Fe_2O_3$. The cycling data and the SEM images are shown in insets.[101] Permission from The Electrochemical Society if required.

2) The significantly reduced sizes of the electrode materials can greatly improve the rate of the conversion and intercalation reactions of lithium. This is due to the shortened distances for

lithium ion diffusion between grains and between the electrolyte and the material. The diffusion rate of lithium ions can be characterized as $t=L^2/D$, in which L is the diffusion distance and D is a diffusion constant. With the increase of the diffusion distance, t increases with the square of L, and this means the diffusion rate decreases much faster with the increase of the size of the electrode materials.[1]

3) Nano-materials also exhibit extremely high specific surface area, and hence lead to better contact between the electrolyte and the material.

4) Electron transport also benefits from the reduced dimension of the material, the mechanism of which is similar to that of ion transport.

5) The chemical potentials of some materials for lithium conversion or intercalation may be modified to be thermodynamically favorable for these reactions.[102]

6) Large contact area between these nanocomposites and short lithium ion diffusion paths are kinetically favorable for the reversible conversion of transitional metals and $Li_2O$.[103,104]

7) Nanoparticles can usually form solid solutions with a much larger range of compositions,[105] and the ability to accommodate for volume change is much better than bulky materials.

As shown in Figure 9 (a), silicon experiences significant volume increase upon the formation of $Li_{22}Si_5$. As a result, bulky silicon plates and particles fail to endure the volume change and will pulverize, causing the loss of contact points between the active material and current collector. Furthermore, the unstable surface of these bulky materials can lead to the continuous growth and crackdown of SEI. As illustrated in Figure 9 (b), nanostructured silicon wires not only provide efficient electron transport pathway, but also well relax the strain from the volume expansion, and thus present themselves as a promising candidate for lithium ion battery anode.[106]

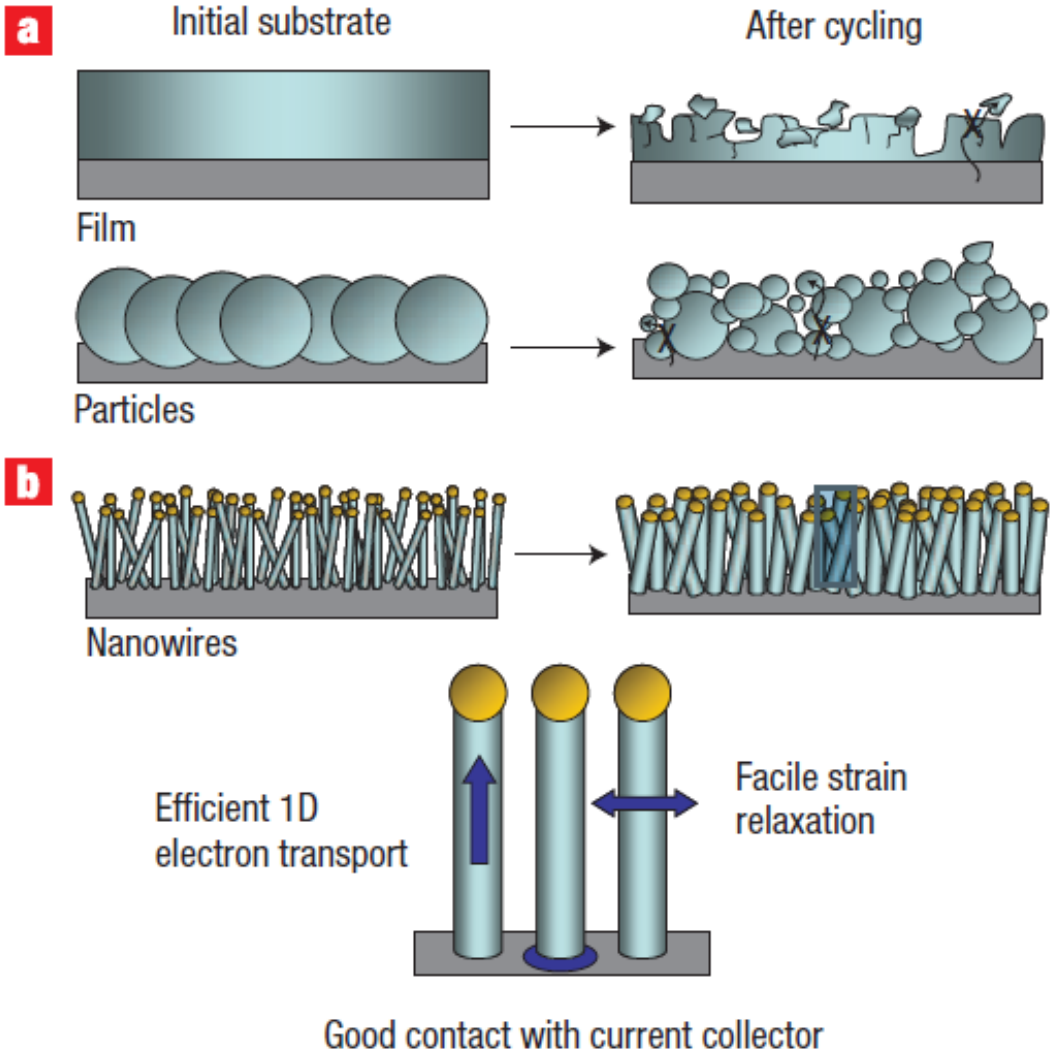


Figure 9: A schematic presentation of how silicon nanowire accommodates the strain, (a) bulky film and particles as electrodes before and after cycling, (b) nanowires before and after cycling.[106] Permission from Nature Publishing Group if required.

Disadvantages:

1) The synthesis of nanomaterials might be more difficult, and may cost more than normal materials. It is also more difficult to control the morphology and the dimensions of nanomaterials.

2) High surface area of nanomaterials can contribute to the better contact of electrolyte and electrode materials; however, the large surface area can lead to irreversible side reactions and difficulty in maintaining the inter-particle contact.

3) The tap density of nanomaterials is usually lower than that of bulky materials. This may inevitably decrease the volumetric energy density.

To conclude, LIBs have been contributing tremendously to the evolution of the modern communication industry in recent years. Applications of LIBs include mobile phones, laptops, digital cameras, and many other portable electronic devices.[26] As fossil fuels are being consumed at an astonishing speed and their price continues to rise, LIBs as the power source for vehicles are garnering more and more attention. Commercialization of electric vehicles is proceeding slowly due to several fatal drawbacks of current commercial batteries, e.g. lower energy density compared to fossil fuels and their frequently-reported safety issues.[107] In order to meet the ever-increasing demand of high energy and power density LIBs, alternative anode materials have been widely investigated, including lithium metal alloys,[108,109] transitional metal compounds,[110-114] and silicon-based materials.[115-121] These materials have all been reported to present significantly higher capacities than commercial graphite. Among all these materials, silicon has the highest as-known specific capacity of 4200 mAh $g^{-1}$ at the full lithiation stage (corresponding to the formation of Si-Li alloy $Li_{22}Si_5$), showing a huge potential for the increase of LIB's capacity. These materials suffer from severe volume expansion and contraction during charge and discharge process. The insertion and extraction of such a large amount of lithium leads to severe volume change of silicon (300 percent of volume increase upon full lithiation), which further causes the pulverization of silicon in electrode material, loss of conductive points and the damage of solid electrolyte interphase (SEI). All these result in silicon's poor stability upon

cycling, which leads to poor long-term cycling stability.[122] To achieve a long cycle life of a LIB, it is critical to accommodate the volume change of silicon and help to form a stable SEI layer. Significant efforts have been made to deal with the above issues with silicon. Two most frequently reported methodologies to address current issues with silicon are engineering special morphologies of silicon and combining conductive materials with semi-conductive silicon.

## 1.2 Silicon based anode materials

| Materials | Li | C | $Li_4Ti_5O_{12}$ | Si | Sn | Sb | Al | Mg |
|---|---|---|---|---|---|---|---|---|
| Density (g/cm3) | 0.53 | 2.25 | 3.5 | 2.3 | 7.3 | 6.7 | 2.7 | 1.3 |
| Lithiated phase | Li | $LiC_6$ | $Li_7Ti_5O_{12}$ | $Li_{4.4}Si$ | $Li_{4.4}Sn$ | $Li_3Sb$ | LiAl | $Li_3Mg$ |
| Theoretical specific capacity (mAh/g) | 3862 | 372 | 175 | 4200 | 994 | 660 | 993 | 3350 |
| Volume change (%) | 100 | 12 | 1 | 420 | 260 | 200 | 96 | 100 |
| Potential versus Li (V) | 0 | 0.05 | 1.6 | 0.4 | 0.6 | 0.9 | 0.3 | 0.1 |

Table 1: A comparison of some common anode materials for lithium ion batteries. The parameters of the materials include their densities, lithiated phases, theoretical capacities, volume changes, potentials versus lithium.[123]

Properties of several commonly studied anode materials are shown in Table 1. It can be seen that silicon possesses the highest theoretical specific capacity (4200 mAh $g^{-1}$) among all these materials listed in the table, corresponding to the formation of $Li_{4.4}Si$. Silicon is the second most abundant element in the earth crust, and the technique of processing silicon has also been well developed. Despite the advantages of silicon anode materials, it is also important to note the disadvantages of using silicon anodes. For instance, the significant volume change of silicon during charge and discharge leads to poor capacity retention of silicon anodes.[124,125] It has been experimentally proven that silicon undergoes phase change during the lithiation and delithiation process, *i.e.* crystalline to amorphous phase transition.[126] In addition, the electric conductivity of

silicon is poor since it is a semiconductor, making it challenging to apply silicon to high-power batteries. In general, three fundamental challenges of silicon anodes can be concluded as follows:

1) Pulverization of silicon materials. The large volume change of silicon may often cause cracking down of the material, especially in bulky silicon materials (Figure 10 a).

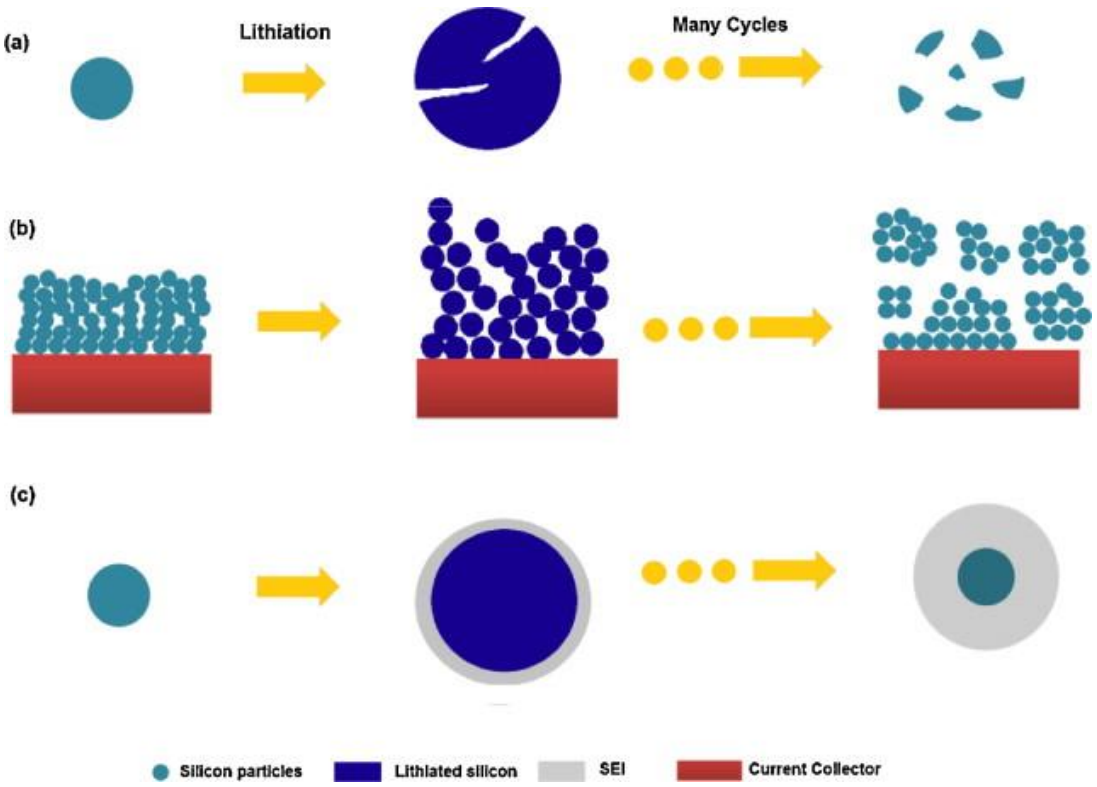


Figure 10: graphical illustrations of fundamental failing mechanisms of silicon electrodes: (a) Material pulverization, (b) electrode degradation, (c) formation of an unstable SEI.[123] Permission from Elsevier if required.

2) Volume and morphology change of the whole electrode. The volume and morphology change of the electrode may lead to the loss of contact points between electrode materials and the substrate. The detachment of active material to the substrate inevitably increases the electrical resistance of the electrode and thus results in the battery failure (Figure 10 b).

3) Unstable solid electrolyte interphase. As shown in Figure 10 c, continuous breaking down and growth of SEI may lead to ceaseless side reactions at the surface of silicon and decomposition of electrolyte. The process is irreversible, and the thick SEI may block the lithium ion conductive pathways and retard lithium intercalation and extraction.[127]

To overcome the obstacles listed above, significant efforts have been made in the field of nanostructured silicon anodes. Silicon nanowires,[128] silicon nanoparticles,[129] hollow silicon nanostructures,[130] and silicon nanostructures decorated with conductive materials[131] have been reported exclusively to obtain stable and high capacity lithium ion battery anode. In spite of the effort made on electrode materials, specialized binders such as carboxymethyl cellulose[132] and sodium alginate[133], and electrolyte additives including FEC[75] have also been put under scrutiny.

In this thesis, silicon and graphene composites have been systematically studied to learn the effect of graphene on the performance of silicon nanoparticles, and highly promising results are obtained from this research.

### 1.3 Cobalt oxide as anode materials

P.Poizot *et al.* proved for the first time that transitional metal oxides can store lithium via a heterogeneous conversion reaction mechanism:[47]

$$M_xO_y + 2y\ Li \rightarrow y\ Li_2O + x\ M \qquad (4)$$

In this generalized reaction equation, M stands for any applicable metal, and x and y represent integers in the most simplified reaction formula. This reaction was not expected to happen due to the very inert reactivity of $Li_2O$ with transitional metal oxides at room temperature. It was later clarified that the strengthened electrochemical reactivity of $Li_2O$ is owing to the nanostructure of the metal oxides. In these nanostructures, $Li_2O$ and transitional metals can form ultra-tiny grains

that can interphase homogeneously.[134] Large contact area between these nanocomposites and the short lithium ion diffusion paths are kinetically favorable for the reversible conversion of transitional metals and $Li_2O$.[103,104]

Nano-sized $Co_3O_4$ has been known as a lithium electroactive anode material in LIBs for many years and many methods have been used to obtain different morphology of $Co_3O_4$ nanostructures.[135] $Co_3O_4$ nanoparticles,[136] nanotubes,[137] nanowires,[138] cages,[139] and $Co_3O_4$-carbon composites[140] have all been reported as effective materials for LIBs as $Co_3O_4$ exhibits relatively high theoretical capacity of 890 mAh $g^{-1}$; more than twice that of commercial graphite. Common powder-type materials require a conventional electrode fabrication process with a binder and carbon material which will decrease the specific energy density of batteries; besides, contact between active material and current collector may deteriorate upon cycling, causing the long term cycle stability and rate capability failure.[141]

## 1.4 Project's scopes and objectives

Lithium ion batteries are highly promising for next-generation powerful and durable electric vehicles. Current anode materials cannot fulfill the ever-increasingly rigorous requirements for lithium ion batteries. Silicon, as a potential anode material, has been well known for its high capacity, although the durability of the material is an issue due to its intrinsic drawbacks and has been a main hindrance to its implementation in the LIB industry. $Co_3O_4$ also provides much higher theoretical capacity than commercial graphite anodes, and it is easy to engineer various dimensions and morphologies with $Co_3O_4$. $Co_3O_4$ undergoes conversion reaction during lithium storage and release, and the formation and decomposition of $Li_2O$ is kinetically unfavorable, making the reaction slow. Furthermore, the phase change during the conversion reaction may lead to irreversible capacity and cause the failure of the electrode.

To overcome the shortcomings of these two materials, the work in this thesis includes the design of graphene wrapped silicon composites and direct growth of $Co_3O_4$ nanowires on a flexible stainless steel mesh. Both pronounced capacity and rate capability are achieved in these materials, and this provides a possible solution to the urgent demand for next generation lithium ion batteries.

In general, the objectives of this thesis are listed as follows:

- Develop novel anode materials with improved capacity and durability.
- Explore new advanced anode material with enhanced rate capability.
- Design facile materials synthesis and simple electrode fabrication methods.

## 2.0 Structural and Electrochemical Characterization Techniques

Material synthesis and characterization are both vital to our research. Necessary characterization techniques can provide a fundamental understanding of the mechanism of the synthesis process, and help decide the necessary changes to the design of the experiments. For example, the preliminary scanning electron microscope (SEM) images provide the detailed morphological information of the synthesized Si-G composites, from which the sizes of Si particles and graphene can be determined. In addition, it can help with the analysis of finding the proper ratio of Si and graphene needed to form a well-wrapped Si-G composite. Thermogravimetric analysis (TGA), X-ray diffraction (XRD), transmission electron microscope (TEM), Raman spectroscopy, *etc.* are all indispensable to obtain the necessary characteristics of the materials. Electrochemical characterization is a key part to the accomplishment of the project. The electrochemical performance is recorded with several basic measurements, *e.g.* cyclic voltammetry, long term charge and discharge, electrochemical impedance spectroscopy and rate capability test. Detailed description of some essential characterization techniques and materials synthesis methodology are explained in the following sections.

### 2.1 Scanning Electron Microscopy

Scanning electron microscopy (SEM) is a very useful tool to detect a sample's topology and composition. A fine SEM can be competent to obtain morphological images of a sample to a scale of several nanometers. As shown in Figure 11, silicon nanoparticles (50 nm-70 nm) are wrapped by graphene, and the distribution of silicon nanoparticles and the fringes of graphene sheet can be clearly observed from SEM images.

SEM is an electron microscope which produces electron beams to interact with a sample, and reflects the samples' properties by collecting the signal of electrons after interaction with the sample. Normal SEMs operate at a high vacuum atmosphere (~$10^{-5}$ mmbar), but according to different real applications, there are special SEMs which can work under low vacuum or even atmosphere, for example, environmental SEM.

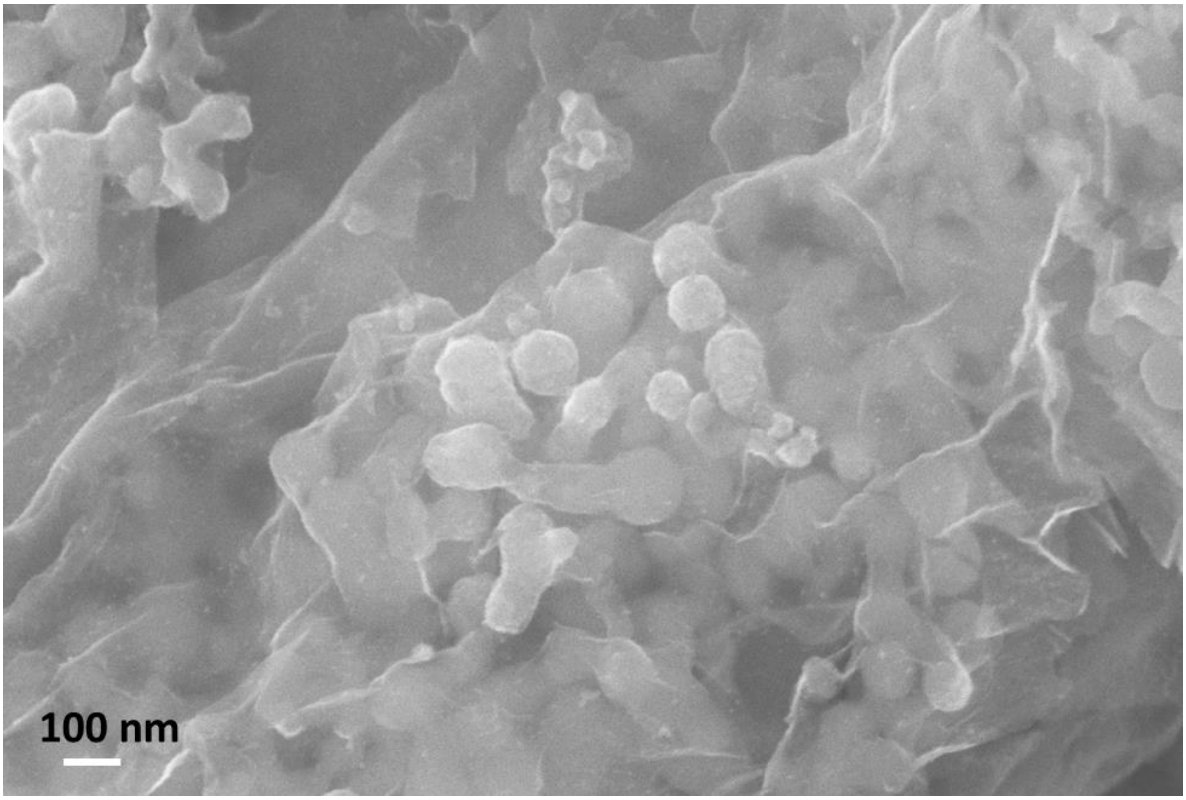


Figure 11 A SEM image of a silicon-graphene composite sample.

As shown in Figure 12, main components in a SEM system include an electron gun, an electron lens, a scanning system, a detector, a display, and a vacuum system. Electron beams are firstly generated by an electron generating device, such as a tungsten filament cathode, or a field emission electron gun. Electrons are subsequently accelerated by the electric field to 0.2 to 40 keV. Meanwhile, the beam is condensed to be with a diameter of less than ten nanometers. Then

the electron beam goes through the scanning coil, where the beam can be controlled by an operator to scan the specimen. The signals from the sample are detected, amplified and shown on the display simultaneously.

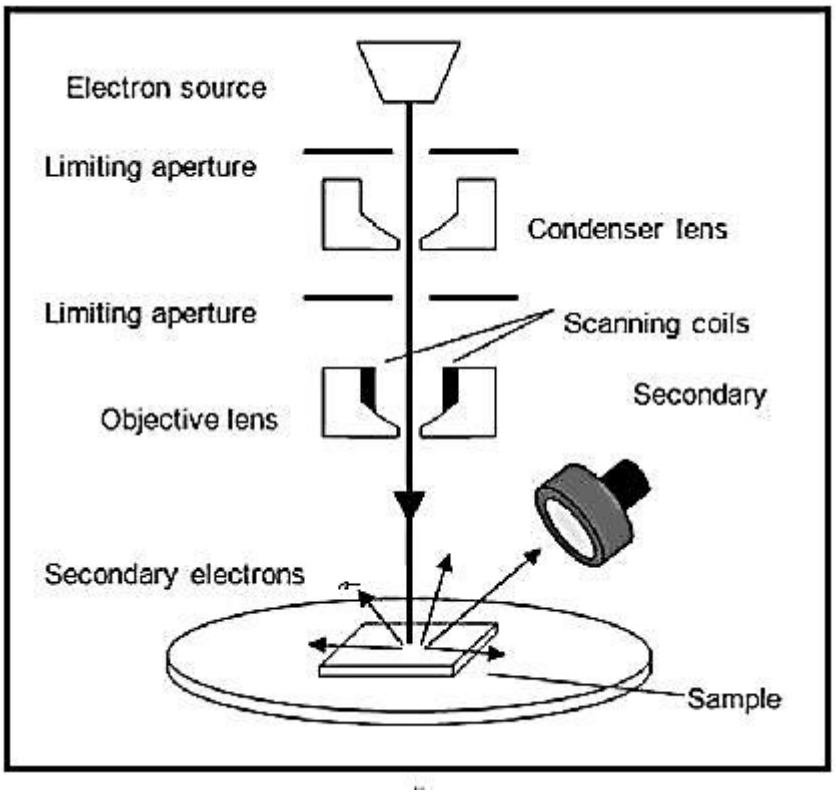


Figure 12. A schematic view of a SEM system.

**2.2 Transmission Electron Microscopy**

Transmission electron microscopy (TEM) is another versatile electron microscopy. Unlike SEM, a beam of highly focused electrons are directed toward a thinned sample (<200 nm) in a TEM, and high energy incident electrons interact with the sample. Information of the sample is obtained from both deflected and non-deflected transmitted electrons, backscattered and secondary electrons, and emitted photons. As illustrated in Figure 13, similar to a SEM, a TEM also has an electron gun, which can be either a thermionic or a field emission gun. Followed is a

condenser which can narrow the electron beam. Different from that of SEM, electrons in a TEM are typically accelerated to 100 to 400 keV to gain enough energy to transmit the specimen and hit the fluorescent screen. Electrons are accelerated shortly after they are generated from the emission source. After that, the electron beam is condensed through an aperture. Then electrons meet with the specimen and generate different kinds of electrons, which are used to obtain different information of the sample. Objective lens and diffraction lens after the sample chamber are used to help converge electrons from transmission and diffraction. Those electrons are further expanded by the projector lens to form images on the display devices. The magnification of the TEM is closely related to the ratio of the distances between the specimen and the objective lens' image plane, as well as the diameter of the display’s size.

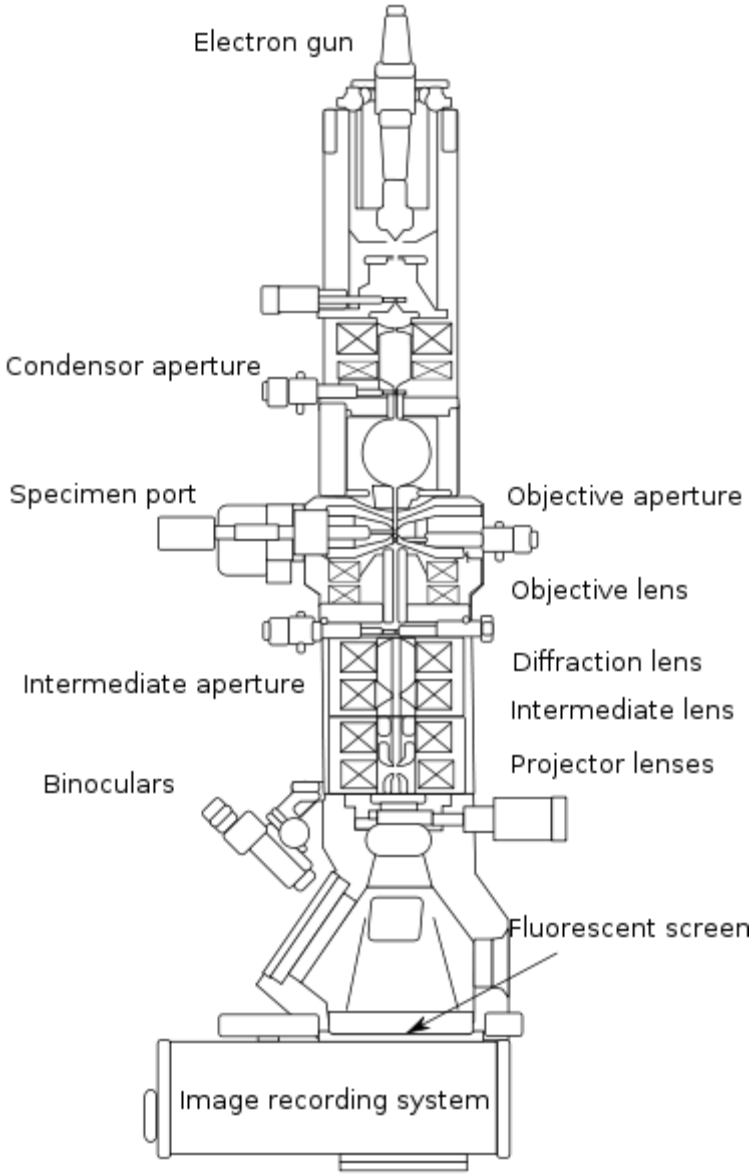


Figure 13. A schematic view of a TEM system.

The resolution of a TEM can be as high as 0.2 nm, which is much higher than that of a SEM. As a result crystal structure of a sample can be obtained with those high resolution TEMs, which are usually referred to as HRTEM. In Figure 14, a high-resolution TEM image of intrinsic silicon shows the regular arrangement of silicon atoms, from which the crystal structure of the sample can be determined.

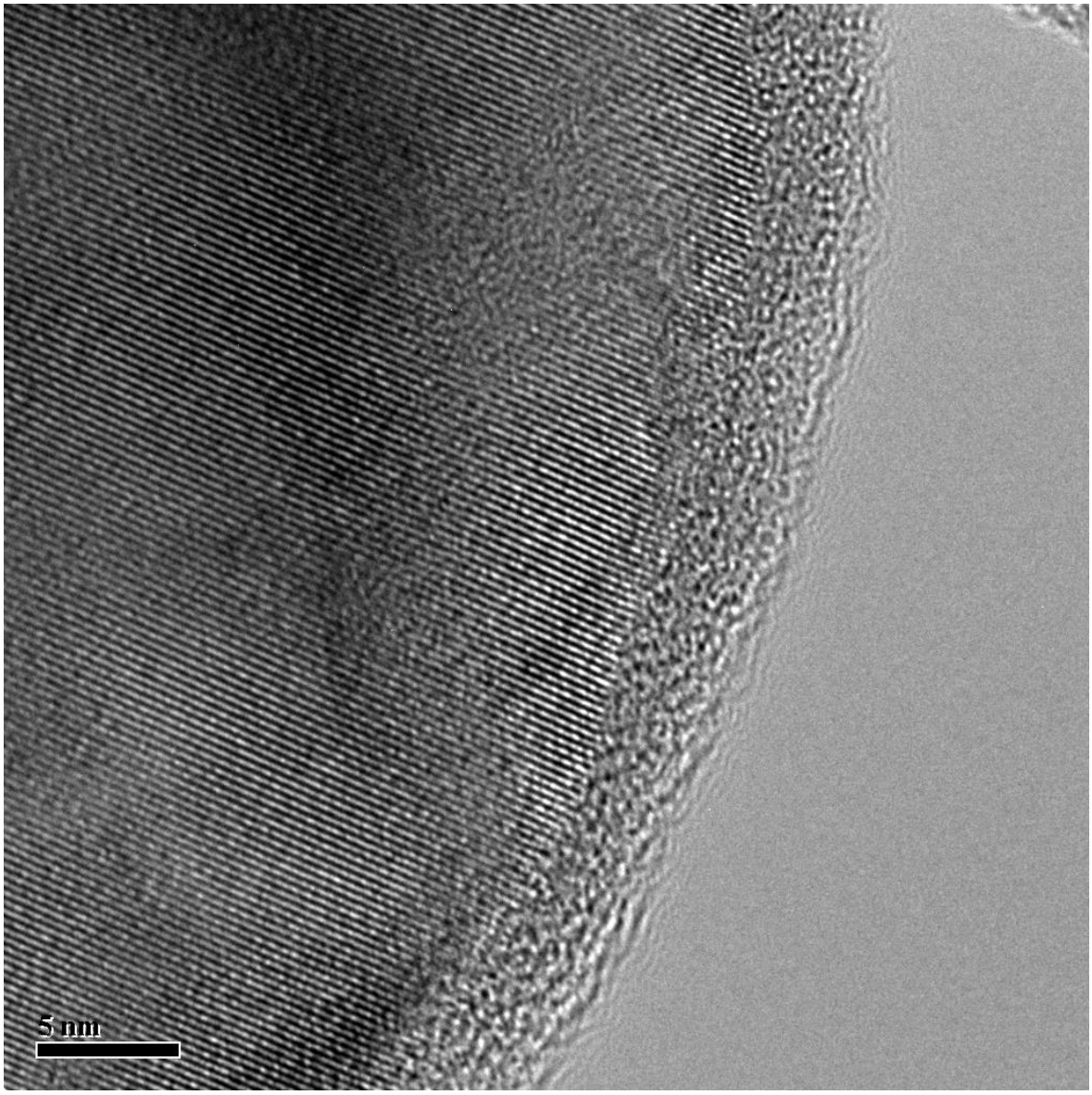


Figure 14: A high resolution TEM image of a silicon sample.

The selected area electron diffraction (SAED) equipped in many TEMs can provide a diffraction pattern of the specimen by adjusting the magnetic lenses such that the back focal plane of the lens rather than the imaging plane is placed on the imaging apparatus. Lattice information of a sample can be obtained from the SAED. Furthermore, a TEM equipped with an electron energy loss spectroscopy can select particular energy values, which can be attributed to how electrons

interact with the specimen. For instance, different elements from a specimen can lead to different electron energies in the beam after interaction with the sample. The difference in electron energy can further result in chromatic aberration, and this can be an effective approach to generate an image with the information on elemental composition of the detected sample, based upon the atomic transition during electron-electron interaction.

### 2.3 X-ray Diffraction

X-ray diffraction (XRD) is a powerful tool for determining a sample's composition and its crystalline information. In an XRD measurement (As shown in Figure 15 A), a sample is placed on top of a goniometer, which is rotated gradually while constantly exposed to incoming X-rays. Scatters of X-rays after hitting the atoms in the sample may have different scattering angles and diffractions due to different arrangements of atoms in the sample. Although in most directions the diffraction waves cancel each other out by a destructive interference, in some specific directions, diffraction waves are strengthened by a constructive interference, and this is determined by the Bragg's Law:

$$2d\sin\theta = n\lambda, \qquad (1)$$

where d is the spacing between diffracting planes, $\theta$ is the incident angle, n is the correspondent integer, and $\lambda$ is the wavelength of the beam (Figure 15 B).

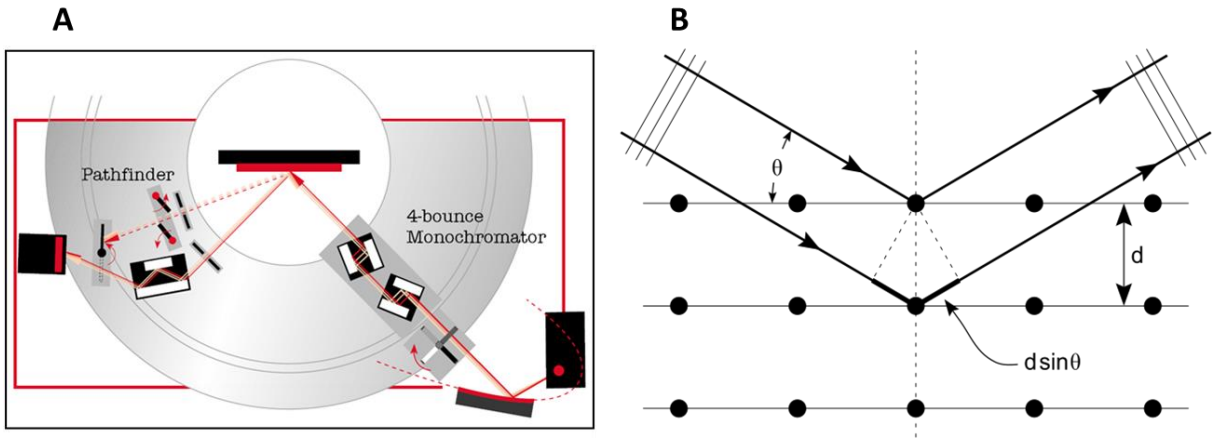


Figure 15: A schematic representation of an X-ray diffractometer (A), and a graphic illustration of the Bragg's law (B).

By measuring the angles (θ) and the correspondent beam intensities of these diffracted beams, the positions of atoms in a crystal can be determined, as well as their disorder, types of chemical bonds, and other kinds of information. XRD can be used to determine various types of sample with no tedious sample preparation. Samples for XRD can be a bulky inorganic material, biological tissues or segments including DNAs, proteins, nucleic acids, nano-sized powder materials and so on.

### 2.4 Raman Spectroscopy

Raman spectroscopy is a spectroscopic technique used to detect a system's vibrational, rotational and other low-frequency modes. As shown in Figure 16 A, When a sample is radiated by a monochromatic laser beam, both elastic scattering (Rayleigh scattering) and inelastic scattering (Stokes and Anti-stokes) are generated, while only the inelastic scattering is used in Raman spectroscopy to give Raman signals. Samples in Raman may exist in solid, liquid and also gaseous phases. A Raman set-up typically consists of several key components including a radiation source (usually a laser generator), a sample illumination system and light collection

optics, a wavelength selector (filter or spectrophotometer) and a detector, frequently functioned by a charge coupled device, photo multiplier tube or photo diode array (Figure 16 B).

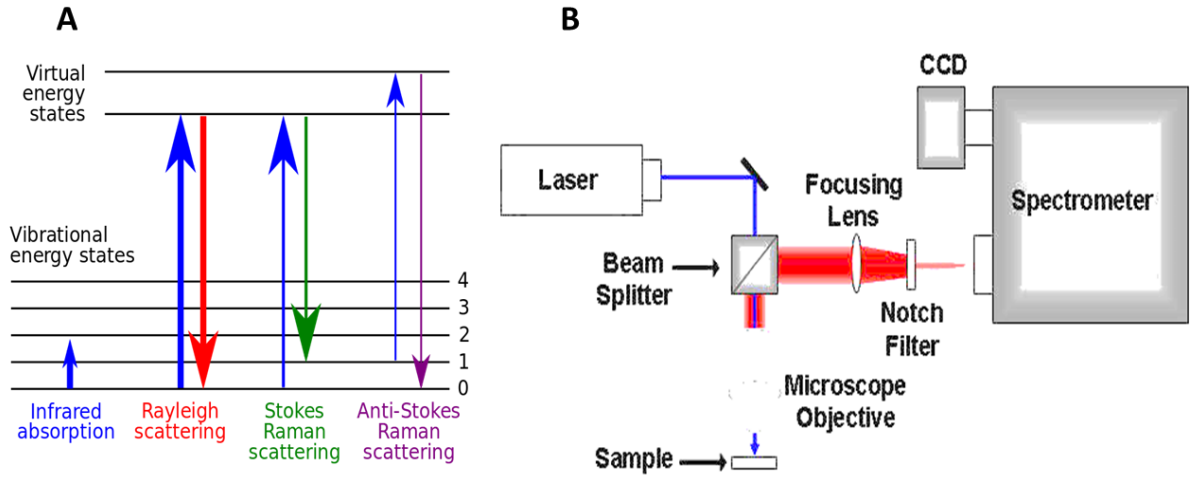


Figure 16: Different kinds of scatter in an energy diagram (A), a schematic view of Raman spectroscope.

In a Raman spectroscope, illumination laser can be in ultra-violet, visible, and also near-infrared region according to the specific requirement of different samples. Scattered light is condensed by a lens and then sent through an interference filter or spectrophotometer to obtain Raman spectrum of a sample. Around 99.999% of the scattering in a normal Raman Spectroscope is Raman-inactive Rayleigh scattering, and only the rest 0.001% is inelastic Raman scattering, which makes it very difficult for a detector to filter the useful signal from all the scattering radiation. This requires special treatment on the signals to distinguish the target Raman signal from other useless signals. Several categories of instruments including laser stop apertures, tunable filters, notch filters, spectrometric systems, double and triple are used to separate high-quality Raman spectra from strong Rayleigh scattering.

## 2.5 Fourier Transformed Infrared Radiation

Infrared light is one kind of electromagnetic radiation with a wavelength between 1 millimeter and 700 nanometers. The frequency of IR falls in the range of 300GHz to 430THz. The corresponding photon energy is from 1.4mV to 1.7eV. IR is beyond the range of visible lights for human beings. But applications of IR can be widely found in both daily life and research areas. Infrared light is generated or absorbed by the change of rotational-vibrational movements in molecules. A change in the dipole moment can reflect the corresponding vibrational mode and infrared energy, offering useful information for studying the energy states and the vibrational modes in molecules. Absorption and transmission of photons in the infrared energy range are easily examined by the infrared spectroscopy. Fourier Transformed Infrared Radiation (FTIR) spectroscopy is a kind of more advanced infrared spectroscopy. Compared to traditional IR, FTIR spectrometers have several significant advantages: (1) The scan time is greatly reduced for scanning in all frequencies (less than 1s). (2) The error in the wavelengths is much smaller. (3) The signal-to-noise ratio of spectrum is prominently improved. (4) The scan range of FTIR is dramatically enlarged. (5) The interference issue in other obsolete IRs is well addressed in FTIR. (6) The resolution of FTIR is much higher.

As demonstrated in Figure 17, a common FTIR spectrometer consists of an IR emitter, interferometer, sample compartment, detector, signal amplifier, A/D convertor, data processor and a display. The IR from the radiation source passes through the interferometer and arrived at the detector. After that, the signal is amplified and converted to digital signal by an amplifier and analog-to-digital converter. Finally, Fourier transform of the signal is realized on a computer. Below is a simplified FTIR diagram.

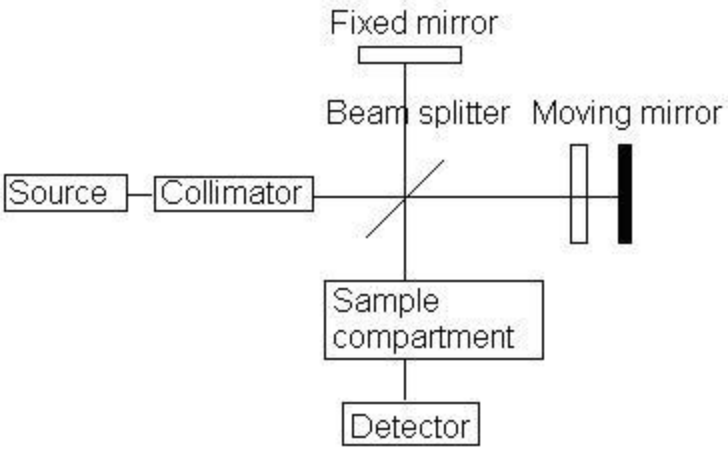


Figure 17: A simplified diagram of FTIR

Fourier transform is named after the French mathematician and physicist Jean Baptiste Joseph Fourier. It is a mathematical method to transform a function into a new function. The following equation is a common form of the Fourier transform with unitary normalization constants:

$$F(\omega) = \frac{1}{\sqrt{2\pi}} \int_{-\infty}^{\infty} f(t) e^{-i\omega t}\, dt \qquad (2)$$

where t represents time, i is the unit of imaginary number.

The equation below is another form of the Fourier transform (trigonometric function form), where imaginary number i is eliminated.

$$F(v) = \frac{1}{\sqrt{2\pi}} \int_{-\infty}^{\infty} f(t) \cos(2\pi v t)\, dt \qquad (3)$$

The equation shows the mathematical relationship between F(v) and (t), and is in the form of Fourier transform.

$$f(t) = \frac{1}{\sqrt{2\pi}} \int_{-\infty}^{\infty} F(v)\cos(2\pi vt)\, dv \qquad (4)$$

Fourier Transform of Interferogram to Spectrum:

The original signal from the interferogram is time domain since it is a function of time. After the Fourier transformation, a spectrum represented by frequency domain is obtained. Figure 18 shows the Fourier transform spectrum from an interferogram of a polychromatic light.

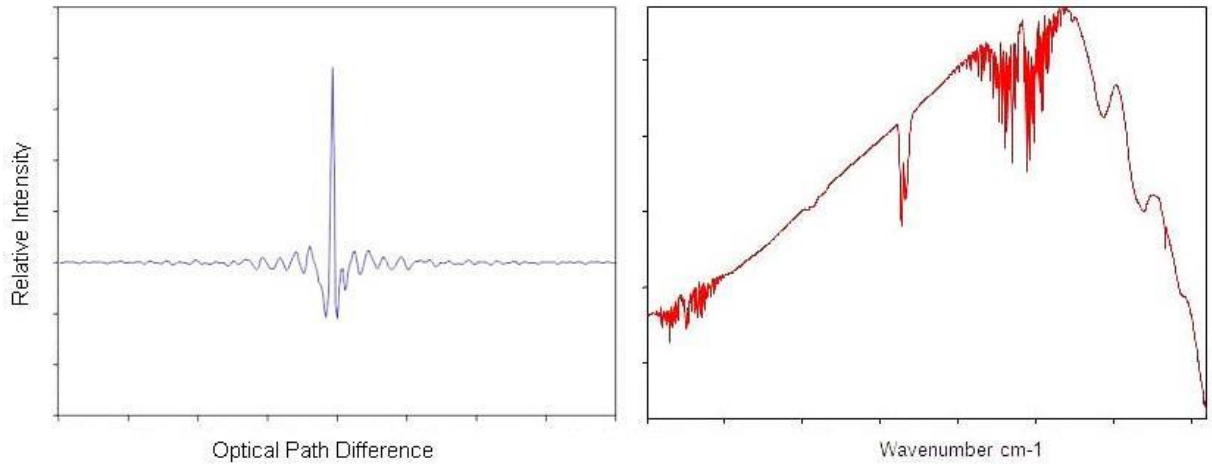


Figure 18: An example of Fourier transform from original signal to FTIR spectrum.

### 2.6 Thermogravimetric Analysis

Thermogravimetric analysis (TGA) is used to measure thermal properties of a sample by increasing the sample's temperature at a set rate in a specific atmosphere. A typical TGA apparatus contains a precise balance, a thermo-tolerant sample pan, and a programmable furnace. It can provide information of a sample such as its melting point, boiling point, dehydration temperature, combustion temperature, and composition of a sample with several components. For example, in this thesis, the mass ratio of silicon in Si-G composites can be obtained by a TGA test. The sample is put into a TGA burning chamber in atmosphere, and the final

temperature is set to be 900° C. The ramp rate is set to be 10 ℃/min. As the temperature increases, graphene is first burned away since it has a lower burning temperature than silicon. There is a steep drop on the mass-temperature curve, and from the minimum of the curve the mass ratio of silicon in the whole composite can be observed. Since the sample only contains two ingredients, the mass ratio of graphene can also be obtained by deducting the mass ratio of silicon from a 100%.

### 2.7 Lithium Ion Battery Evaluation

To evaluate the electrochemical properties of the synthesized material, lithium ion coin cells (CR2032) are fabricated. Electrode fabrication methods in this thesis vary according to different materials; electrode compositions are also based on the characteristics and requirements of different materials. In the Si-G project, electrodes were fabricated using a doctor-blade cast, with an electrode composition of 6:2:2, *i.e.* 60% active material: 20% super-P： 20% polyvinylidene fluoride (PVDF) binder. In other silicon projects, carboxymethyl cellulose (CMC) binder is adopted instead of PVDF. The ratio of active material, binder, and super-P also varies from project to project. In the project where Si-GO was reduced at a low temperature, electrodes are first fabricated with a ratio of 60% Si-GO, 20% super-P, and 20% binder, and the binder is 2%V/V CMC solution. The electrodes were heated in a vacuum oven at 150 degrees Celsius for drying, and at the same time, GO is reduced to graphene and CMC binder is cured.

Unlike the silicon projects, active material is directly deposited on the current collector and substrate directly during the synthesis process in the $Co_3O_4$ project, and no binder or additional conducting material is used in the electrode fabrication.

Electrochemical tests include constant current charge and discharge, which can obtain the cycling performance and the profile data of charge and discharge process. Rate capability data of an electrode can be obtained when different currents are applied in the charge and discharge tests. Cyclic voltammetry is used to study the characteristic peaks of electrode reactions. In some projects, electrochemical impedance spectroscopy is used to study the internal resistance of batteries to evaluate the property of electrode materials.

# 3.0 Effects of graphene on the performance of silicon based anode materials in LIBs



## 3.1 Introduction and purpose of study

Silicon has been considered as the anode material for next generation lithium ion batteries with high energy density because of its high theoretical specific capacity, reaching 4200 mA h $g^{-1}$ at full lithiation (Si-Li alloy, $Li_{22}Si_5$).[142,143] This is highly favourable compared to the graphite anode materials used in current Li-ion batteries, which exhibit theoretical capacity of only 372 mA h $g^{-1}$ and low energy density. Unfortunately, the high specific capacity of Si is accompanied by substantial volume expansion and contraction during the lithiation/delithiation of silicon (>300%), which results in poor cycling stability due to the rapid pulverization of silicon electrodes, disconnection of electrical contacts, and instability of the solid electrolyte interphase (SEI).[33,123-125,144] To successfully develop next-generation lithium-ion batteries containing Si anode materials and offering long cycle life, it is critical to develop a strategy to either accommodate or restrict this volume change and form a stable SEI layer. One approach has been explored to engineer silicon nanostructure, including the development of silicon nanowire,[106] silicon nanotube,[130] hollow silicon nanoparticle,[145] and nano-porous silicon.[146] Another effective strategy is to apply carbon coatings on silicon, which can not only accommodate the volume change of silicon, but also enhance the electric conductivity of the electrode and contribute to a stable SEI layer.[147-153]

Graphene, a two-dimensional structure composed of carbon atoms, has garnered remarkable attention due to its unique structure and properties, such as: excellent electrical conductivity, high surface area, good flexibility and high mechanical strength.[154-157] As an anode material for LIBs, graphene has demonstrated promising performance compared to graphite and more recently Si-G materials have been shown to alleviate the issues associated with bare Si.[67,118,158-160] However, it remains a challenge to evenly disperse Si within the graphene sheets. As a result, it is difficult to form stable composites and lithium diffusion could be hindered by sluggish ion diffusion within the poorly distributed composite materials.[161-163]

In this work, we synthesized Si-G composites with a freeze-drying method in order to combine the merits of Si, graphene and freeze drying. We believe that an effective strategy for the production of uniformly dispersed Si-G composites is to reduce graphene oxide (GO) to graphene after mixing with silicon. This is attributed to graphene being very hydrophobic and thus difficult to disperse in aqueous solution, while GO is highly hydrophilic and Si-NPs are slightly hydrophilic due to the native oxygen functionality on the surface of Si. However, the agglomeration of nano-sized silicon caused by the surface tension when drying in aqueous solution can also lead to inadequate composite performance.[164] Freeze-drying has been reported as an effective way to fabricate three-dimensional (3D) architectures and aligned structures, avoiding the agglomeration that commonly occurs during drying.[165,166] After the Si and GO are well dispersed in water, the mixture is frozen immediately with liquid nitrogen so that GO and silicon nanoparticles can maintain their original morphology. Then the water is sublimated to vapour phase directly in a freeze-dryer, and a 3-D network of graphene wrapping silicon is

formed by the following heat treatment. The 3-D structure will benefit LIBs in terms of easier lithium ion transportation, faster electrolyte diffusion, as well as better retention of its structure during cycling. In a previous communication published by Zhou *et al.*, one ratio of Si-G composite was synthesized by the freeze drying method and tested in LIBs.[166] However, advanced study for an optimal composition of Si-G is suggested to improve cycle stability and investigate the trade-off between capacity and stability. We systematically investigate the impact of varying the graphene content on the performance of Si-G composites in LIBs, in order to obtain an optimal Si to graphene ratio with enhanced cyclic stability and high specific capacity. All composites had improved stability compared to bare Si-NPs, but most notable was the superior cyclic stability and rate capability of the composite employing a starting ratio of 1:2 (Si-NP:GO). The 3D architecture of the Si-G 1:2 composite materials reveal capacity retention after 200 cycles was 96% @ 0.2 C and around 100% @ 1C, corresponding to 786.3 mA h $g^{-1}$ and 594.6 mA h $g^{-1}$ respectively. We believe that the graphene wrapped silicon will maintain the electrical connection even if the fracture and pulverization occur in silicon due to diffusion-induced stress exceeding the fracture strength. At the same time, the silicon particles are most likely isolated from the electrolyte, so that the majority of SEI will form just on graphene surface which would not go through the huge volume expansion and contraction along with Si. As a result, the cycle efficiency can be improved. In addition, hydrofluoric acid (HF) has been widely used to remove the $SiO_X$ layer on pristine silicon,[167-169] but recent studies have shown that an amorphous $SiO_X$ layer can help prevent the electroactive silicon from agglomerating during cycling. More importantly, the $SiO_X$ also form lithium silicate during cycling ($Li_2Si_2O_5$), which can function as a buffer layer to reduce the damage to and restrict the volume expansion of Si and stabilize the SEI layer.[160] For these reasons and to increase cost effectiveness of the material,

HF treatment was avoided. In addition, no expensive electrolyte additives, such as vinylene carbonate (VC) and fluoroethylene carbonate (FEC) were used in the electrolyte.

### 3.2 Experimental methods

Figure 19 schematically shows the process to synthesize the Si-G nanocomposite. Silicon nanoparticles (Si-NPs) (Nanostructured & Amorphous Materials Inc, USA. 50-70 nm) were sonicated in water for five hours. Meanwhile, graphene oxide (GO) synthesized by a modified Hummers' method was sonicated separately for five hours as well. Detailed procedures for the fabrication of GO were described in a paper previously published by our group.[170] The two suspensions were then mixed and sonicated for another five hours to achieve a thorough dispersion. Next, the mixture was frozen rapidly with liquid nitrogen and a freeze-dryer (Labconco Freezone 1, USA) was subsequently used to freeze dry the sample for 48 hours, retaining its as-frozen shape. Then the Si-GO composite was pyrolysed under an argon atmosphere with 10% hydrogen at a flow rate of 70 $cm^3$ $min^{-1}$, purging for 30 min before the furnace was turned on. Finally, the sample was heated up to 700 $^oC$ @ 0.5 $^oC$ $min^{-1}$ and held for 3 hours to generate the final graphene-wrapped silicon composites. Characterization of the graphene formation and Si stability in the as-prepared Si-graphene composites was studied by X-ray diffraction (XRD). Field Emission Scanning Electron Microscopy (FESEM) (Zeiss Ultra Plus, UK) and Transmission Electron Microscopy (TEM) (FEI Philips CM300, USA) were utilized to obtain the morphology and further reveal the structure of the composites. Thermoravimetric Analysis (TGA) (TA instrument Q500, USA) was used to determine Si/G mass ratio in the composites. TGA testing was performed in air with a temperature range of 25 $^oC$ to 900 $^oC$ and a ramp rate of 10 $^oC$ $min^{-1}$.

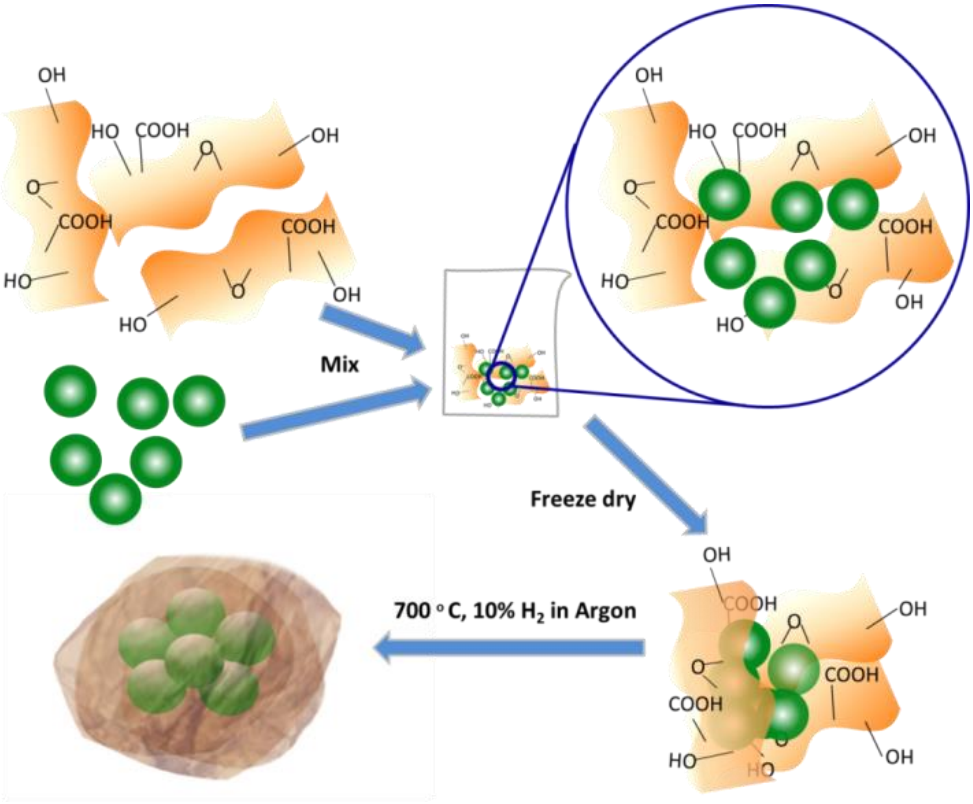


Figure 19: Schematic view for synthesis of the Si-G composites.

To study the balance between the high capacity of Si and the cycle stability of graphene, as well as optimizing battery performance, graphene-wrapped silicon composites were prepared by varying the ratios of the starting materials. The initial Si:GO ratios tested include 1:3, 1:2, 1:1 and 1:0.5, in addition to pure GO and bare Si-NP. The graphene-wrapped composites produced will be further referred to as Si-G 1:3, Si-G 1:2, Si-G 1:1, and Si-G 1:0.5, respectively. Coin cells (CR 2032) were fabricated to study the electrochemical properties of the nanocomposites using a slurry containing: 60 wt% of the active composite material, 20 wt% Super P carbon black as a conductive material, and 20% polyvinylidene fluoride (PVDF). Lithium metal (Aldrich, USA) was used as a counter/reference electrode. The electrolyte was a 1 M $LiPF_6$ solution with a mixture of ethylene carbonate (EC)/dimethyl carbonate (DMC) (3:7) as a solvent, with no

additives. The two electrodes were separated by a polypropylene membrane (high porosity, 20 μm micro porous, Celgard PP2075, USA) and assembled in an argon-filled glove box (MBRAUN 10, USA). Charging and discharging of cells was conducted on battery testing equipment (Neware, China), employing a cut-off voltage range from 0.05V to 1.5 V. Cyclic voltammetry (CV) was conducted on an electrochemical station (Versa Stat MC, Princeton Applied Research, USA) with a scanning rate of 0.1 mV $s^{-1}$. All tests above were conducted at room temperature.

### 3.3 Results and discussion

The SEM analysis in Figure 20 demonstrates the 3D morphology of the synthesized Si-G composites, depicting the well-distributed Si-NP encapsulated by the graphene after freeze-drying and reduction. For Si-G 1:3, shown in the Figure 20 (b) image, the Si-NPs (homogenous 50-70 nm size distribution, (shown in Figure 20 (f)) are scarcely distributed on and under the graphene sheets. Meanwhile, Si-G 1:2 clearly displays a larger Si content and the graphene wrapping is more visible in Figure 20 (c). As the amount of Si-NPs in the starting material increases, the Si clusters within the composite become denser (Figure 20 (d, e)). Interestingly, despite the low graphene content in Si-G 1:0.5, the composite still forms small 3D clusters of Si-NPs wrapped by the graphene. The SEM image in Figure 20 (a) shows the morphology of a graphene only sample, produced by the same procedure as the Si-G composites. The extensive graphene wrinkling and sharp folds may offer a large number of ideal anchoring sites for silicon nanoparticles during reduction.

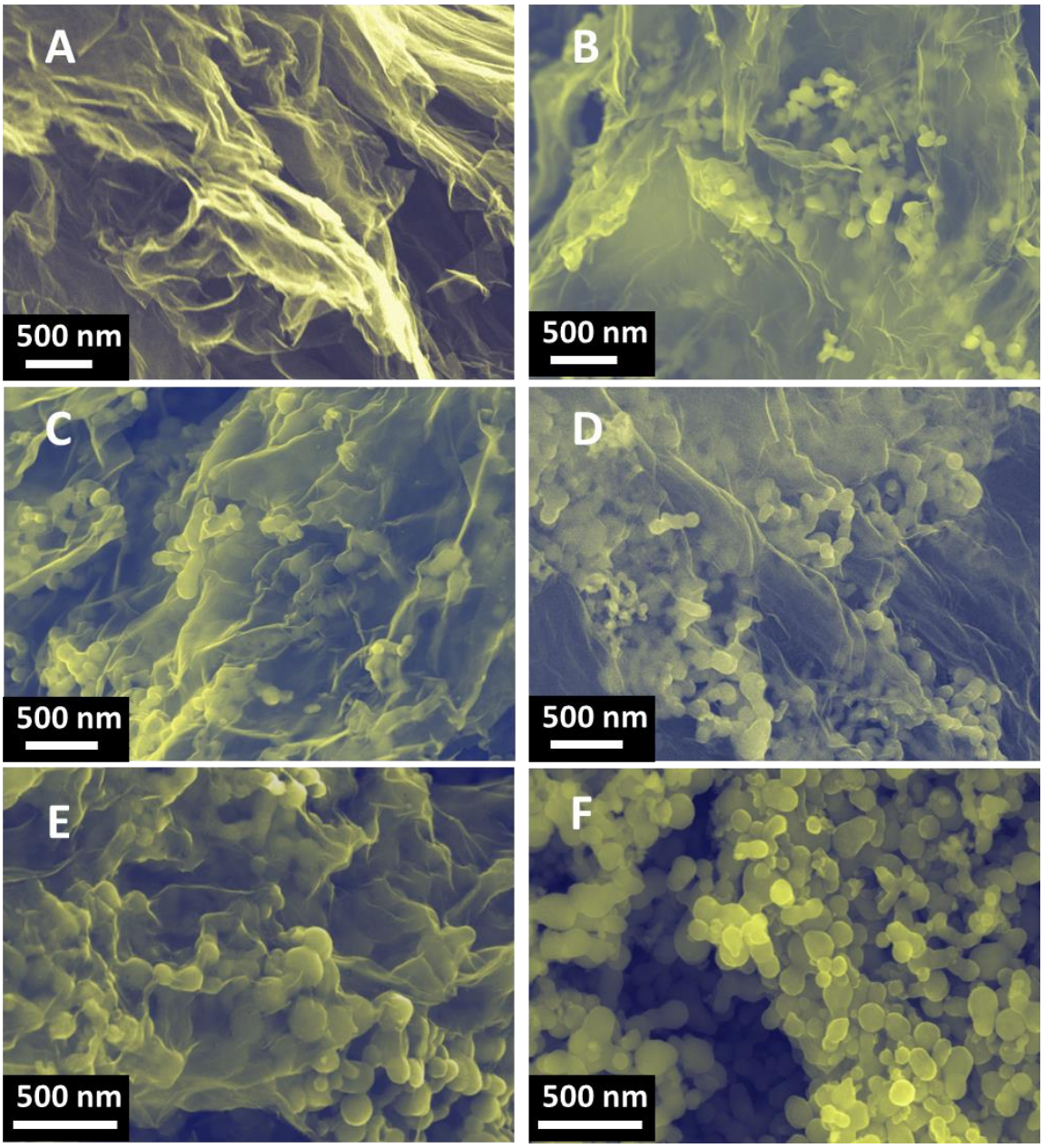


Figure 20: SEM images of (a) graphene, (b) Si-G 1:3, (c) Si-G 1:2, (d) Si-G 1:1, and (e) Si-G 1:0.5, (f) bare silicon nanoparticles.

To further illustrate the morphology of the as-obtained composites, TEM images were taken and shown in Figure 21. Both the Si-NPs and wrinkled graphene sheets can be clearly seen. Analysis of Si-G 1:2 highlights the sparse Si-NPs, with minimal overlap, anchored to the graphene sheet

in Figure 21 (a). However, the Si-NPs in Si-G 1:1 were dense and relatively clustered within the graphene sheets (Figure 21 (b)). Retention of the wrapped structure despite the extended sonication required for sample preparation suggests the Si-G composites exhibit a certain degree of structural integrity.

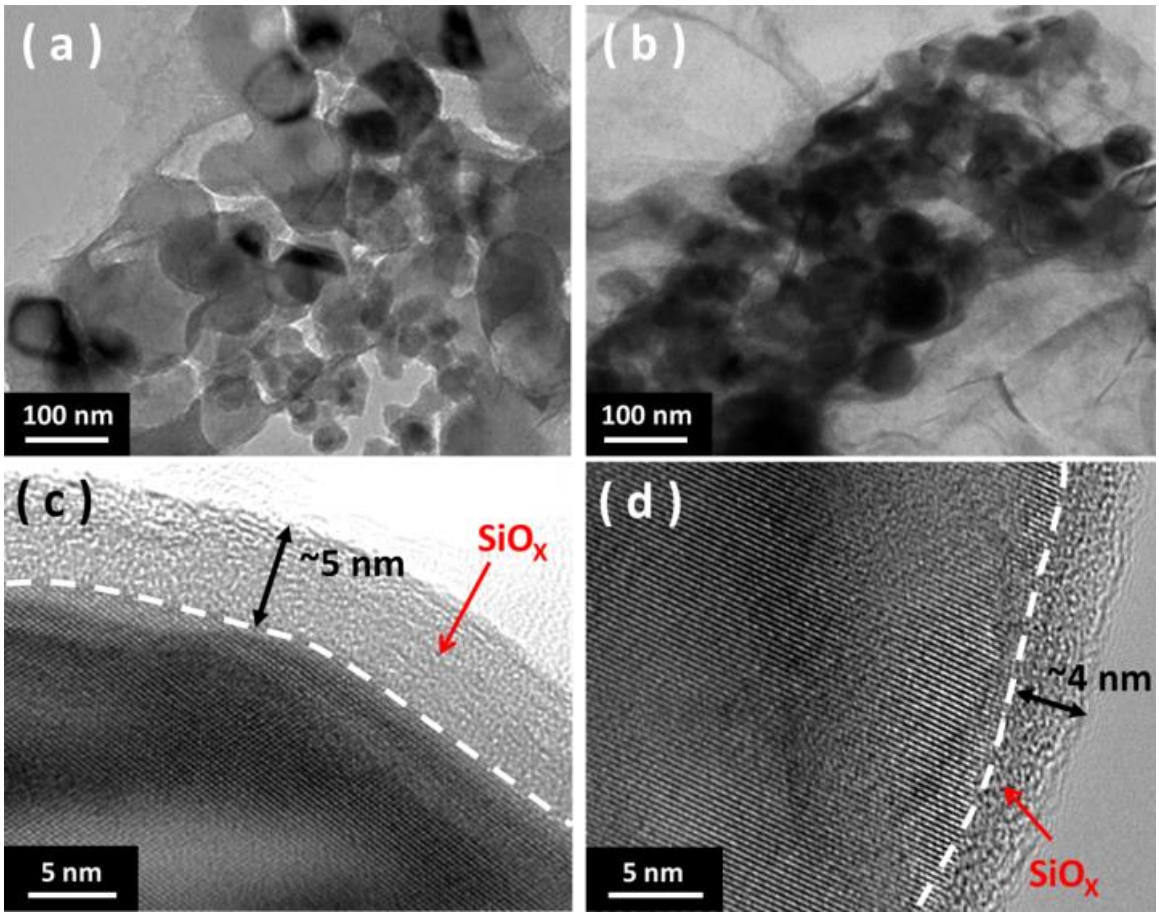


Figure 21: TEM images of Si-G 1:2 (a) and Si-G 1:1 (b), and HRTEM images of the surface of Si in Si-G 1:2 (c) and Si-G 1:1 (d).

It is proposed that the re-stacking nature of graphene sheets, initiated by increased Van der Waals force during reduction from GO, leads to the novel morphology illustrated in Figure 22. In contrast, intercalated silicon nanoparticles in GO layers also prevent graphene sheets from

further restacking, facilitating the electrolyte diffusion.[171-173] High resolution TEM (HRTEM) (Figure 21 (c) and (d)) was used to further characterize the surface of the Si-NPs after treatment to form Si-G 1:2 and Si-G 1:1. A distinct boundary between the crystalline Si core and an amorphous $SiO_x$ layer can be easily observed in both composites. A slightly thicker layer of $SiO_x$ can be seen in Si-G 1:2, which can be attributed to the higher content of oxygen in the starting material. Apart from the difference of silicon content in these two composites, the amount of $SiO_x$ can also partially explain why the capacity of Si-G 1:2 is lower than that of Si-G 1:1.

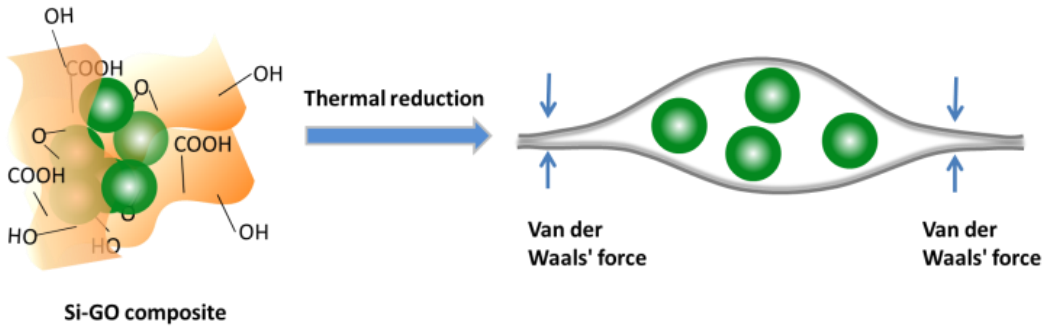


Figure 22: Hypothetic illustration of formation process of 3-D Si-G composites.

XRD was carried out to determine if any side reactions occurred during preparation of the composites. Figure 23 (a) shows the diffraction pattern of the as-prepared Si-G 1:2 composite, which is closely match to: the crystalline peaks for Si and the characteristic broad peak for graphene at 26.7°.[174] The remaining peaks can be attributed to characteristic peaks of the aluminum holder showing through the composite samples. The absence of any additional unassigned peaks confirms that no silicon carbide was formed during heat treatment and the lack of a $SiO_2$ pattern suggests most of the Si remains un-oxidized.[175]

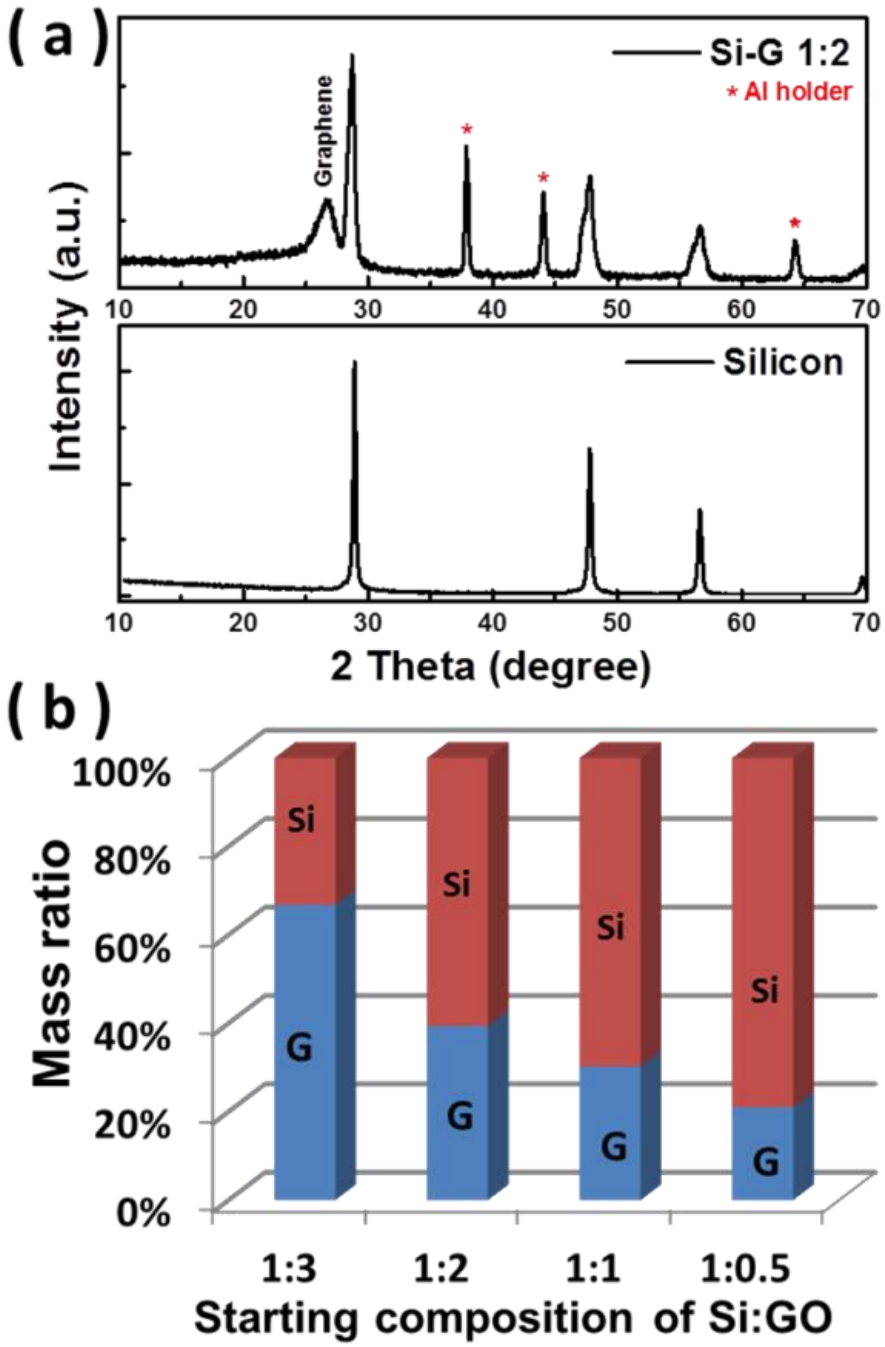


Figure 23: XRD patterns of Si-G 1:2 and Si (a). TGA results of Si-G composites with different ratios of silicon and graphene (b).

The other composites were also examined by XRD (Figure 24), and they shared a spectrum similar to Si-G 1:2. Some variation in the peak intensities of graphene and silicon was observed due to the different ratios of silicon and graphene in these composites. Then, TGA analysis was used to more accurately determine the ratio of graphene to silicon within the various Si-G composites, after removing the majority of the oxygen functional groups from GO during the reduction process. The results shown in the Figure 23 (b) illustrate the ratio of silicon in composites increases from 33.2% (Si-G 1:3) to 79.0% (Si-G 1:0.5) as the amount of Si in the starting materials increases.

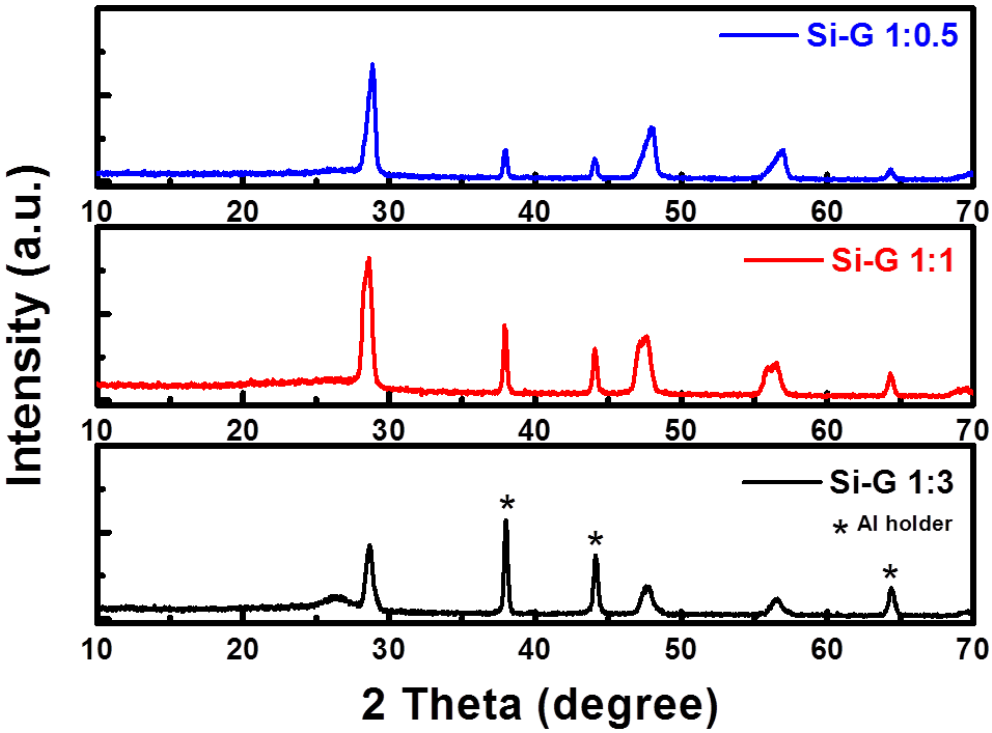


Figure 24: XRD patterns of Si-G 1:0.5, Si-G 1:1 and Si-G 1:3.

Galvanostatic measurements were conducted on each of the Si-G composites (Figure 25). The cut-off voltage range for all tests was from 0.05V to 1.5V, and the current used for the first three cycles was 100 mA $g^{-1}$ based on the total mass of the active materials, graphene and Si. In the first discharge, decomposition of electrolyte on the composite surface to form the SEI layer is confirmed by a small plateau region at 0.8V, which is no longer present in later cycles.[176] Further, a flat plateau at around 0.1 V appears in every material's profile curve, which corresponds to the characteristic discharging voltage of silicon in a half cell.[177] As shown in Figure 26, over 90% of the bare Si-NP electrode's first discharge capacity exists within the characteristic region. However, with decreasing Si content in the Si-G composite, the capacity contribution of this 0.1V plateau during first discharge decreases from ~80% (Si-G 1:0.5) to only ~25% (Si-G 1:3). Prominence of the slope between 0.8V and 0.1V can be attributed to the change in graphene content, which exhibits a nearly continuous slope below 0.8V and the cut-off potential (Figure 26 (a)).[178] First cycle discharge efficiencies of the composites in order of decreasing graphene content are 40.9%, 46.4%, 54.0% and 63.0% respectively, indicating that first cycle efficiency and total discharge capacity are sacrificed in order to improve cycle stability. Table 2 provides detailed information about the first cycle data obtained. The reduced efficiency can be attributed to graphene's intrinsic properties and limitation of the graphene capacity imposed by the cut-off voltage (0.05 V-1.5 V).[179] It is important to note that the charge capacity of both Si-G 1:2 (Figure 26 (c)) and Si-G 1:1 (Figure 26 (d)) increased during the initial cycles, likely due to the continued activation of the Si, while that of the unstable bare Si-NPs drops significantly and pure graphene decreases only slightly. This increase in charge capacity demonstrates the successful accommodation of silicon's volume change within the optimally wrapped Si-G composites.

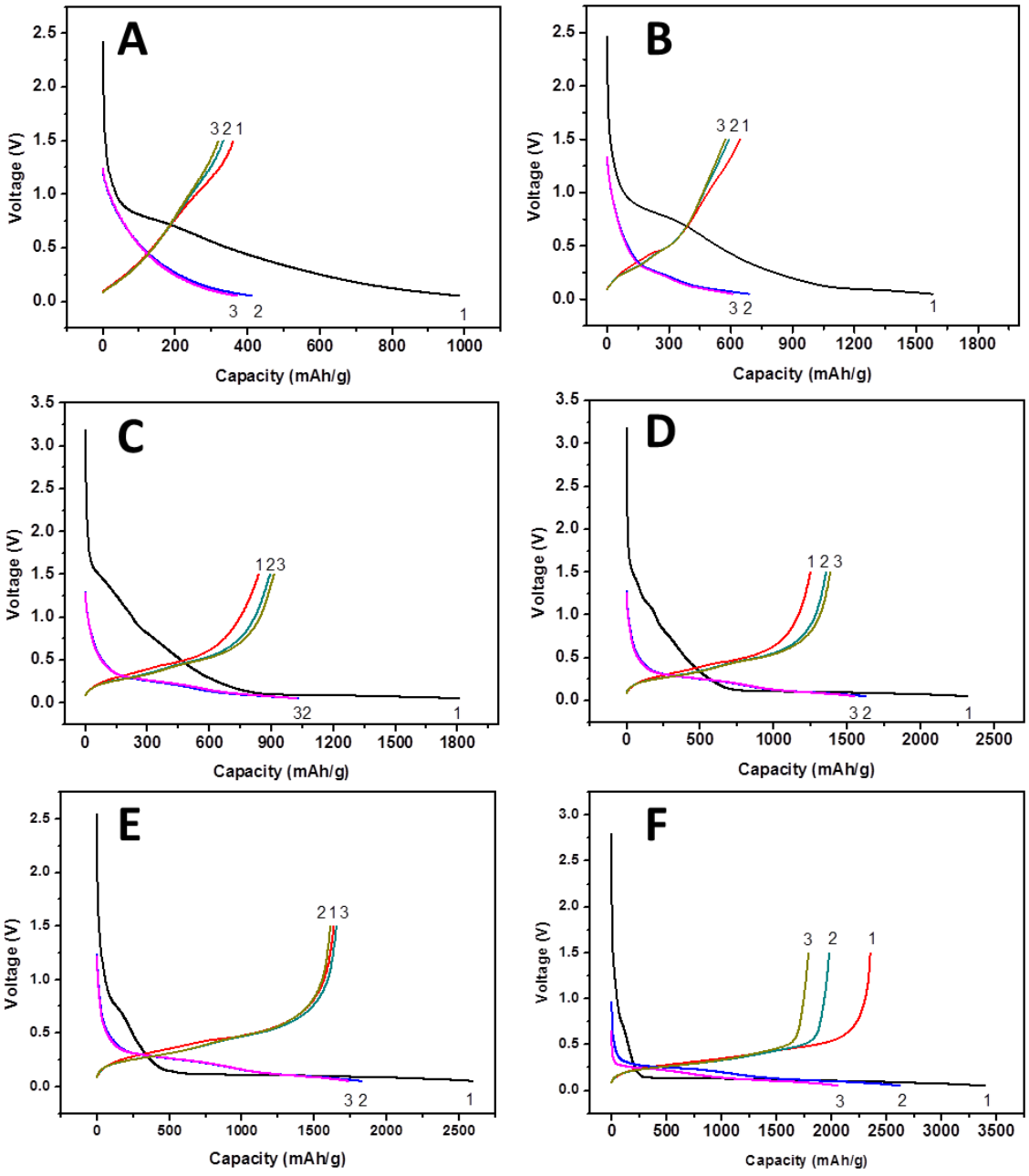


Figure 26: Charge and discharge profiles of the first three cycles from: (a) graphene, (b) Si-G 1:3, (c) Si-G 1:2, (d) Si-G 1:1, (e) Si-G 1:0.5, and (f) bare silicon, tested at 100 mA $g^{-1}$.

Table 2: Discharge/charge capacities, coloumbic efficiency of the first cycles at 100 mA g-1, as well as capacity retention after 100 cycles at 0.2 C; for each of the composites tested.

| **Composite Type** | **Discharge capacity (mAh/g)** | **Charge capacity (mAh/g)** | **Coulombic efficiency** | **$100^{th}$ cycle capacity retention** |
|---|---|---|---|---|
| G | 985.0 | 360.8 | 36.6% | 78.2% |
| Si-G 1:3 | 1310.2 | 514.7 | 39.3% | 55.5% |
| Si-G 1:2 | 1806.2 | 837.7 | 46.4% | 103.3% |
| Si-G 1:1 | 2312.4 | 1248.8 | 54.0% | 78.7% |
| Si-G 1:0.5 | 2599.2 | 1636.5 | 63.0% | 15.7% |
| Si | 3499.3 | 2356.1 | 67.3% | 2.5% |

To study long-term cycling stability of the Si-G composites, batteries were adjusted to cycle at 0.2 C, based on the capacity of each material after 5 cycles at 100 mA $g^{-1}$ (Figure 27). The corresponding 1 C rates adopted were 300 mA $g^{-1}$, 500 mA $g^{-1}$, 900 mA $g^{-1}$ ,1300 mA $g^{-1}$, 1500 mA $g^{-1}$, and 1500 mA $g^{-1}$ for graphene, Si-G 1:3, Si-G 1:2, Si-G 1:1, Si-G 1:0.5, and Si-NP, respectively. Figure 27 (a) shows that both Si-G 1:1 and Si-G 1:2 are promising composites in terms of specific capacities and cycling stability, in contrast to the limited Si capacity contribution to Si-G 1:3 and inferior cycle stability of Si-G 1:0.5.

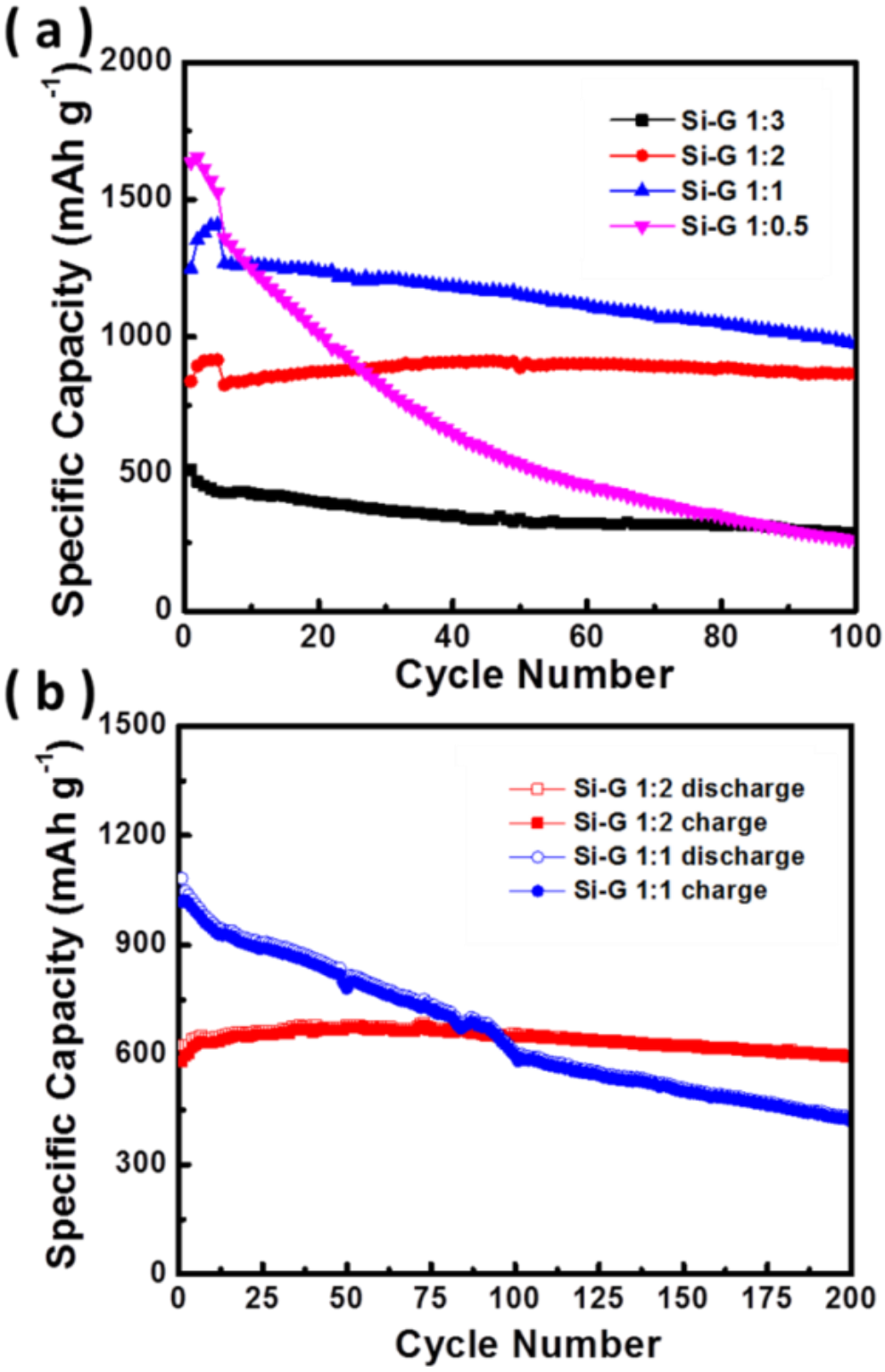


Figure 27: Long-term cycling performance for all composites at 0.2 C (a) and 1 C rate data for Si-G 1:2 and Si-G 1:1 (b).

From SEM, the low graphene content in Si-G 1:0.5 left many of the Si-NPs uncovered and less void space was available to allow sufficient Si expansion. This helps to explain, why, after 100 cycles at 0.2 C the capacity decreases to 257 mA h $g^{-1}$(15.7% of initial reversible capacity). Still, Si-G 1:0.5 offers much better cycling performance than the bare Si-NP (Figure 28) which degraded to a specific capacity of ~60 mA h $g^{-1}$ after only 100 cycles.[125,180] This shows that the graphene in the composite helps improve the cycling stability of the battery, but due to the limited amount of graphene, the capacity still fades quickly. With the increase of graphene content in the composite, the cycling stability increased. Si-G 1:1 presents much better stability and higher capacity than Si-G 1:0.5 after cycling, with a capacity of 982.8 mAh $g^{-1}$ and capacity retention of 78.7% (Figure 27(a)). Optimal stability was observed for Si-G 1:2 which produced a specific capacity of 865.2 mA h $g^{-1}$ after 100 cycles. Remarkably, this was higher than the initial charge capacity and a significant improvement over the theoretical capacity of graphite (372 mA h $g^{-1}$) and the stabilized graphene after 100 cycles (~280 m Ah $g^{-1}$, Figure 28). In addition, the composites capacity after the 5th cycle (Si:GO 1:2, 824 mAh $g^{-1}$) exceeds that of the estimate determined from the summed capac ity of bare graphene and bare silicon, based on their mass ratios in the optimized Si:GO 1:2 composite (779 mAh $g^{-1}$). This demonstrates the synergistic effect between Si NPs and graphene, leading to excellent cycle stability for the composite. The capacity increase during cycling can be attributed to gradual reorganization of Si structure during the insertion/extraction process,[159,181] enabling activation of additional Si for future cycles. Lately, Xin *et al.*, presented the 3D Si/graphene composite by a direct synthesis of Si nanoparticles on graphene sheets followed by spray drying to form 3D morphologies.[159] They demonstrated the effectiveness of the 3D architecture of Si/graphene composite on the cycle

stability by comparing with the nanosheets of Si/graphene. However, they showed the stability with only 30 cycles at 100 mA $g^{-1}$.

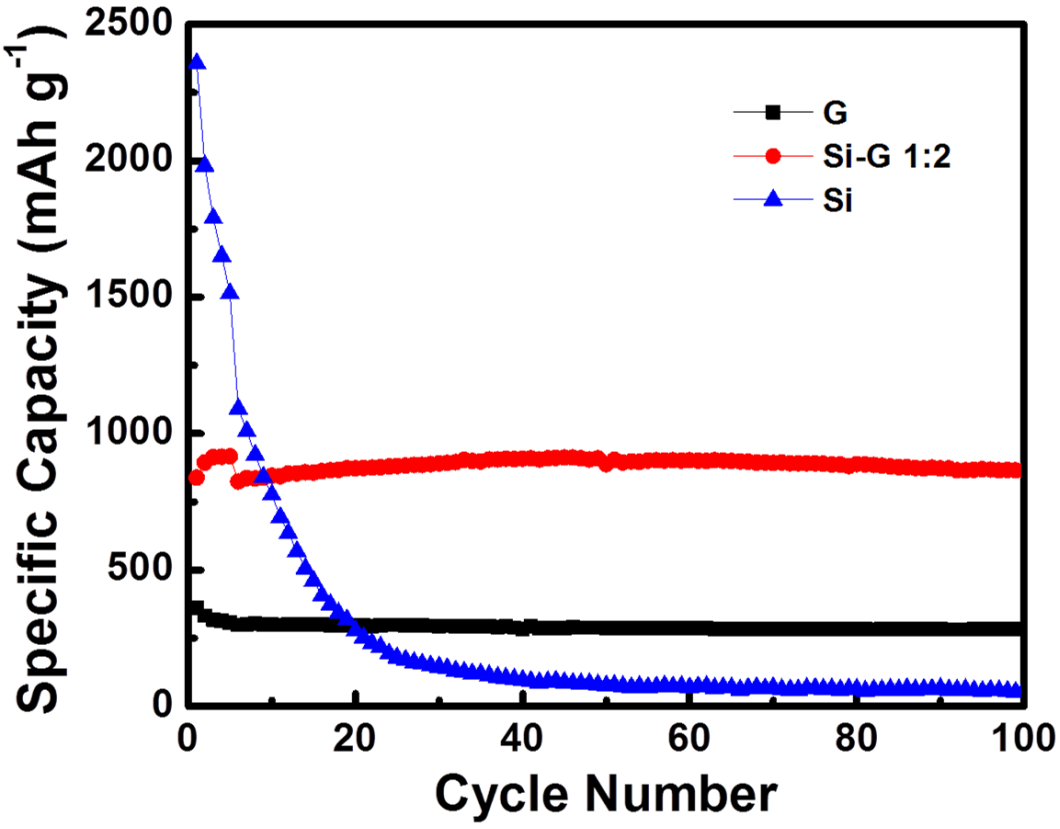


Figure 28: Long-term cycling performance for Si-G 1:2, silicon and graphene at 0.2 C.

To support the effectiveness of controlling the Si-G mass ratio, correlation of surface areas between Si and graphene is considered. The optimum performance and cycle stability may be surface area dependent, as the graphene sheets provide the charge transport pathways and active sites. In light of the surface area measurement for these materials, graphene has a specific surface area of 483.4 $m^2$ $g^{-1}$, and silicon nanoparticles have a specific surface area of 18.5 $m^2$ $g^{-1}$, according to $N_2$ adsorption–desorption isotherms (Figure 29). Taking the mass ratio of graphene

and Si in each composite into account, the specific surface area ratios of graphene to silicon are 52.6, 17.0, 11.3, 6.9 for Si-G 1:3, Si-G 1:2, Si-G 1:1 and Si-G 1:0.5 respectively.

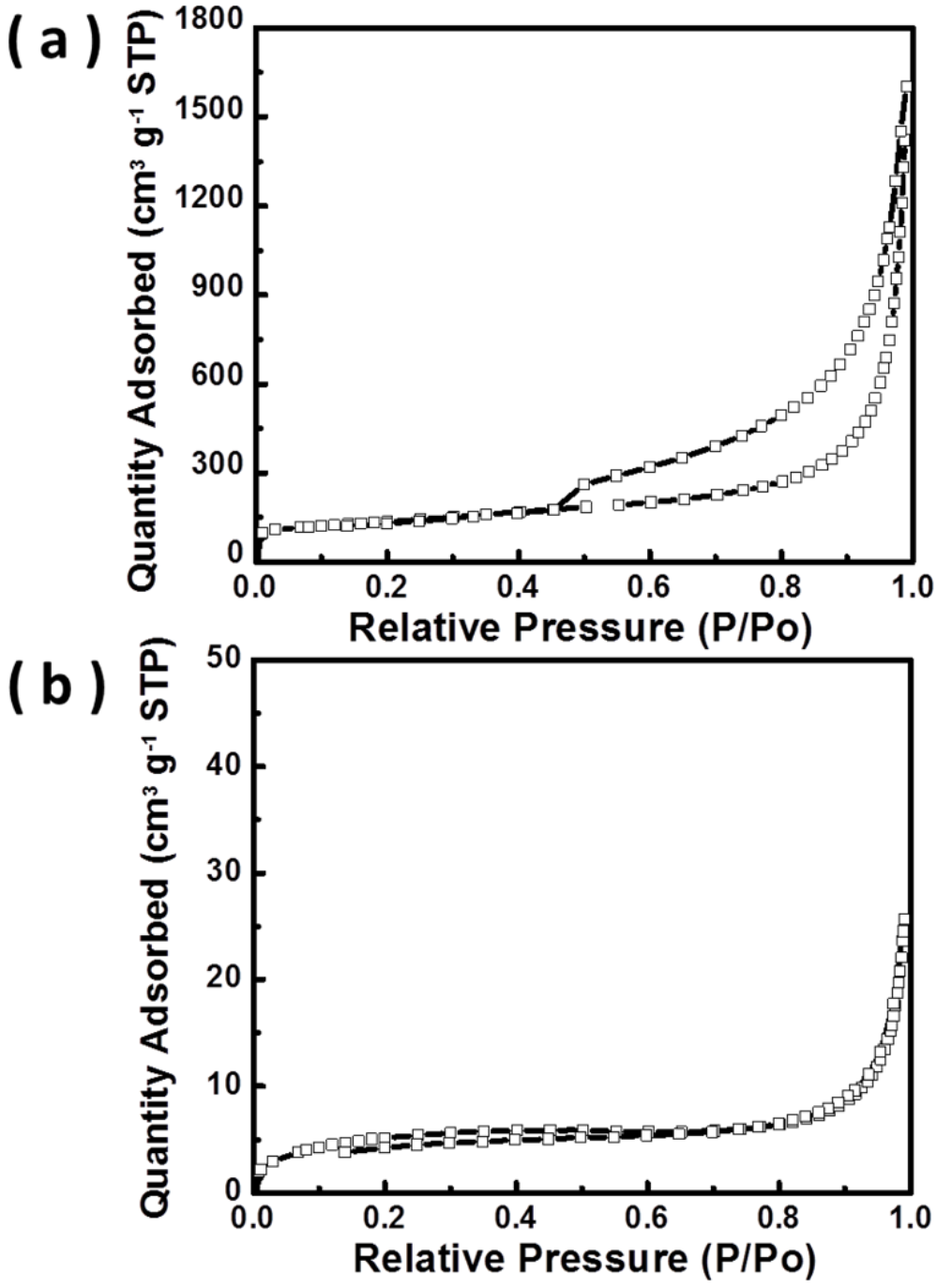


Figure 29: $N_2$ adsorption–desorption isotherms of graphene (a) and Si-NP (b)

From the performance of the composites in this study, Si-G 1:2 with the graphene-silicon surface area ratio of 17.0 shows the best performance. This alludes to the optimum surface area ratio for Si-G composites, relevant to Si particles of varying size and different graphene precursors used for future study. Further, after 200 cycles, Si-G 1:2 (96% retention) had higher capacity than that of Si-G 1:1 (58.7% retention), intersecting after 165 cycles at the 0.2 C rate (Figure 30).

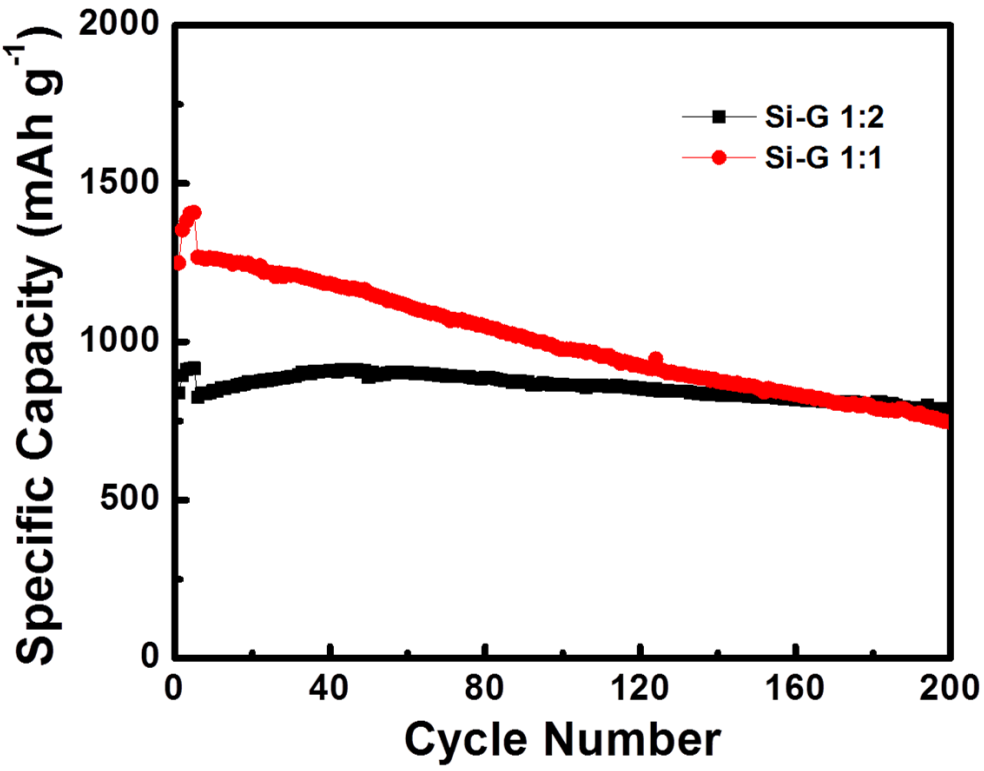


Figure 30: Long-term cycling performance for Si-G 1:1 and Si-G 1:2 at 0.2 C.

The Si-G 1:2 and Si-G 1:1 composites were also both tested at a high rate of 1 C, and the results are shown in Figure 31. The results in Figure 27 (b) and Figure 28 show Si-G 1:2 had excellent capacity retention, specific capacity increased for the first 50 cycles and remained stable at 600

mA h $g^{-1}$ for the 200 cycles tested. However, the stability of Si-G 1:1 suffered at the increased rate, capacity retention decreased to 42% of the initial reversible capacity after 200 cycles.

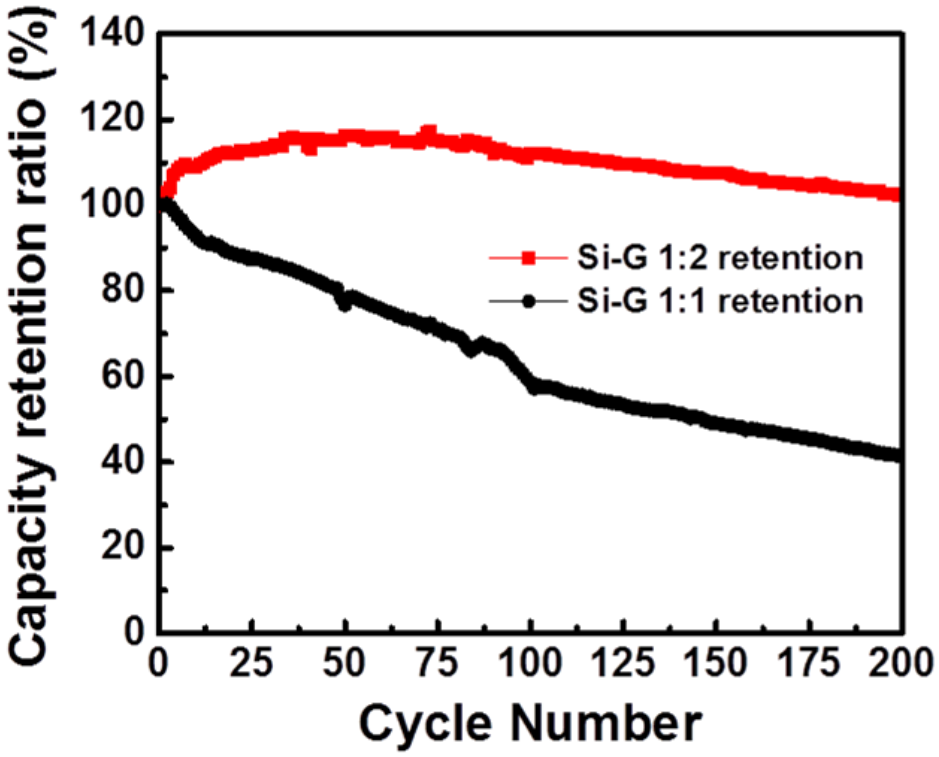


Figure 31: Capacity retention ratio of Si-G 1:2 and Si-G 1:1 at 1 C.

Besides the unique morphology and optimal composition of Si-G composites, the superior cycle stability is also attributed to the remaining $SiO_X$. According to previous researches, a surface layer of $SiO_X$ on Si plays the role of enhancing the stability of Si during cycling.[159,169] The thicker $SiO_X$ layer of Si-G 1:2 due to the higher starting GO content enhances the cycle stability as well, compared to Si-G 1:1. It is worth noting that the previous communication report with Si-G composites demonstrated that their composites only retained around 60% of its initial capacity after 100 cycles at a current density of 200 mA $g^{-1}$ with even a precious additive, vinylene carbonate (VC), in the electrolyte to improve the cycle stability and an HF pre-treatment to

purify the composites.[166] According to our study, the poor cycle stability is attributed to high ratio (~78%) of Si content in the composites which means its amount was not optimal for the composite. In addition, the purification step with HF treatment might have resulted in the inferior cycle stability due to the elimination of the adjuvant SiOx layer for long term stability.

Table 3: Capacity retention data of Si-G 1:2 and Si-G 1:1 in rate capability tests at different current densities.

| **Samples** | **0.2 C** | **0.5 C** | **1.0 C** | **1.5 C** | **2.0 C** | **0.2 C** |
|---|---|---|---|---|---|---|
| Si-G 1:2 | 101.4% | 93.0% | 85.0% | 78.6% | 72.3% | 101.5% |
| Si-G 1:1 | 95.6% | 85.7% | 79.7% | 69.5% | 60.3% | 89.7% |

To further investigate the rate capability of Si-G composites, Si-G 1:2 and Si-G 1:1 were tested at different current densities including 100 mA $g^{-1}$, 0.2 C, 0.5 C, 1 C, 1.5 C and 2 C. As shown in Figure 32 (a), the composite Si-G 1:2 retains most of its capacity at low current densities, such as 100 mA $g^{-1}$ and 0.2 C. With increasing current density the capacity drops a bit, but remains stable, producing 600 mA h $g^{-1}$ @ 2 C (72.3% retention). Returning to 0.2 C, the capacity of Si-G 1:2 remains above 100% retention, minimal degradation is observed from the high rate cycling. As previously determined, Si-G 1:1 gives higher capacity at all current densities applied (Figure 32 (b)), but inferior stability compared to Si-G 1:2. As detailed in Table 3, the capacity retention of Si-G 1:1 is consistently lower than Si-G 1:2 for all rates tested, but even after higher rates were applied it still retained 89.7% capacity.

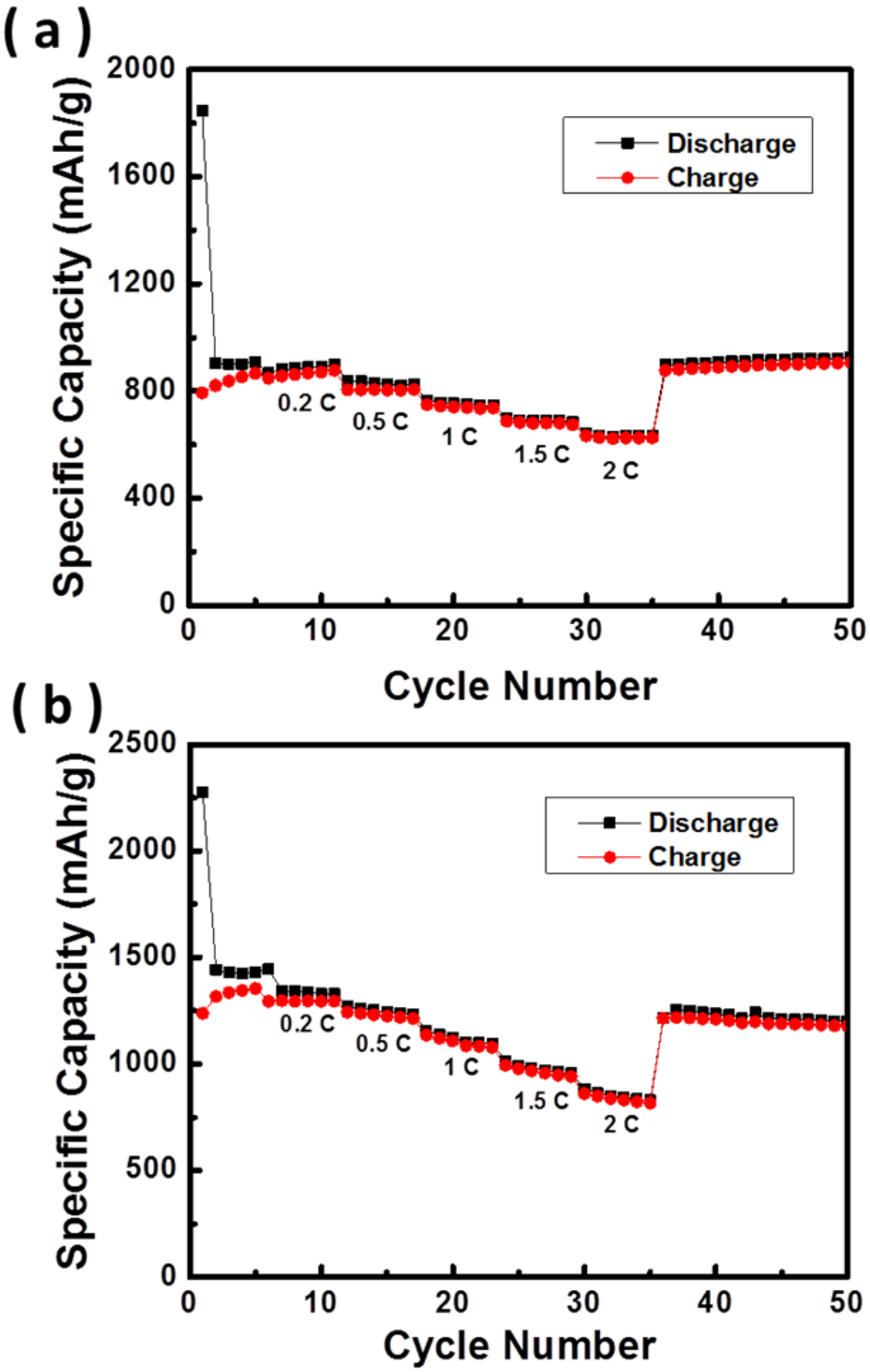


Figure 32: Rate capability data of Si-G 1:2 (a) and Si-G 1:1 (b).

Cycle stability and rate capability both confirmed that Si-G 1:2 ratio outperforms the other composites and determined the optimum ratio to maximize the long-term battery performance. Therefore, CV was conducted on the batteries composed from the Si-G 1:2 composite to more closely investigate electrochemical reactions during discharge and charge (Figure 33). The CV test was performed on a freshly-prepared cell with a scan rate of 0.1 mV $s^{-1}$ and a voltage range of 0.05-1.5 V. In the first cathodic scan (lithiation), the current begins to increase sharply at 0.8 V, followed by a current plateau from around 0.7 V to around 0.2 V. This is due to the decomposition of electrolyte and the formation of SEI.[182,183] In addition, the irreversible first cycle capacity of graphene also helps to explain the long plateau. The remaining peak extending from 0.2 V to the low cut-off voltage is characteristic to the lithiation of Si. Meanwhile, the first anodic scan (delithiation) develops a weak current plateau from 0.2V to 0.5V. In future cycles, the CV curve reveals the development of a 0.2 V peak in the cathodic scan and two peaks at 0.3 V and 0.5 V within the anodic scan, characteristic to the formation of amorphous silicon.[166,181] The area circumscribed by the anodic curves in each full cycle keeps increasing in the first five cycles and after accounting for the initial irreversible discharge capacity the area of the cathodic scan increases for each of the future cycles. This further suggests that more silicon is activated as the stress for lithiation and delithiation decreases in future cycles.

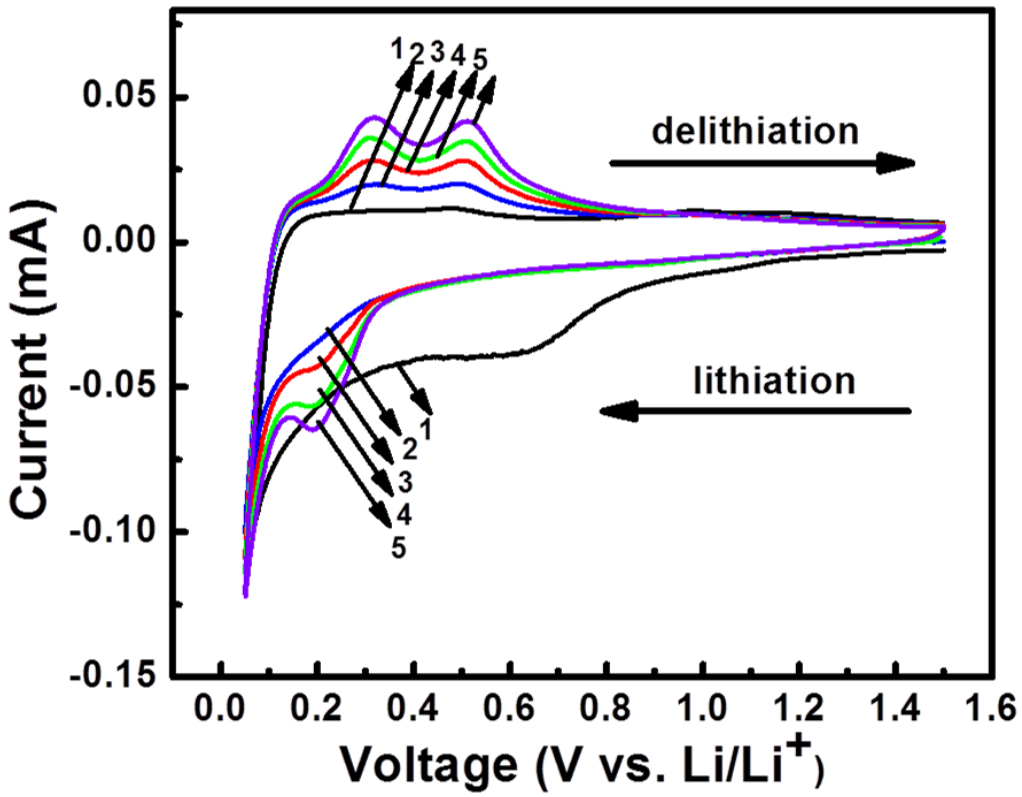


Figure 33: Cyclic voltammetry curves of Si-G 1:2 composite of first five cycles at a scan rate of 0.1 mV s-1 in the voltage range of 0.05-1.5 V.

### 3.4 Conclusions and remarks

In summary, graphene wrapped silicon composites were fabricated by a facile freeze-drying method and a subsequent annealing treatment. Different ratios of Si and GO were used to obtain a variety of Si-Gs, which were further characterized and investigated by both structural and electrochemical tests. When appropriate Si and GO ratios were utilized, such as 1:1 and 1:2, the Si-NPs were well wrapped by graphene. The wrapped Si-G composites not only utilize the high capacity of Si, but also harness graphene's conductivity and flexibility to contribute conductivity to the electrode and accommodate the volume change of Si. The first of two composites showing promising electrochemical performance, Si-G 1:1 showed a high reversible capacity of 1200 mA

h $g^{-1}$, much higher than graphene and with much better stability than the regular Si-NP electrode. The more optimal composite Si-G 1:2 achieved superior stability, its capacity continuing to increase for the first 50 cycles. After 200 cycles, Si-G 1:2 retained a specific capacity of 786.3 mA h $g^{-1}$, similar to its initial capacity. This performance was achieved with no tedious or extreme treatments and without the presence of electrolyte additives, making it possible for mass production in commercial applications. Both the facile synthesis of the material and superior performance make Si-G composite a promising anode material for next-generation lithium ion batteries.

Extended efforts have been made for this project. Carbon coating by a chemical-vapor-deposition (CVD) method was used to build a carbon layer within the space of the silicon and graphene composite. With this method, the pathways for the electron transport from graphene to silicon nano particles as well the contact between active material and current collector was better accommodated. Low temperature reduction of graphene in the above Si-G project also continues to draw attention from both industrial and academic fields. Here the Si-GO composite was first fabricated and then made into electrodes, followed by low temperature reduction of GO at 150 degrees Celsius. GO in the Si-GO composites was examined by Raman spectroscopy and FTIR to study the effect of low temperature reduction. The result showed the Go was well reduced and implied qualities of graphene. From both the material characterization and battery performance it can be concluded that graphene oxide is effectively reduced to graphene, offering significantly improved performance for silicon regarding both capacity and stability.

## 4.0 $Co_3O_4$ grown on stainless steel mesh for LIB's anode material

### 4.1 Introduction and purpose of study

Compared to the conventional graphite (372 mAh $g^{-1}$) used in lithium ion batteries, transition metal oxides such as $TiO_2$,[110] $Co_3O_4$, [111] $Mn_3O_4$,[112] $Fe_3O_4$[113] and CoO[114] show as high as twice or three times the capacity. Unfortunately, similar to that of materials mentioned above, practical usage of transitional metal oxides in LIBs is also hindered by their large irreversible capacity at 1st discharge and large volume change with severe particle aggregation during charge and discharge, which leads to poor rate performance and cycle capabilities caused by electrode degradation by loss of contact points between the active material and the current collector.[140,141]

Poizot *et al.* proved for the first time that transitional metal oxides can store lithium via a heterogeneous conversion reaction mechanism:[47]

$$MxOy + 2y\ Li \rightarrow y\ Li_2O + x\ M \qquad (5)$$

In this generalized reaction equation, M stands for any applicable metal, and x and y represent integers in the most simplified reaction formula. This reaction was not expected to happen due to the very inert reactivity of $Li_2O$ with transitional metal oxides at room temperature.[109] It was later clarified that the strengthened electrochemical reactivity of $Li_2O$ is owing to the nanostructure of the metal oxides. In these nanostructures, $Li_2O$ and transitional metals can form ultra-tiny grains and they can interphase homogeneously.[134]

$Co_3O_4$ has been known with high lithium electroactivity as anode material in LIBs for many years and different methods have been tried to obtain various kinds of $Co_3O_4$ nanomaterial.[135] $Co_3O_4$ nanoparticle, nanotube, nanowire, cage, and $Co_3O_4$-carbon composite have all been reported to find applications in LIBs because the theoretical capacity of $Co_3O_4$ is as high as

890mAh $g^{-1}$; more than twice the value of graphite (<372mAh $g^{-1}$) ,which is widely used in commercial LIBs. LIBs with $Co_3O_4$ as their anode materials are found to store and release energy via a process of intercalation and deintercalation of lithium ions, which can also be interpreted as formation or decomposition of $Li_2O$.[184] However, common powder-type materials need a conventional electrode fabrication process with a binder and carbon material which will decrease the specific energy density of batteries; besides, the long term cycle stability and rate capability require further improvement.

Directly grown $Co_3O_4$ nano-materials on current collectors with several strategies have also been proposed for LIBs. For example, Fu *et al*. introduced lemongrass-like morphology of $Co_3O_4$ on Ni foam with a remarkable performance. However, compared to stainless steel mesh, Nickel foam is thicker, thus occupying more space in the battery and lowering the volumetric energy density in practical application. Besides, the mechanic strength of the Nickel foam is weaker than that of stainless steel. Li *et al.* introduced the directly grown $Co_3O_4$ nanotubes on alumina membranes for LIBs and gas sensors.[185] Compared to the alumina membrane, stainless steel has a superior flexibility. Stainless steel has also been adopted as a current collector and substrate by some researchers with attractive performances, e.g. Chan *et al.* developed Si NW on stainless steel substrate with a high performance.[106] Boyano, I *et al.* successfully deposited C-$LiFePO_4$\polypyrrole on stainless steel mesh for cathode in LIB.[186] Thus, we proposed the method of directly growing active material on the current collector to enhance the conductivity between the current collector and active material. Here, the SS mesh acts as both a current collector and a substrate. This method is not only easier but also more economically acceptable than other methods using extra substrate, additional conductive materials, and a binder, all of which[106] make the battery fabrication process very time consuming and expensive. Also,

conventional battery fabrication methods as mentioned are confronted with the problem of less tight contact between the active material and the substrate, which may add difficulties in battery fabrication and increase internal resistance of batteries.[138] Furthermore, the $Co_3O_4$ NW can be grown on both sides of the mesh at the same time to eliminate a complicated double side coating process. In addition, stainless steel has a good mechanical strength as well as a reliable electrochemical stability in LIBs. As shown in Figure 34 (A), SS mesh has a great flexibility; $Co_3O_4$ NW on SS mesh was not peeled off by considerable curling (Figure 34 (B)), which makes it promising for application in flexible batteries.[187,188]

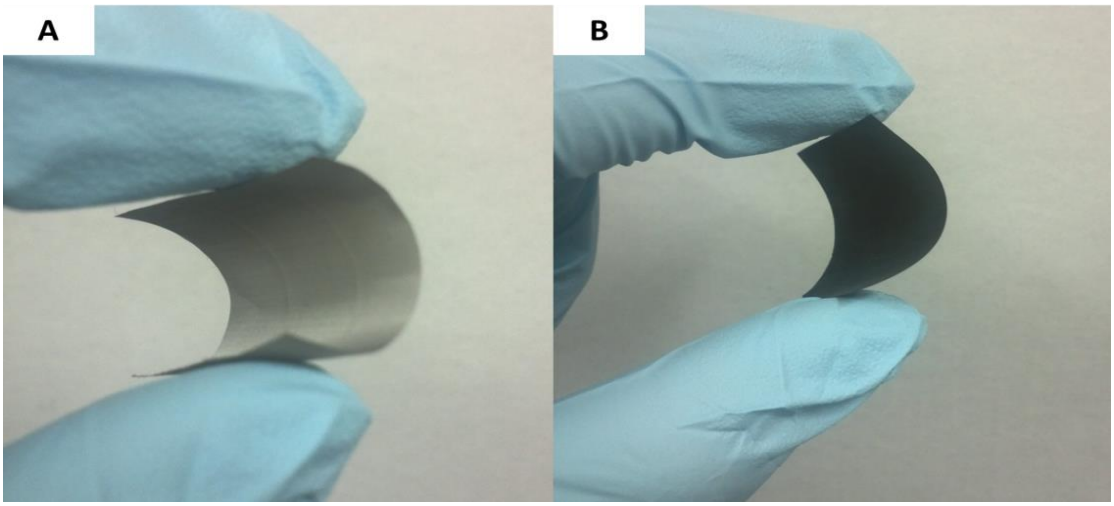


Figure 34: Photographs of stainless steel mesh before (A) and after (B) the growth of $Co_3O_4$ nanowire.

The porous electrode structure and nanostructured active material shown in Figure 34 (B) are believed to give huge surface area, large free volume, along with increased lithium-ion diffusion rate,[189-192] endowing the LIBs made from it with superior performance during charge and discharge process. The performance of batteries made with $Co_3O_4$ on SS mesh was highly

satisfactory with a stable capacity of around 800mAh $g^{-1}$after 100 cycles with a current density of 200mA $g^{-1}$.

### 4.2 Experimental methods

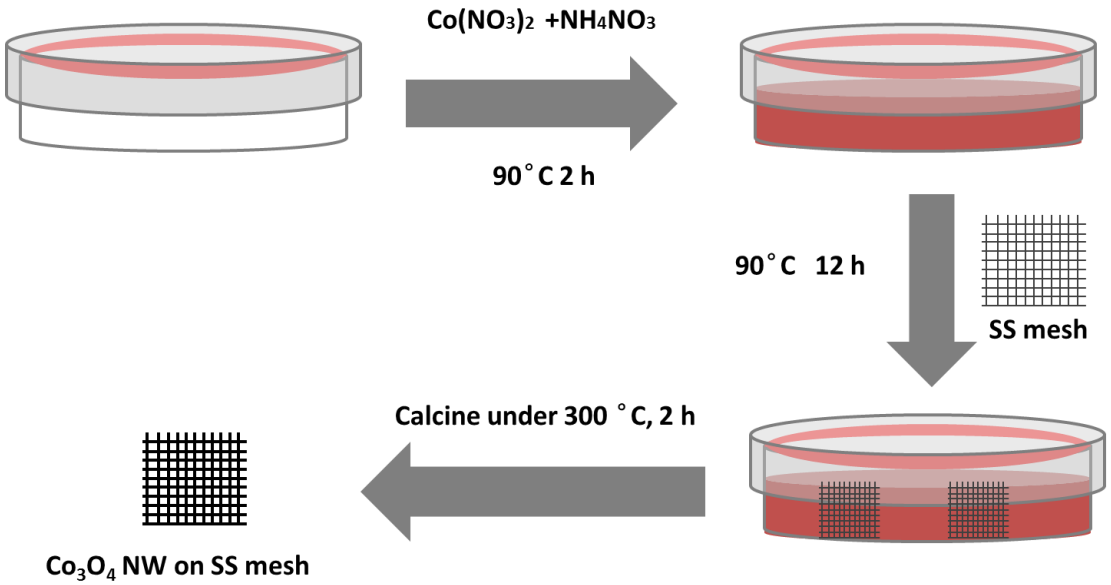


Figure 35: A schematic view of the synthesis of the $Co_3O_4$ NW on the SS mesh.

Stainless steel (SS) mesh-supported $Co_3O_4$ NW electrodes were synthesized via a template-free growth method as described in Figure 35. Cobalt Nitrate(10mmol, $Co(NO_3)_2 \cdot 6H_2O$, Sigma-Aldrich) and Ammonia Nitrate(5mmol, $NH_4NO_3$, Sigma-Aldrich) were dissolved in an ammonia solution consisting of 35 ml water(de-ionized, same below) and 15 ml ammonia (30wt%).Then, it was slowly mixed by a magnetic stirrer for 10 min in air at room temperature. After that, the solution was transferred to a Petri dish wrapped with Teflon tape. The following perheating step was conducted by placing the covered Petri dish in the 90 $^oC$ oven for 2 h. Meanwhile, the 500-

mesh SS (3 cm × 3 cm) was sonicated in water and acetone for 15 min respectively to remove inorganic salts and organic impurities on the mesh. Then the SS mesh was soaked in 6.0 M HCl for 15 min and rinsed with water thoroughly to get rid of metal oxides. After the solution was preheated for 2 h, the SS mesh was immersed in it and kept for 12 h at the same temperature. After the reaction, the SS mesh was rinsed with de-ionized water and dried in an oven at 60 $^{o}$C, followed by calcination under 300 $^{o}$C for 2 h in air with a ramping rate of 2 $^{o}$C per minute. The structure and phase composition of the samples obtained was examined by X-ray diffraction (XRD). Then scanning electron microscopy (SEM) and transmission electron microscopy (TEM) were adapted to investigate the morphology of the sample. To evaluate the performances, CR-2032 coin cells were fabricated with lithium metal foil as both the reference and counter electrode, and 1 M $LiPF_6$ in a mixed solution of ethylene carbonate (EC) and diethyl carbonate (DEC) (1:1 volume ratio, Novolyte, USA) was used as the electrolyte. The conventional $Co_3O_4$ NW electrode consisted of $Co_3O_4$ NW collected from the SS mesh-supported $Co_3O_4$ NW electrode, carbon black as a conductive material, PVDF as a binder, and copper (Cu) foil as a current collector.

### 4.3 Results and discussion

The color of the SS mesh turned black from the original silver gray color (Figure 34 A) after the reaction in the Petri dish. The black material attached to the mesh tightly even after vigorous rinse with water and ethanol. The sample was calcined under 300 $^{o}$C after drying in air. The black material on the mesh didn't peel off after the calcination (Figure 34 B).

Figure 36 A shows the XRD pattern of the SS mesh electrode with the diffraction peaks observed at 18.95 °, 31.29 °, 36.8 °, 44.9 °, 59.39 ° and 65.25 °, which are indexed to (111), (220), (311),

(440), (511) and (440) planes of crystalline $Co_3O_4$, in accordance with the standard JCPDS Card NO. 42-1467.[193] No other obvious peaks exist, indicating the absence of any impurities.

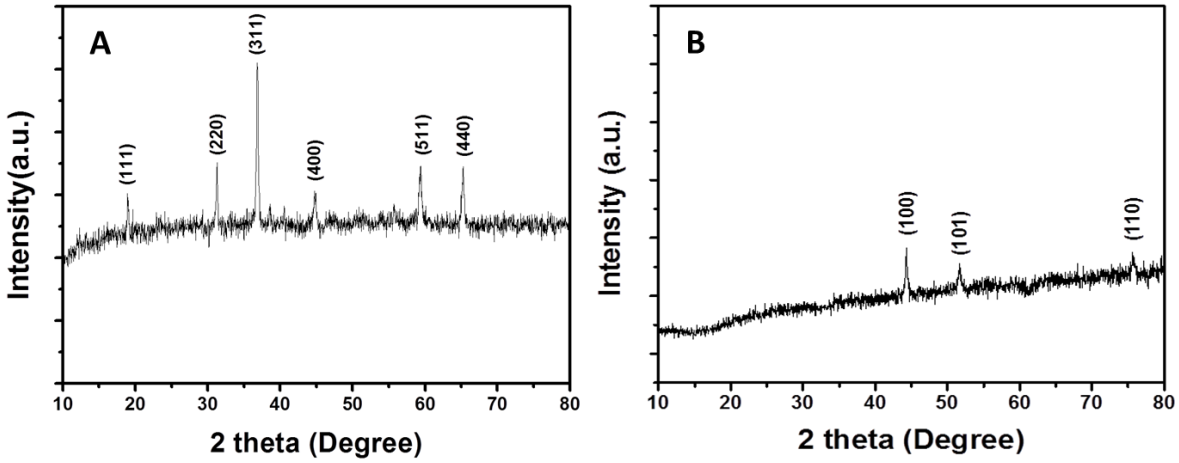


Figure 36: XRD patterns of $Co_3O_4$ NW on SS mesh before (A) and after (B) cycling.

The morphology of the synthesized material on the SS mesh was clearly shown by SEM that $Co_3O_4$ NW grew on the SS mesh substrate densely and vertically, making the bare SS wires barely visible (Figure 37 A). However, it revealed that the NWs did not block the net skeletons of the SS mesh, thus improving the electrolyte diffusion and reaction kinetics between the $Co_3O_4$ NW materials and the electrolyte on both sides. Figure 37 B indicates that the diameters of NWs are around 300 nm and some NWs are interconnected during the synthesis. Figure 37 C shows a typical TEM image of several $Co_3O_4$ NWs peeled off from the SS mesh with dimensions consistent with SEM results. In addition, surface roughness can be clearly observed, resulting in increased surface area between the electrode and electrolyte. The high crystallinity of $Co_3O_4$ NWs is revealed by the SAED pattern inset in Figure 37 C. The fringes observed in high-

resolution TEM image in Figure 37 D also confirms crystalline $Co_3O_4$ NW with the lattice distance of 0.233 nm measured corresponding to (222) plane.

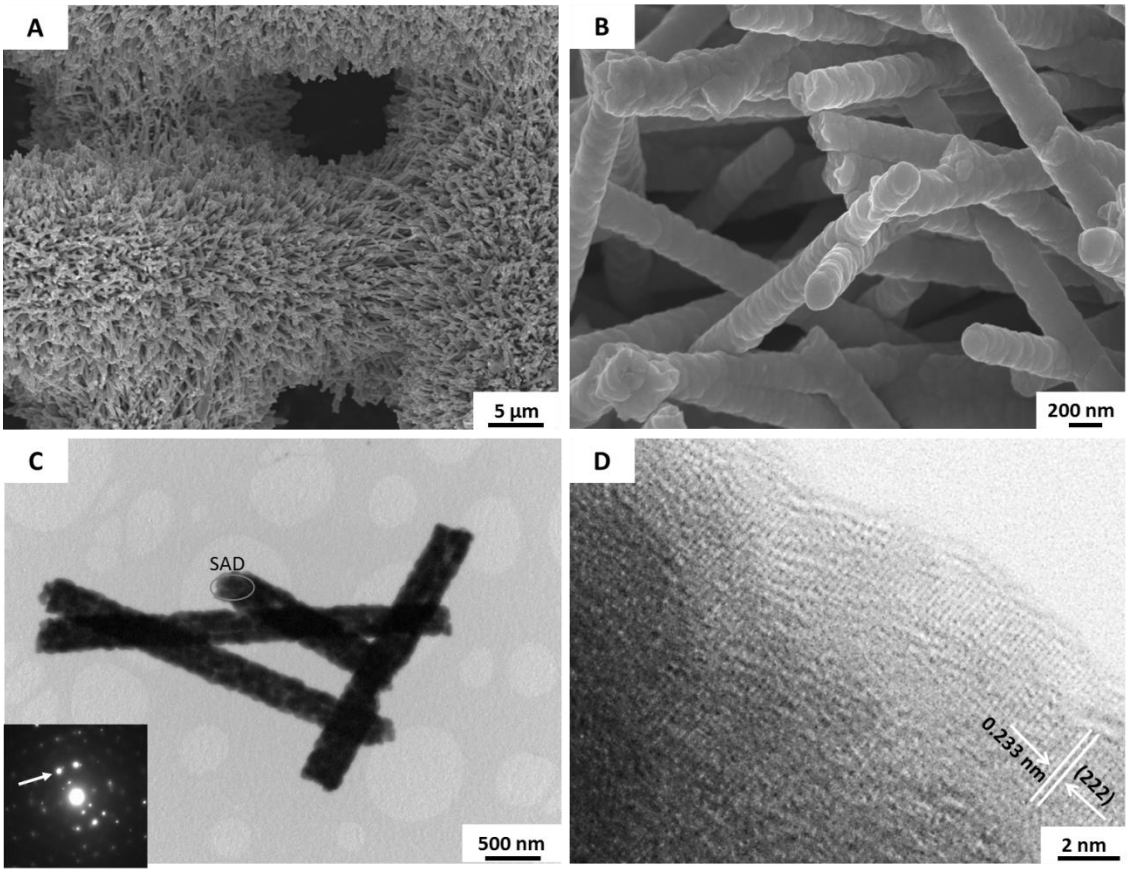


Figure 37: SEM images of $Co_3O_4$ NWs on SS mesh at low magnification (A) and high magnification (B), TEM image of the $Co_3O_4$ NWs on SS mesh (C) (Inset is SAED pattern) and the corresponding HRTEM image (D).

To investigate the electrochemical process during charge and discharge of $Co_3O_4$ NW on SS mesh, cyclic voltammetry (CV) of the prepared electrode was conducted at a scan rate of 1mV $s^{-1}$ from 0.01V to 3V (Figure 38). The cathodic peak was observed at 0.52 V in the first cycle, corresponding to the first electochemical reduction reaciton of $Co_3O_4$ and the formation of solid electrolyte interface (SEI). P. Poizot *et al* have suggested that the formation and decomposition

of $Li_2O$ takes place in the electrochemical reaction between transitional metal oxides, such as CoO and Li in LIBs.[47] The single reduction peak at 0.52V, which is different from the previous result, can be attributed to the incomplete decomposition of $Co_3O_4$ in the first discharge reaction.[137] The first anodic peak was observed at 2.11V, corresponding to the oxidation of $Co^0$ to $Co^{3+}$. The electrochemical reaction mechanism of $Co_3O_4$ and Li can be interpreted as follows:

$$8Li \leftrightarrow 8Li^+ + 8e^- \quad (6)$$

$$Co_3O_4 + 8Li^+ + 8e^- \leftrightarrow 4Li_2O + 3Co \quad (7)$$

$$Co_3O_4 + 8Li \Leftrightarrow 4Li_2O + 3Co \quad (8)$$

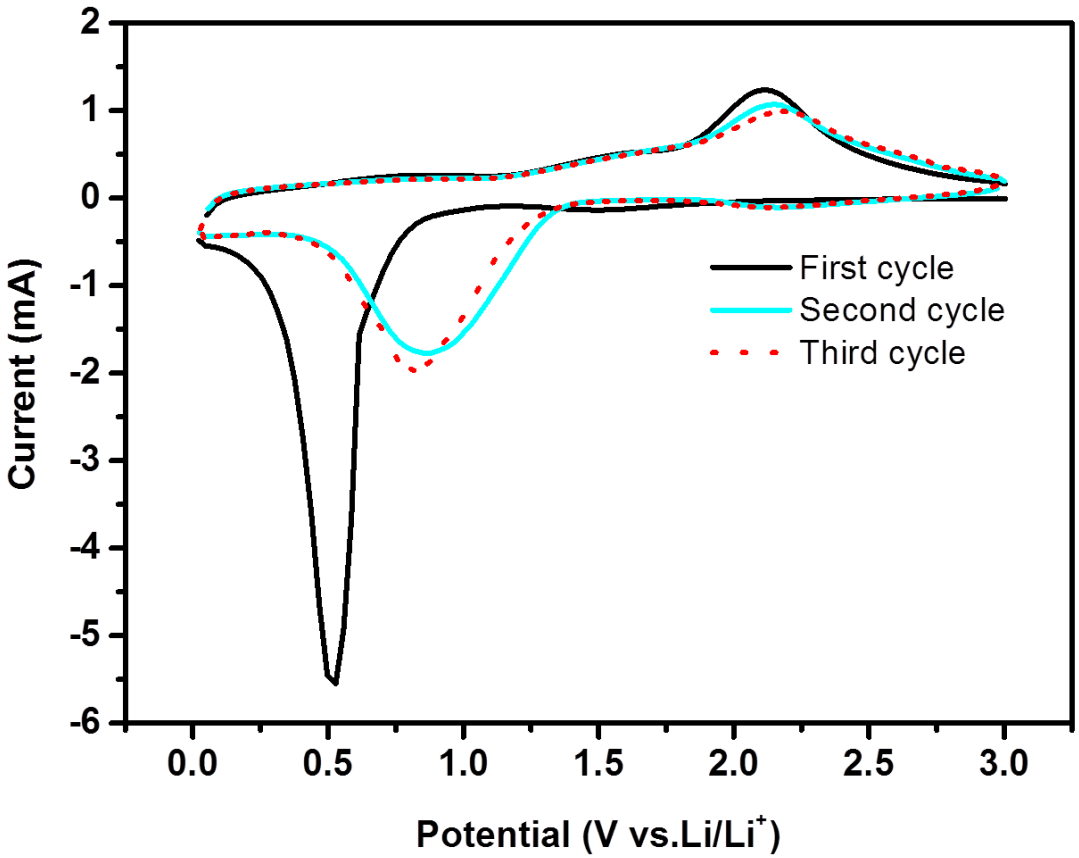

Figure 38. CV curves of $Co_3O_4$ NW on SS mesh. Scan rate 1mV $s^{-1}$, potential range 0.01-3 V.

As shown in Figure 39 A, the cycle stability and rate capability of SS mesh-supported $Co_3O_4$ NW electrode and conventional $Co_3O_4$ NW electrode were investigated by the galvanostatic discharge and charge measurement with various applied currents. The specific discharge and charge capacities in the first cycle of SS mesh-supported $Co_3O_4$ NW electrode were 1106.9 mAh $g^{-1}$ and 855.1 mAh $g^{-1}$ at a current density of 100 mA $g^{-1}$, with a coulometric efficiency of 77.3%. The specific discharge capacity in the second cycle was 883.4 mAh $g^{-1}$ with capacity retention of 79.8% in respect of first two cycles. The specific capacities of conventional $Co_3O_4$ electrode in first discharge and charge were 1129 mAh $g^{-1}$ and 782 mAh $g^{-1}$, and the coulometric efficiency was 69.3%, 8 percentage points lower than that of $Co_3O_4$ NW on SS mesh. The specific discharge capacity in the second cycle was 801 mAh $g^{-1}$ and the capacity retention was 70.9%, which was 9 percentage points lower than that of $Co_3O_4$ NW on SS mesh.

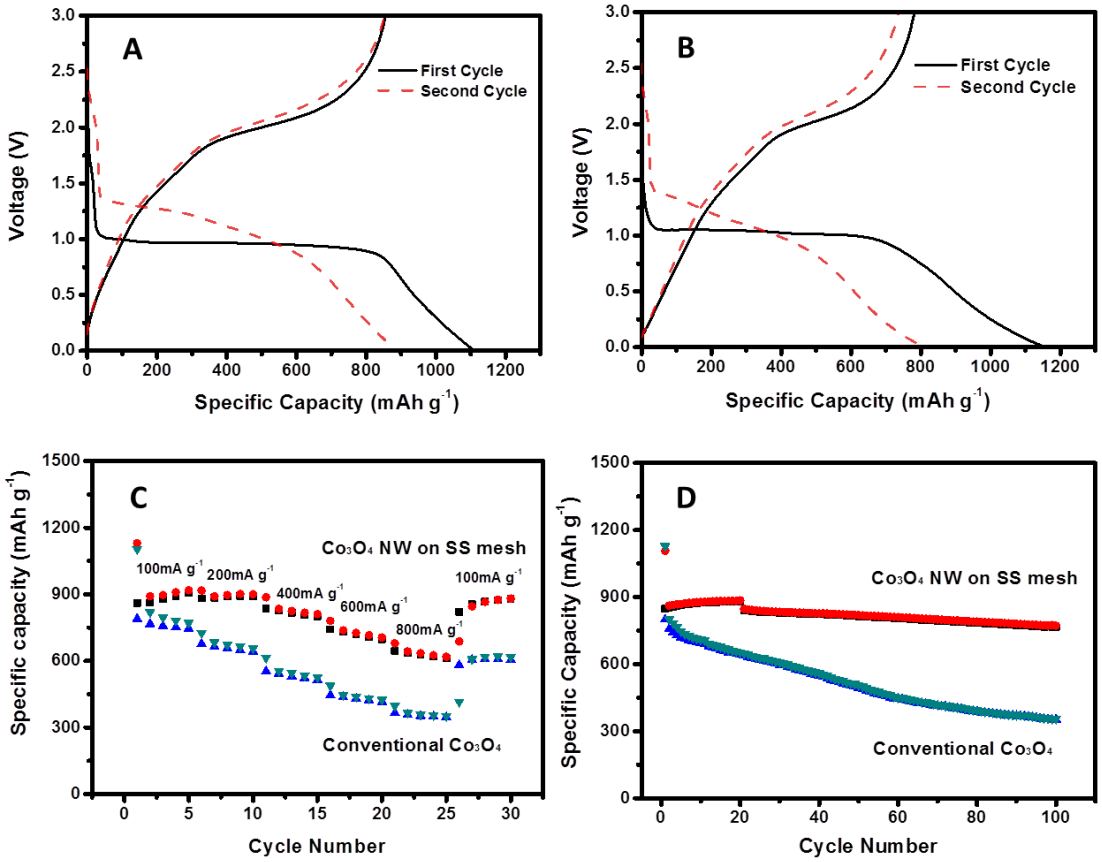


Figure 39: Galvanostatic charge and discharge curves of the $Co_3O_4$ NW on SS mesh (A) and the conventional $Co_3O_4$ NW electrode (B). $Co_3O_4$ NW on SS mesh and the conventional $Co_3O_4$ NW electrode at various current rates from 100 to 800 mA $g^{-1}$ with respect to the cycle number (C) and cyclic performances of batteries made from $Co_3O_4$ NW on SS mesh and conventional $Co_3O_4$ (D).

The large irreversible capacity during first cycle is attributed to the irreversible conversion reaction of the $Co_3O_4$ NW by Li ions and the formation of a solid electrolyte interface (SEI) layer by electrolyte decomposition. During the second cycle, the difference of the discharge and charge capacity was reduced, suggesting that most of irreversible reactions including the formation of an SEI layer occurred during the first cycle. Figure 39 C demonstrates the cycle stability of SS mesh-supported $Co_3O_4$ NW electrode with various current densities. The charge

capacity achieved 645 mAh $g^{-1}$ at a current rate of 800 mA $g^{-1}$, which was significantly better than that of conventional $Co_3O_4$ NW electrode (366 mAh $g^{-1}$). Furthermore, after 30 cycles with various current densities, the mesh-supported $Co_3O_4$ NW electrode was stabilized at around 880 mAh $g^{-1}$, introducing the superior cycle stability of the electrode. The recoverable capacity in subsequent cycles also well implies the structure integrity of the $Co_3O_4$ NW on the electrode. In Figure 39 D, $Co_3O_4$ NW on SS mesh was first tested at a current density of 100 mA $g^{-1}$. In first 20 cycles, the capacity increased gradually by around 30 mAh $g^{-1}$ from ~850 to ~880 mAh $g^{-1}$. After that, the current density was altered to 200 mA $g^{-1}$. The battery had an initial capacity of around 841.3 mAh $g^{-1}$ under 200mA $g^{-1}$. After 100 cycles in total, there was still a capacity of 765.8mAh $g^{-1}$, which was about 90% the capacity of the initial value. The battery with conventional $Co_3O_4$ was tested at 100mA $g^{-1}$, but the cyclic performance was far worse than the $Co_3O_4$ NW on SS mesh, indicating that the battery with $Co_3O_4$ NW on SS mesh was superior due to the three-dimensional structure of the electrode.

As mentioned in introduction part, electrode materials being directly synthesized on current collector has been reported. To be convenient, a battery's capacity is usually presented based on electrode's area. The areal capacity of $Co_3O_4$ on SS mesh after 100 cycles was calculated to be 0.675 mAh $cm^{-2}$ at a charge/discharge rate of 0.173 mA $cm^{-2}$. The above capacity is very competitive, namely, two to three times that of the reported values in the peer-reviewed articles published recent years.[45,46]

It is assumed that the excellent cycle stability and rate capability are attributed to its unique morphology in which the $Co_3O_4$ NW is directly connected to the current collector and its porous structure of the electrode. These structures of the electrode are expected to reduce resistance of the electrode and improve the performance of Li ion batteries, and the idea was confirmed by

electrochemical impedance spectroscopy (EIS) measurement compared with the conventional $Co_3O_4$ NW electrode at fully discharged states (Figure 40). The results of EIS revealed that charge transfer resistance of the mesh-supported $Co_3O_4$ NW electrode was around 40 ohm lower than that of conventional $Co_3O_4$ NW electrode. These results correspond to the rate capability test in Figure 39 C. Furthermore, it is confirmed that the electrochemical reactions in the directly grown $Co_3O_4$ NW on mesh are faster, suggesting that the faster electron conduction between the current collector and the active materials plays a critical role in the overall battery performance.

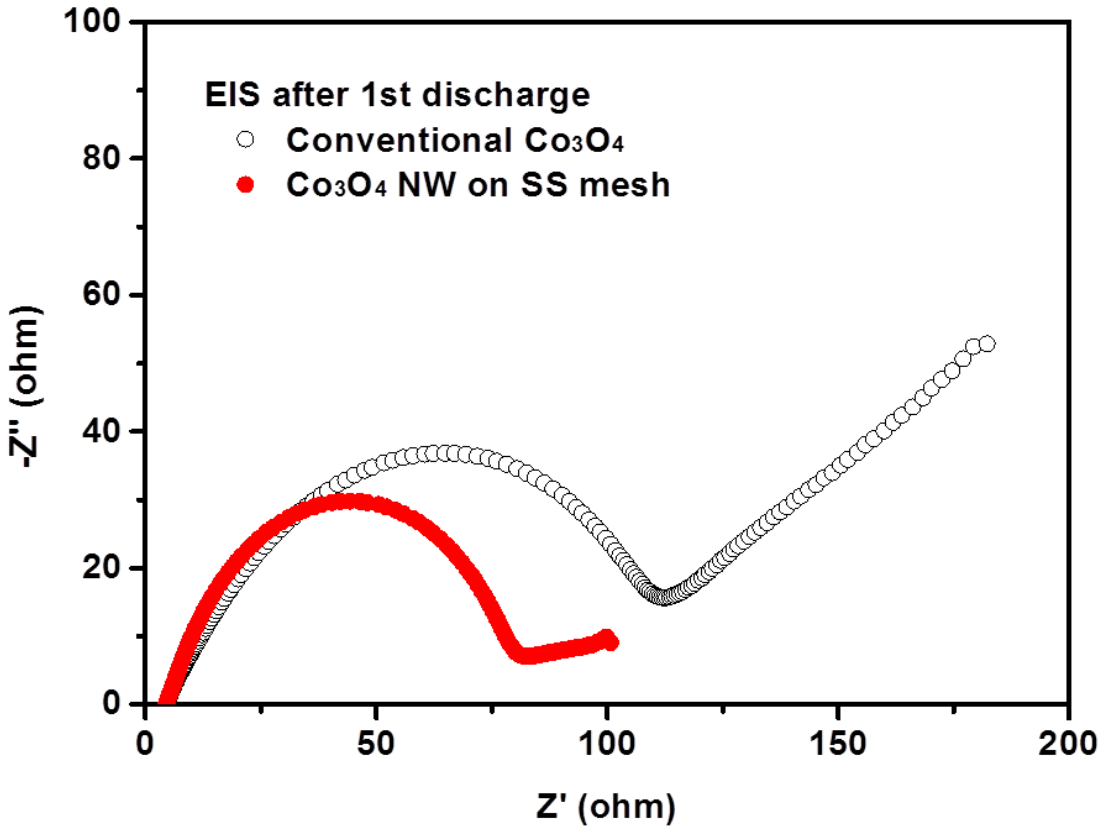


Figure 40: EIS results of the $Co_3O_4$ nanowires on SS mesh and conventional $Co_3O_4$ NW electrode at fully discharged states.

Figure 41 shows the pictures of $Co_3O_4$ NW on SS mesh after 100 cycles. A coin cell was dissembled at fully-charged state to obtain the cycled electrode, which was subsequently washed with dimethyl carbonate (DMC) to remove any residue electrolyte or organic by-product from electrode reaction. The cycled electrode was bent by fingers (Figure 41 A) and tweezers (Figure 41 B). No active material peeled off from the significant deformation. This proves that $Co_3O_4$ NW is firmly attached to SS mesh even after the electrochemical process.

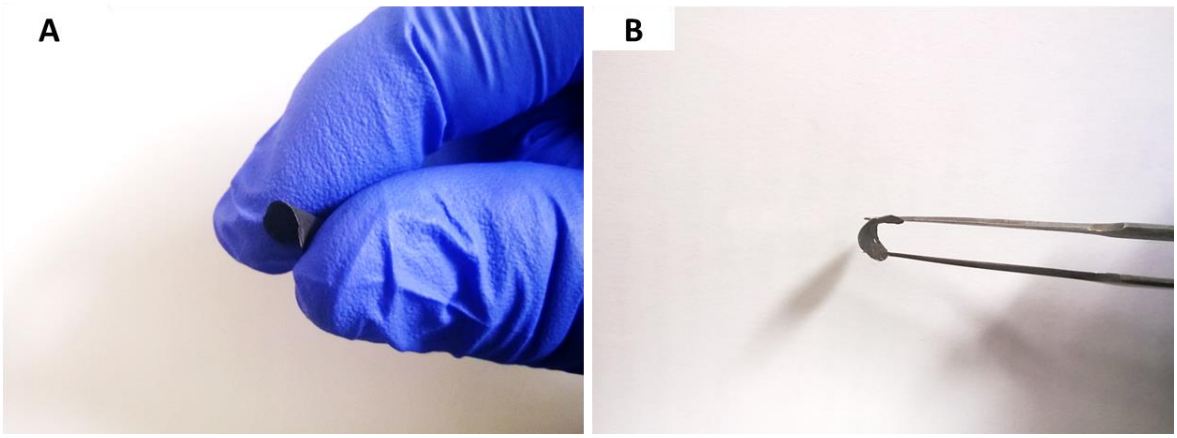


Figure 41 Photographs of $Co_3O_4$ NW on SS mesh after cycling, (A) bended with fingers, (B) bended with tweezers.

XRD and SEM were adopted to study the morphology and composition of the electrode. XRD was first conducted to confirm the composition of the used electrode. As shown in Figure 36 B, only stainless steel's characteristic peaks are found in the pattern, which proves that $Co_3O_4$ did not return to its original spinel crystalline form after cycling. This result is consistent with several previous reports about the chemical reactivity of $Co_3O_4$.[138,188,194] However, despite the structure transformation, the $Co_3O_4$ NW maintained its structure integrity after long-term cycling as shown in the following SEM images. Figure 42 A shows the $Co_3O_4$ NW on SS mesh from a large scale. It is easy to see that the 3-D network structure of the original electrode is well

maintained after cycling; $Co_3O_4$ NWs are firmly attached to the mesh without being peeled off by the repeated lithiation/delithition processes. Compared to Figure 37 A, the pores on the mesh do not vanish, although the size of these pores diminishes after cycling, thus these pores can continue contributing to offer a better pathway for $Li^+$ diffusion in the electrolyte than traditional copper foil electrode. Figure 42 B is a zoomed-in image of the same mesh. The average diameter of $Co_3O_4$ NWs is around 300 nm, which is approximately 100 nm greater than its original value. This volume expansion can be an effect of lithiation during the discharge process of the half cell.

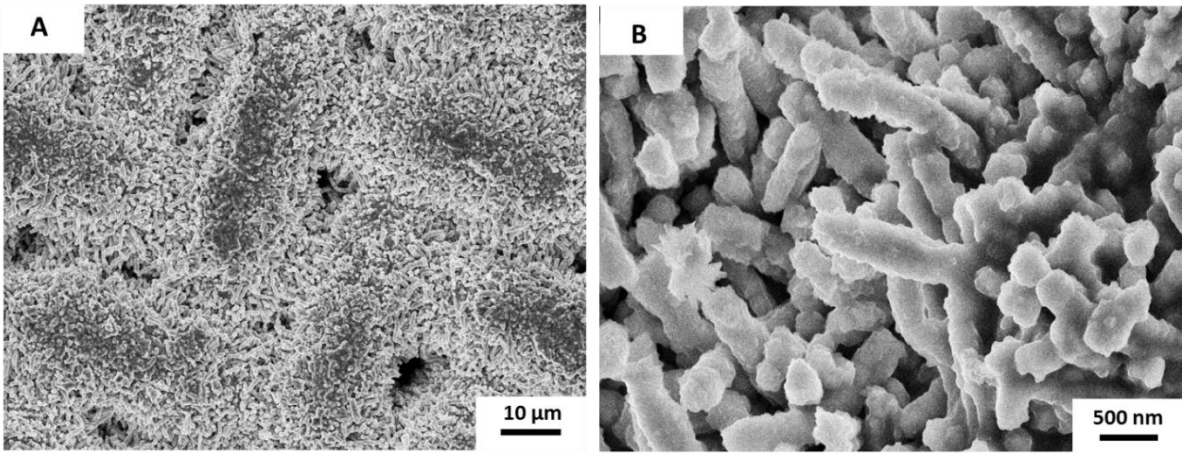


Figure 42 SEM images of $Co_3O_4$ NW on SS mesh after cycling.

### 4.4 Conclusions and remarks

In conclusion, a facile way was introduced to synthesize $Co_3O_4$ NW on stainless steel mesh substrate directly with a novel morphology and an excellent electrochemical performance in LIBs. The directly-grown $Co_3O_4$ NW on SS mesh was prepared via an ammonia-evaporation-induced method followed by calcination under 300 ℃ in air. Free from the tedious and

economically unfavorable electrode fabrication, $Co_3O_4$ NW on SS mesh simplified the process by a direct grow technique. Furthermore, it better addresses the capacity as well as the durability issue of $Co_3O_4$. Together with its superior mechanical strength and flexibility, this novel $Co_3O_4$ may find many applications in different types of LIBs. The crystal structure of as-obtained $Co_3O_4$ was identified by X-ray diffraction. The morphology of prepared $Co_3O_4$ NW on SS mesh was characterized by SEM and TEM. SEM images showed a SS mesh-sketched structure with densely grown nanowires and ordered meshes on it. The charge and discharge capabilities were stabilized at around 880mAh $g^{-1}$ after 30 cycles with various current densities. Electrochemical impedance spectroscopy (EIS) confirmed that the charge transfer resistance of the mesh-supported $Co_3O_4$ NW electrode was prominently lower than that of conventional $Co_3O_4$ NW electrode.

It was confirmed that $Co_3O_4$ NW was directly and vertically formed on the SS-mesh substrate with the original net structure of the mesh. We suggest that the unique morphology of the material and the structure of the electrode should be responsible for the superior performance for the LIB with the low charge transfer resistance. Consequently, the $Co_3O_4$ NW on the SS-mesh anode exhibited 855.1 mAh $g^{-1}$ of initial capacity at 100 mA $g^{-1}$ of the current density, which corresponds to the theoretical capacity of $Co_3O_4$. Furthermore, it presents a capacity of 655 mAh $g^{-1}$ at 800 mA $g^{-1}$ of the current density which is 300 mAh $g^{-1}$ higher than the capacity of conventionally prepared electrode of $Co_3O_4$ NW. After 30 cycles of the rate capability test, the electrode revealed superior cycle stability with 880 mAh $g^{-1}$ at the current density of 100 mA $g^{-1}$, which is a little higher than the initial capacity. All these results suggest that the SS-mesh supported $Co_3O_4$ nanowire anode should be a promising electrode for Li ion batteries.

## 5.0 Summary and future direction

As a key component in a LIB, an anode plays a vital role in determining the overall performance of a battery. Thus, it is an essential task to develop novel anode materials with enhanced performance to meet high-energy and high-power demands of next generation LIBs. Herein, successful efforts have been made to obtain Si-G composites and electrodes with $Co_3O_4$ NW directly grown on the SS mesh. Graphene wrapped silicon nanoparticles not only provide better electric conductivity of the active material, but also help protect silicon from irreversible structural destruction. A stable SEI layer is formed on the surface of the Si-G composite upon cycling, contributing to the evident reduction of side reactions in following cycles. $Co_3O_4$ NW on the SS mesh as an electrode material in LIBs has an advantage over traditional electrode materials in terms of both electrode fabrication and electrochemical performance. The preparation $Co_3O_4$ NW on the SS mesh eliminates the time-consuming and expensive electrode-casting process by directly growing active material on the substrate. By abandoning binder materials and conductive additives, the $Co_3O_4$ NW improves the utility of overall electrode mass. The directly grown $Co_3O_4$ NW on SS mesh possesses merits that can improve its performance in LIBs. Direct growth of $Co_3O_4$ NW on SS mesh presents a better contact between the active material and the substrate, and thus enhances the electric conductivity in between. The nano porous structure of the material also provides sufficient pathways for lithium ion diffusion. The internal resistance of batteries can be lessened due to these virtues.

Promising results have been presented with both silicon and cobalt materials. To obtain more competitive anode materials, continuous work should be devoted to relevant research. For example, the synthesis process of the Si-G composite can be simplified by using low temperature reduction instead of the high-temperature pyrolysis adopted in this research. Silicon has a

theoretical capacity of 4200 mA $g^{-1}$, but only 800 mAh $g^{-1}$ is achieved in this research, leaving much room for improvement. Except for $Co_3O_4$, other transitional metal oxides such manganese oxides, iron oxides present attractive performance in LIBs, while offers easy synthesis and low cost, and research in these areas bears tremendous significance.

# References


1 Arico, A. S., Bruce, P., Scrosati, B., Tarascon, J. M. & van Schalkwijk, W. Nanostructured materials for advanced energy conversion and storage devices. *Nat Mater* **4**, 366-377, doi:10.1038/nmat1368 (2005).

2 Tarascon, J. M. & Armand, M. Issues and challenges facing rechargeable lithium batteries. *Nature* **414**, 359-367, doi:Doi 10.1038/35104644 (2001).

3 Whittingham, M. S. Electrical energy storage and intercalation chemistry. *Science* **192**, 1126-1127, doi:10.1126/science.192.4244.1126 (1976).

4 Steele, B. C. H. Chemical Diffusion. *Nato Adv Sci Inst Se* (1973).

5 Rao, B. M. L., Francis, R. W. & Christopher, H. A. Lithium-Aluminum Electrode. *J Electrochem Soc* **124**, 1490-1492, doi:Doi 10.1149/1.2133098 (1977).

6 Geronov, Y., Zlatilova, P. & Staikov, G. The Secondary Lithium Aluminum Electrode at Room-Temperature .2. Kinetics of the Electrochemical Formation of the Lithium Aluminum-Alloy. *Journal of Power Sources* **12**, 155-165, doi:Doi 10.1016/0378-7753(84)80046-4 (1984).

7 Peled, E., Menachem, C., BarTow, D. & Melman, A. Improved graphite anode for lithium-ion batteries - Chemically bonded solid electrolyte interface and nanochannel formation. *J Electrochem Soc* **143**, L4-L7, doi:Doi 10.1149/1.1836372 (1996).

8 Shodai, T., Okada, S., Tobishima, S. & Yamaki, J. Study of $Li_{(3-x)}M_{(x)}N$ (M:Co,Ni or Cu) system for use as anode material in lithium rechargeable cells. *Solid State Ionics* **86-8**, 785-789, doi:Doi 10.1016/0167-2738(96)00174-9 (1996).

9 Yu, X. Q. *et al.* Nanocrystalline MnO thin film anode for lithium ion batteries with low overpotential. *Electrochemistry Communications* **11**, 791-794, doi:DOI 10.1016/j.elecom.2009.01.040 (2009).

10 Choi, H. S., Lee, J. G., Lee, H. Y., Kim, S. W. & Park, C. R. Effects of surrounding confinements of Si nanoparticles on Si-based anode performance for lithium ion batteries. *Electrochimica Acta* **56**, 790-796, doi:DOI 10.1016/j.electacta.2010.09.101 (2010).

11 Courtney, I. A. & Dahn, J. R. Electrochemical and in situ x-ray diffraction studies of the reaction of lithium with tin oxide composites. *J Electrochem Soc* **144**, 2045-2052, doi:Doi 10.1149/1.1837740 (1997).

12 Idota, Y., Kubota, T., Matsufuji, A., Maekawa, Y. & Miyasaka, T. Tin-based amorphous oxide: A high-capacity lithium-ion-storage material. *Science* **276**, 1395-1397, doi:DOI 10.1126/science.276.5317.1395 (1997).

13 Ren, J. G. *et al.* Germanium-graphene composite anode for high-energy lithium batteries with long cycle life. *J Mater Chem A* **1**, 1821-1826, doi:Doi 10.1039/C2ta01286c (2013).

14 Murphy, D. W. & Christian, P. A. Solid-State Electrodes for High-Energy Batteries. *Science* **205**, 651-656, doi:DOI 10.1126/science.205.4407.651 (1979).

15 Mizushima, K., Jones, P. C., Wiseman, P. J. & Goodenough, J. B. $Li_xCoO_2$ "(Oless-Thanxless-Than-or-Equal-To1) - a New Cathode Material for Batteries of High-Energy Density. *Mater Res Bull* **15**, 783-789, doi:Doi 10.1016/0025-5408(80)90012-4 (1980).

16 Thackeray, M. M., David, W. I. F., Bruce, P. G. & Goodenough, J. B. Lithium Insertion into Manganese Spinels. *Mater Res Bull* **18**, 461-472, doi:Doi 10.1016/0025-5408(83)90138-1 (1983).

17 Murphy, D. W., Disalvo, F. J., Carides, J. N. & Waszczak, J. V. Topochemical Reactions of Rutile Related Structures with Lithium. *Mater Res Bull* **13**, 1395-1402, doi:Doi 10.1016/0025-5408(78)90131-9 (1978).

18 Lazzari, M. & Scrosati, B. Cyclable Lithium Organic Electrolyte Cell Based on 2 Intercalation Electrodes. *J Electrochem Soc* **127**, 773-774, doi:Doi 10.1149/1.2129753 (1980).

19 Wakihara, M., Ikuta, H. & Uchimoto, Y. Structural Stability in Partially Substituted Lithium Manganese Spinel Oxide Cathode. *Ionics* **8**, 329-338, doi:Doi 10.1007/Bf02376045 (2002).

20 Patoux, S. *et al.* High voltage nickel manganese spinel oxides for Li-ion batteries. *Electrochimica Acta* **53**, 4137-4145, doi:DOI 10.1016/j.electacta.2007.12.054 (2008).

21 Basu, S. *et al.* Synthesis and Properties of Lithium-Graphite Intercalation Compounds. *Mater Sci Eng* **38**, 275-283, doi:Doi 10.1016/0025-5416(79)90132-0 (1979).

22 Zanini, M., Basu, S. & Fischer, J. E. Alternate Synthesis and Reflectivity Spectrum of Stage 1 Lithium-Graphite Intercalation Compound. *Carbon* **16**, 211-212, doi:Doi 10.1016/0008-6223(78)90026-X (1978).

23 Yazami, R. & Touzain, P. A Reversible Graphite Lithium Negative Electrode for Electrochemical Generators. *Journal of Power Sources* **9**, 365-371, doi:Doi 10.1016/0378-7753(83)87040-2 (1983).

24 Aurbach, D. *et al.* The Study of Electrolyte-Solutions Based on Ethylene and Diethyl Carbonates for Rechargeable Li Batteries .1. Li Metal Anodes. *J Electrochem Soc* **142**, 2873-2882, doi:Doi 10.1149/1.2048658 (1995).

25 Goodenough, J. B. & Kim, Y. Challenges for Rechargeable Li Batteries. *Chemistry of Materials* **22**, 587-603, doi:Doi 10.1021/Cm901452z (2010).

26 Armand, M. & Tarascon, J. M. Building better batteries. *Nature* **451**, 652-657, doi:Doi 10.1038/451652a (2008).

27 Cheng, F., Tao, Z., Liang, J. & Chen, J. Template-directed materials for rechargeable lithium-ion batteries. *Chemistry of Materials* **20**, 667-681, doi:Doi 10.1021/Cm702091q (2008).

28 Nishi, Y. The development of lithium ion secondary batteries. *Chem Rec* **1**, 406-413, doi:Doi 10.1002/Tcr.1024 (2001).

29 Dillon, A. C. Carbon Nanotubes for Photoconversion and Electrical Energy Storage. *Chem Rev* **110**, 6856-6872, doi:Doi 10.1021/Cr9003314 (2010).

30 Bhardwaj, T., Antic, A., Pavan, B., Barone, V. & Fahlman, B. D. Enhanced Electrochemical Lithium Storage by Graphene Nanoribbons. *Journal of the American Chemical Society* **132**, 12556-12558, doi:Doi 10.1021/Ja106162f (2010).

31 Hu, Y. S. *et al.* Synthesis of hierarchically porous carbon monoliths with highly ordered microstructure and their application in rechargeable lithium batteries with high-rate capability. *Adv Funct Mater* **17**, 1873-1878, doi:DOI 10.1002/adfm.200601152 (2007).

32 Li, H., Huang, X. J. & Chen, L. Q. Anodes based on oxide materials for lithium rechargeable batteries. *Solid State Ionics* **123**, 189-197, doi:Doi 10.1016/S0167-2738(99)00081-8 (1999).

33 Holzapfel, M., Buqa, H., Scheifele, W., Novak, P. & Petrat, F. M. A new type of nano-sized silicon/carbon composite electrode for reversible lithium insertion. *Chem Commun*, 1566-1568, doi:Doi 10.1039/B417492e (2005).

34 Cui, G. L. *et al.* A Germanium-Carbon Nanocomposite Material for Lithium Batteries. *Advanced Materials* **20**, 3079-3083, doi:DOI 10.1002/adma.200800586 (2008).

35 Armstrong, G., Armstrong, A. R., Bruce, P. G., Reale, P. & Scrosati, B. TiO2(B) nanowires as an improved anode material for lithium-ion batteries containing LiFePO4 or $LiNi_{0.5}Mn_{1.5}O_4$ cathodes and a polymer electrolyte. *Advanced Materials* **18**, 2597, doi:DOI 10.1002/adma.200601232 (2006).

36 Cui, G. L., Gu, L., Kaskhedikar, N., van Aken, P. A. & Maier, J. A novel germanium/carbon nanotubes nanocomposite for lithium storage material. *Electrochimica Acta* **55**, 985-988, doi:DOI 10.1016/j.electacta.2009.08.056 (2010).

37 Kim, H. S., Chung, K. Y. & Cho, B. W. Electrochemical properties of carbon-coated Si/B composite anode for lithium ion batteries. *Journal of Power Sources* **189**, 108-113, doi:DOI 10.1016/j.jpowsour.2008.10.045 (2009).

38 Zuo, P. J. & Yin, G. P. Si-Mn composite anodes for lithium ion batteries. *J Alloy Compd* **414**, 265-268, doi:DOI 10.1016/j.jallcom.2005.07.026 (2006).

39 Shimoi, N. & Tanaka, Y. Improvement in Si active material particle performance for lithium-ion batteries by surface modification of an inductivity coupled plasma-chemical vapor deposition. *Electrochimica Acta* **80**, 227-232, doi:DOI 10.1016/j.electacta.2012.07.006 (2012).

40 Zheng, Y., Yang, J., Wang, J. L. & NuLi, Y. N. Nano-porous Si/C composites for anode material of lithium-ion batteries. *Electrochimica Acta* **52**, 5863-5867, doi:DOI 10.1016/j.electacta.2007.03.013 (2007).

41 Zhang, X. N., Pan, G. L., Li, G. R., Qu, J. Q. & Gao, X. P. Si-Si(3)N(4) composites as anode materials for lithium ion batteries. *Solid State Ionics* **178**, 1107-1112, doi:DOI 10.1016/j.ssi.2007.05.011 (2007).

42 Youn, D. Y., Tuller, H. L., Hyun, T. S., Choi, D. K. & Kim, I. D. Facile Synthesis of Highly Conductive $RuO_2$-$Mn_3O_4$ Composite Nanofibers via Electrospinning and Their Electrochemical Properties. *J Electrochem Soc* **158**, A970-A975, doi:Doi 10.1149/1.3601852 (2011).

43 Wang, J. G., Yang, Y., Huang, Z. H. & Kang, F. Y. Synthesis and electrochemical performance of $MnO_2$/CNTs-embedded carbon nanofibers nanocomposites for supercapacitors. *Electrochimica Acta* **75**, 213-219, doi:DOI 10.1016/j.electacta.2012.04.088 (2012).

44 Hashem, A. M., Abuzeid, H. M., Nikolowski, K. & Ehrenberg, H. Table sugar as preparation and carbon coating reagent for facile synthesis and coating of rod-shaped $MnO_2$. *J Alloy Compd* **497**, 300-303, doi:DOI 10.1016/j.jallcom.2010.03.039 (2010).

45 Han, H. *et al.* Nitridated $TiO_2$ hollow nanofibers as an anode material for high power lithium ion batteries. *Energy & Environmental Science* **4**, 4532-4536, doi:Doi 10.1039/C1ee02333k (2011).

46 Ryu, W. H., Nam, D. H., Ko, Y. S., Kim, R. H. & Kwon, H. S. Electrochemical performance of a smooth and highly ordered $TiO_2$ nanotube electrode for Li-ion batteries. *Electrochimica Acta* **61**, 19-24, doi:DOI 10.1016/j.electacta.2011.11.042 (2012).

47 Poizot, P., Laruelle, S., Grugeon, S., Dupont, L. & Tarascon, J. M. Nano-sized transition-metaloxides as negative-electrode materials for lithium-ion batteries. *Nature* **407**, 496-499 (2000).

48 Wang, W. *et al.* Nanostructured $Li_4Ti_5O_{12}$ synthesized in a reverse micelle: A bridge between pseudocapacitor and lithium ion battery. *Electrochimica Acta* **68**, 254-259, doi:DOI 10.1016/j.electacta.2012.02.088 (2012).

49 Shen, L. F. *et al.* In situ growth of $Li_4Ti_5O_{12}$ on multi-walled carbon nanotubes: novel coaxial nanocables for high rate lithium ion batteries. *Journal of Materials Chemistry* **21**, 761-767, doi:Doi 10.1039/C0jm02316g (2011).

50 Li, J., Jin, Y. L., Zhang, X. G. & Yang, H. Microwave solid-state synthesis of spinel $Li_4Ti_5O_{12}$ nanocrystallites as anode material for lithium-ion batteries. *Solid State Ionics* **178**, 1590-1594, doi:DOI 10.1016/j.ssi.2007.10.012 (2007).

51 Jin, Y. H. *et al.* Facile synthesis of nano-$Li_4Ti_5O_{12}$ for high-rate Li-ion battery anodes. *Nanoscale Res Lett* **7**, 1-6, doi:Artn 10 Doi 10.1186/1556-276x-7-10 (2012).

52 Gu, Y. J. *et al.* Influence of calcinations temperature on crystallization and synthesis process of $Li_4Ti_5O_{12}$. *Advanced Materials, Pts 1-4* **239-242**, 1858-1861, doi:DOI 10.4028 (2011).

53 Li, N., Zhou, G. M., Li, F., Wen, L. & Cheng, H. M. A Self-Standing and Flexible Electrode of Li4Ti5O12 Nanosheets with a N-Doped Carbon Coating for High Rate Lithium Ion Batteries. *Adv Funct Mater* **23**, 5429-5435, doi:DOI 10.1002/adfm.201300495 (2013).

54 Zhao, X., Hayner, C. M. & Kung, H. H. Self-assembled lithium manganese oxide nanoparticles on carbon nanotube or graphene as high-performance cathode material for lithium-ion batteries. *Journal of Materials Chemistry* **21**, 17297-17303, doi:Doi 10.1039/C1jm12373d (2011).

55 Lin, B. H., Yin, Q., Hu, H. R., Lu, F. J. & Xia, H. $LiMn_2O_4$ nanoparticles anchored on graphene nanosheets as high-performance cathode material for lithium-ion batteries. *J Solid State Chem* **209**, 23-28, doi:DOI 10.1016/j.jssc.2013.10.016 (2014).

56 Wang, D. *et al.* beta-$MnO_2$ as a cathode material for lithium ion batteries from first principles calculations. *Phys Chem Chem Phys* **15**, 9075-9083, doi:Doi 10.1039/C3cp50392e (2013).

57 Ammundsen, B. & Paulsen, J. Novel lithium-ion cathode materials based on layered manganese oxides. *Advanced Materials* **13**, 943, doi:Doi 10.1002 (2001).

58 Dahn, J. R., Vonsacken, U., Juzkow, M. W. & Aljanaby, H. Rechargeable $LiNiO_2$ Carbon Cells. *J Electrochem Soc* **138**, 2207-2211, doi:Doi 10.1149/1.2085950 (1991).

59 Li, C. *et al.* Cathode materials modified by surface coating for lithium ion batteries. *Electrochimica Acta* **51**, 3872-3883, doi:DOI 10.1016/j.electacta.2005.11.015 (2006).

60 Fergus, J. W. Recent developments in cathode materials for lithium ion batteries. *Journal of Power Sources* **195**, 939-954, doi:DOI 10.1016/j.jpowsour.2009.08.089 (2010).

61 Jiang, Y. *et al.* Graphene modified Li3V2(PO4)(3) as a high-performance cathode material for lithium ion batteries. *Electrochimica Acta* **85**, 377-383, doi:DOI 10.1016/j.electacta.2012.08.067 (2012).

62 Cheng, J. L. *et al.* Self-assembled $V_2O_5$ nanosheets/reduced graphene oxide hierarchical nanocomposite as a high-performance cathode material for lithium ion batteries. *J Mater Chem A* **1**, 10814-10820, doi:Doi 10.1039/C3ta12066j (2013).

63 Cao, A. M., Hu, J. S., Liang, H. P. & Wan, L. J. Self-assembled vanadium pentoxide ($V_2O_5$) hollow microspheres from nanorods and their application in lithium-ion batteries. *Angew Chem Int Edit* **44**, 4391-4395, doi:DOI 10.1002/anie.200500946 (2005).

64 Li, G. C., Pang, S. P., Jiang, L., Guo, Z. Y. & Zhang, Z. K. Environmentally friendly chemical route to vanadium oxide single-crystalline nanobelts as a cathode material for lithium-ion batteries. *J Phys Chem B* **110**, 9383-9386, doi:Doi 10.1021/Jp060904s (2006).

65 Shi, Y. *et al.* Graphene wrapped $LiFePO_4$/C composites as cathode materials for Li-ion batteries with enhanced rate capability. *Journal of Materials Chemistry* **22**, 16465-16470, doi:Doi 10.1039/C2jm32649c (2012).

66 Wu, X. L. *et al.* Carbon-Nanotube-Decorated Nano-$LiFePO_4$ @C Cathode Material with Superior High-Rate and Low-Temperature Performances for Lithium-Ion Batteries. *Advanced Energy Materials* **3**, 1155-1160, doi:DOI 10.1002/aenm.201300159 (2013).

67 Hu, L. H., Wu, F. Y., Lin, C. T., Khlobystov, A. N. & Li, L. J. Graphene-modified $LiFePO_4$ cathode for lithium ion battery beyond theoretical capacity. *Nat Commun* **4**, doi:Artn 1687 Doi 10.1038/Ncomms2705 (2013).

68 Yang, S. F., Zavalij, P. Y. & Whittingham, M. S. Hydrothermal synthesis of lithium iron phosphate cathodes. *Electrochemistry Communications* **3**, 505-508, doi:Doi 10.1016/S1388-2481(01)00200-4 (2001).

69 Chen, J. J. & Whittingham, M. S. Hydrothermal synthesis of lithium iron phosphate. *Electrochemistry Communications* **8**, 855-858, doi:DOI 10.1016/j.elecom.2006.03.021 (2006).

70 Li, J. L., Cao, C. B., Xu, X. Y., Zhu, Y. Q. & Yao, R. M. $LiNi_{1/3}Co_{1/3}Mn_{1/3}O_2$ hollow nano-micro hierarchical microspheres with enhanced performances as cathodes for lithium-ion batteries. *J Mater Chem A* **1**, 11848-11852, doi:Doi 10.1039/C3ta12375h (2013).

71 Yabuuchi, N. & Ohzuku, T. Novel lithium insertion material of $LiCo_{1/3}Ni_{1/3}Mn_{1/3}O_2$ for advanced lithium-ion batteries. *Journal of Power Sources* **119**, 171-174, doi:Doi 10.1016/S0378-7753(03)00173-3 (2003).

72 Kim, Y., Kim, H. S. & Martin, S. W. Synthesis and electrochemical characteristics of $Al_2O_3$-coated $LiNi_{1/3}Co_{1/3}Mn_{1/3}O_2$ cathode materials for lithium ion batteries. *Electrochimica Acta* **52**, 1316-1322, doi:DOI 10.1016/j.electacta.2006.07.033 (2006).

73 Yoshizawa, H. & Ohzuku, T. An application of lithium cobalt nickel manganese oxide to high-power and high-energy density lithium-ion batteries. *Journal of Power Sources* **174**, 813-817, doi:DOI 10.1016/j.jpowsour.2007.06.153 (2007).

74 Etacheri, V., Marom, R., Elazari, R., Salitra, G. & Aurbach, D. Challenges in the development of advanced Li-ion batteries: a review. *Energy & Environmental Science* **4**, 3243-3262, doi:Doi 10.1039/C1ee01598b (2011).

75 Etacheri, V. *et al.* Effect of Fluoroethylene Carbonate (FEC) on the Performance and Surface Chemistry of Si-Nanowire Li-Ion Battery Anodes. *Langmuir* **28**, 965-976, doi:Doi 10.1021/La203712s (2012).

76 Choi, H. C., Jung, Y. M., Noda, I. & Kim, S. B. A study of the mechanism of the electrochemical reaction of lithium with CoO by two-dimensional soft X-ray absorption spectroscopy (2D XAS), 2D Raman, and 2D heterospectral XAS-Raman correlation analysis. *J Phys Chem B* **107**, 5806-5811, doi:Doi 10.1021/Jp030438w (2003).

77 Arora, P., White, R. E. & Doyle, M. Capacity fade mechanisms and side reactions in lithium-ion batteries. *J Electrochem Soc* **145**, 3647-3667, doi:Doi 10.1149/1.1838857 (1998).

78 Vetter, J. *et al.* Ageing mechanisms in lithium-ion batteries. *Journal of Power Sources* **147**, 269-281, doi:DOI 10.1016/j.jpowsour.2005.01.006 (2005).

79 Aurbach, D. Review of selected electrode-solution interactions which determine the performance of Li and Li ion batteries. *Journal of Power Sources* **89**, 206-218, doi:Doi 10.1016/S0378-7753(00)00431-6 (2000).

80 Rossen, E., Reimers, J. N. & Dahn, J. R. Synthesis and Electrochemistry of Spinel Lt-$LiCoO_2$. *Solid State Ionics* **62**, 53-60, doi:Doi 10.1016/0167-2738(93)90251-W (1993).

81 Gabrisch, H., Yazami, R. & Fultz, B. Hexagonal to cubic spinel transformation in lithiated cobalt oxide - TEM investigation. *J Electrochem Soc* **151**, A891-A897, doi:Doi 10.1149/1.1738677 (2004).

82 Kamali, A. R. & Fray, D. J. Review on Carbon and Silicon Based Materials as Anode Materials for Lithium Ion Batteries. *J New Mat Electr Sys* **13**, 147-160 (2010).

83 Peled, E. The Electrochemical-Behavior of Alkali and Alkaline-Earth Metals in Non-Aqueous Battery Systems - the Solid Electrolyte Interphase Model. *J Electrochem Soc* **126**, 2047-2051, doi:Doi 10.1149/1.2128859 (1979).

84 Guyomard, D. & Tarascon, J. M. Li Metal-Free Rechargeable Limn2o4/Carbon Cells - Their Understanding and Optimization. *J Electrochem Soc* **139**, 937-948, doi:Doi 10.1149/1.2069372 (1992).

85 Tarascon, J. M. *et al.* Synthesis Conditions and Oxygen Stoichiometry Effects on Li Insertion into the Spinel $LiMn_2O_4$. *J Electrochem Soc* **141**, 1421-1431, doi:Doi 10.1149/1.2054941 (1994).

86 Aurbach, D. & Gottlieb, H. The Electrochemical-Behavior of Selected Polar Arotic Systems. *Electrochimica Acta* **34**, 141-156, doi:Doi 10.1016/0013-4686(89)87079-3 (1989).

87 Aurbach, D. *et al.* Design of electrolyte solutions for Li and Li-ion batteries: a review. *Electrochimica Acta* **50**, 247-254, doi:DOI 10.1016/j.electacta.2004.01.090 (2004).

88 Shu, J. Study of the Interface Between $Li_4Ti_5O_{12}$ Electrodes and Standard Electrolyte Solutions in 0.0-5.0 V (vol 11, pg A238, 2008). *Electrochem Solid St* **12**, S9-S9 (2009).

89 Tarascon, J. M. Key challenges in future Li-battery research. *Philos T R Soc A* **368**, 3227-3241, doi:DOI 10.1098/rsta.2010.0112 (2010).

90 Zhang, S. S. A review on the separators of liquid electrolyte Li-ion batteries. *Journal of Power Sources* **164**, 351-364, doi:DOI 10.1016/j.jpowsour.2006.10.065 (2007).

91 Owens, B. *et al.* Panel discussion - Future prospects of lithium batteries. *Journal of Power Sources* **68**, 173-186, doi:Doi 10.1016/S0378-7753(96)02620-1 (1997).

92 Murata, K. An Overview of the Research-and-Development of Solid Polymer Electrolyte Batteries. *Electrochimica Acta* **40**, 2177-2184, doi:Doi 10.1016/0013-4686(95)00160-G (1995).

93 Bierwagen, G. P. Film Coating Technologies and Adhesion. *Electrochimica Acta* **37**, 1471-1478, doi:Doi 10.1016/0013-4686(92)80092-Z (1992).

94 Fenton, D. E., Parker, J. M. & Wright, P. V. Complexes of Alkali-Metal Ions with Poly(Ethylene Oxide). *Polymer* **14**, 589-589, doi:Doi 10.1016/0032-3861(73)90146-8 (1973).

95 Koksbang, R., Olsen, I. I. & Shackle, D. Review of Hybrid Polymer Electrolytes and Rechargeable Lithium Batteries. *Solid State Ionics* **69**, 320-335, doi:Doi 10.1016/0167-2738(94)90420-0 (1994).

96 Meyer, W. H. Polymer electrolytes for lithium-ion batteries. *Advanced Materials* **10**, 439, doi:Doi 10.1002 (1998).

97 Brandt, K. Historical Development of Secondary Lithium Batteries. *Solid State Ionics* **69**, 173-183, doi:Doi 10.1016/0167-2738(94)90408-1 (1994).

98 Evans, J., Vincent, C. A. & Bruce, P. G. Electrochemical Measurement of Transference Numbers in Polymer Electrolytes. *Polymer* **28**, 2324-2328, doi:Doi 10.1016/0032-3861(87)90394-6 (1987).

99 Bruce, P. G., Hardgrave, M. T. & Vincent, C. A. The Determination of Transference Numbers in Solid Polymer Electrolytes Using the Hittorf Method. *Solid State Ionics* **53**, 1087-1094, doi:Doi 10.1016/0167-2738(92)90295-Z (1992).

100 Jiao, F. & Bruce, P. G. Mesoporous crystalline beta-$MnO_2$- a reversible positive electrode for rechargeable lithium batteries. *Advanced Materials* **19**, 657, doi:DOI 10.1002/adma.200602499 (2007).

101 Larcher, D. *et al.* Effect of particle size on lithium intercalation into alpha-$Fe_2O_3$. *J Electrochem Soc* **150**, A133-A139, doi:Doi 10.1149/1.1528941 (2003).

102 Balaya, P. *et al.* Nano-ionics in the context of lithium batteries. *Journal of Power Sources* **159**, 171-178, doi:DOI 10.1016/j.jpowsour.2006.04.115 (2006).

103 Balaya, P., Li, H., Kienle, L. & Maier, J. Fully reversible homogeneous and heterogeneous Li storage in $RuO_2$ with high capacity. *Adv Funct Mater* **13**, 621-625, doi:DOI 10.1002/adfm.200304406 (2003).

104 Li, H., Richter, G. & Maier, J. Reversible formation and decomposition of LiF clusters using transition metal fluorides as precursors and their application in rechargeable Li batteries. *Advanced Materials* **15**, 736-739, doi:DOI 10.1002/adma.200304574 (2003).

105 Meethong, N., Huang, H. Y. S., Carter, W. C. & Chiang, Y. M. Size-dependent lithium miscibility gap in nanoscale $Li_{1-x}FePO_4$. *Electrochem Solid St* **10**, A134-A138, doi:Doi 10.1149/1.2710960 (2007).

106 Chan, C. K. *et al.* High-performance lithium battery anodes using silicon nanowires. *Nature nanotechnology* **3**, 31-35, doi:DOI 10.1038/nnano.2007.411 (2008).

107 Tobishima, S., Takei, K., Sakurai, Y. & Yamaki, J. Lithium ion cell safety. *Journal of Power Sources* **90**, 188-195, doi:Doi 10.1016/S0378-7753(00)00409-2 (2000).

108 Bruce, P. G., Scrosati, B. & Tarascon, J. M. Nanomaterials for rechargeable lithium batteries. *Angew Chem Int Edit* **47**, 2930-2946, doi:DOI 10.1002/anie.200702505 (2008).

109 Li, H., Wang, Z. X., Chen, L. Q. & Huang, X. J. Research on Advanced Materials for Li-ion Batteries. *Advanced Materials* **21**, 4593-4607, doi:DOI 10.1002/adma.200901710 (2009).

110 Hu, Y. S., Kienle, L., Guo, Y. G. & Maier, J. High lithium electroactivity of nanometer-sized rutile $TiO_2$. *Advanced Materials* **18**, 1421, doi:DOI 10.1002/adma.200502723 (2006).

111 Fu, Y. J. *et al.* Self-supporting $Co_3O_4$ with lemongrass-like morphology as a high-performance anode material for lithium ion batteries. *Journal of Materials Chemistry* **22**, 17429-17431, doi:Doi 10.1039/C2jm33704e (2012).

112 Wang, H. L. *et al.* $Mn_3O_4$-Graphene Hybrid as a High-Capacity Anode Material for Lithium Ion Batteries. *Journal of the American Chemical Society* **132**, 13978-13980, doi:Doi 10.1021/Ja105296a (2010).

113 Chen, Y., Xia, H., Lu, L. & Xue, J. M. Synthesis of porous hollow $Fe_3O_4$ beads and their applications in lithium ion batteries. *Journal of Materials Chemistry* **22**, 5006-5012, doi:Doi 10.1039/C2jm15440d (2012).

114 Guan, H. *et al.* CoO octahedral nanocages for high-performance lithium ion batteries. *Chem Commun* **48**, 4878-4880, doi:Doi 10.1039/C2cc30843f (2012).

115 Dimov, N., Kugino, S. & Yoshio, M. Carbon-coated silicon as anode material for lithium ion batteries: advantages and limitations. *Electrochimica Acta* **48**, 1579-1587, doi:Doi 10.1016/S0013-4686(03)00030-6 (2003).

116 Chen, L. B., Xie, J. Y., Yu, H. C. & Wang, T. H. Si-Al thin film anode material with superior cycle performance and rate capability for lithium ion batteries. *Electrochimica Acta* **53**, 8149-8153, doi:DOI 10.1016/j.electacta.2008.06.025 (2008).

117 Park, M. S., Wang, G. X., Liu, H. K. & Dou, S. X. Electrochemical properties of Si thin film prepared by pulsed laser deposition for lithium ion micro-batteries. *Electrochimica Acta* **51**, 5246-5249, doi:DOI 10.1016/j.electacta.2006.01.045 (2006).

118 Zhao, X., Hayner, C. M., Kung, M. C. & Kung, H. H. In-Plane Vacancy-Enabled High-Power Si-Graphene Composite Electrode for Lithium-Ion Batteries. *Advanced Energy Materials* **1**, 1079-1084, doi:DOI 10.1002/aenm.201100426 (2011).

119 Cao, F. F. *et al.* Cu-Si Nanocable Arrays as High-Rate Anode Materials for Lithium-Ion Batteries. *Advanced Materials* **23**, 4415, doi:DOI 10.1002/adma.201102062 (2011).

120 Kumai, Y. *et al.* Si-C composite anode of layered polysilane (Si6H6) and sucrose for lithium ion rechargeable batteries. *Journal of Materials Chemistry* **21**, 11941-11946, doi:Doi 10.1039/C1jm10532a (2011).

121 Hu, Y. S. *et al.* Superior storage performance of a Si@$SiO_x$/C nanocomposite as anode material for lithium-ion batteries. *Angew Chem Int Edit* **47**, 1645-1649, doi:DOI 10.1002/anie.200704287 (2008).

122 Chan, C. K., Zhang, X. F. & Cui, Y. High capacity Li ion battery anodes using Ge nanowires. *Nano letters* **8**, 307-309, doi:Doi 10.1021/Nl0727157 (2008).

123 Wu, H. & Cui, Y. Designing nanostructured Si anodes for high energy lithium ion batteries. *Nano Today* **7**, 414-429, doi:DOI 10.1016/j.nantod.2012.08.004 (2012).

124 Besenhard, J. O., Yang, J. & Winter, M. Will advanced lithium-alloy anodes have a chance in lithium-ion batteries? *Journal of Power Sources* **68**, 87-90, doi:Doi 10.1016/S0378-7753(96)02547-5 (1997).

125 Beaulieu, L. Y., Eberman, K. W., Turner, R. L., Krause, L. J. & Dahn, J. R. Colossal reversible volume changes in lithium alloys. *Electrochem Solid St* **4**, A137-A140, doi:Doi 10.1149/1.1388178 (2001).

126 Chevrier, V. L., Zwanziger, J. W. & Dahn, J. R. First principles study of Li-Si crystalline phases: Charge transfer, electronic structure, and lattice vibrations. *J Alloy Compd* **496**, 25-36, doi:DOI 10.1016/j.jallcom.2010.01.142 (2010).

127 Verma, P., Maire, P. & Novak, P. A review of the features and analyses of the solid electrolyte interphase in Li-ion batteries. *Electrochimica Acta* **55**, 6332-6341, doi:DOI 10.1016/j.electacta.2010.05.072 (2010).

128 Shimizu, T. *et al.* Synthesis of vertical high-density epitaxial Si(100) nanowire arrays on a Si(100) substrate using an anodic aluminum oxide template. *Advanced Materials* **19**, 917, doi:DOI 10.1002/adma.200700153 (2007).

129 Liu, W. R. *et al.* Electrochemical characterizations on Si and C-coated Si particle electrodes for lithium-ion batteries. *J Electrochem Soc* **152**, A1719-A1725, doi:Doi 10.1149/1.1954967 (2005).

130 Yao, Y. *et al.* Interconnected Silicon Hollow Nanospheres for Lithium-Ion Battery Anodes with Long Cycle Life. *Nano letters* **11**, 2949-2954, doi:Doi 10.1021/Nl201470j (2011).

131 Evanoff, K. *et al.* Ultra Strong Silicon-Coated Carbon Nanotube Nonwoven Fabric as a Multifunctional Lithium-Ion Battery Anode. *Acs Nano* **6**, 9837-9845, doi:Doi 10.1021/Nn303393p (2012).

132 Guo, J. C. & Wang, C. S. A polymer scaffold binder structure for high capacity silicon anode of lithium-ion battery. *Chem Commun* **46**, 1428-1430, doi:Doi 10.1039/B918727h (2010).

133 Kovalenko, I. *et al.* A Major Constituent of Brown Algae for Use in High-Capacity Li-Ion Batteries. *Science* **334**, 75-79, doi:DOI 10.1126/science.1209150 (2011).

134 Debart, A., Dupont, L., Poizot, P., Leriche, J. B. & Tarascon, J. M. A transmission electron microscopy study of the reactivity mechanism of tailor-made CuO particles toward lithium. *J Electrochem Soc* **148**, A1266-A1274 (2001).

135 Poizot, P. *et al.* Electrochemical reactivity and reversibility of cobalt oxides towards lithium. *Cr Acad Sci Ii C* **3**, 681-691, doi:Doi 10.1016/S1387-1609(00)01148-8 (2000).

136 Choi, B. G. *et al.* 3D heterostructured architectures of $Co_3O_4$ nanoparticles deposited on porous graphene surfaces for high performance of lithium ion batteries. *Nanoscale* **4**, 5924-5930, doi:Doi 10.1039/C2nr31438j (2012).

137 Du, N. *et al.* Porous $Co_3O_4$ nanotubes derived from $Co_4(CO)(12)$ clusters on carbon nanotube templates: A highly efficient material for Li-battery applications. *Advanced Materials* **19**, 4505, doi:DOI 10.1002/adma.200602513 (2007).

138 Li, Y., Tan, B. & Wu, Y. Mesoporous $Co_3O_4$ nanowire arrays for lithium ion batteries with high capacity and rate capability. *Nano letters* **8**, 265-270, doi:10.1021/nl0725906 (2008).

139 Wang, X. *et al.* Synthesis of Single-Crystalline $Co_3O_4$ Octahedral Cages with Tunable Surface Aperture and Their Lithium Storage Properties. *J Phys Chem C* **113**, 15553-15558, doi:Doi 10.1021/Jp904652m (2009).

140 Wu, Z. S. *et al.* Graphene Anchored with $Co_3O_4$ Nanoparticles as Anode of Lithium Ion Batteries with Enhanced Reversible Capacity and Cyclic Performance. *Acs Nano* **4**, 3187-3194, doi:Doi 10.1021/Nn100740x (2010).

141 Paek, S. M., Yoo, E. & Honma, I. Enhanced Cyclic Performance and Lithium Storage Capacity of $SnO_2$/Graphene Nanoporous Electrodes with Three-Dimensionally Delaminated Flexible Structure. *Nano letters* **9**, 72-75, doi:Doi 10.1021/Nl802484w (2009).

142 Kim, H., Han, B., Choo, J. & Cho, J. Three-Dimensional Porous Silicon Particles for Use in High-Performance Lithium Secondary Batteries. *Angew Chem Int Edit* **47**, 10151-10154, doi:DOI 10.1002/anie.200804355 (2008).

143 Yu, Y. *et al.* Reversible Storage of Lithium in Silver-Coated Three-Dimensional Macroporous Silicon. *Advanced Materials* **22**, 2247, doi:DOI 10.1002/adma.200903755 (2010).

144 Raimann, P. R. *et al.* Monitoring dynamics of electrode reactions in Li-ion batteries by in situ ESEM. *Ionics* **12**, 253-255, doi:DOI 10.1007/s11581-006-0046-y (2006).

145 Cui, L. F., Hu, L. B., Choi, J. W. & Cui, Y. Light-Weight Free-Standing Carbon Nanotube-Silicon Films for Anodes of Lithium Ion Batteries. *Acs Nano* **4**, 3671-3678, doi:Doi 10.1021/Nn100619m (2010).

146 Ge, M. Y. *et al.* Scalable preparation of porous silicon nanoparticles and their application for lithium-ion battery anodes. *Nano Research* **6**, 174-181, doi:DOI 10.1007/s12274-013-0293-y (2013).

147 Hassan, F., Chabot, V., Elsayed, A. R., Xiao, X. & Chen, Z. Engineered Si electrode nano-architecture: A scalable treatment for the production of next-generation Li-ion batteries. *Nano letters* (2013).

148 Bruk, M. A. *et al.* A New Type of Nanostructure in Si/C Composite Electrodes for Lithium-Ion Batteries. *Inorg Mater+* **44**, 1086-1090, doi:Doi 10.1134/S0020168508100117 (2008).

149 Camer, J. L. G. *et al.* Nanosized Si/cellulose fiber/carbon composites as high capacity anodes for lithium-ion batteries: A galvanostatic and dilatometric study. *Electrochimica Acta* **54**, 6713-6717, doi:DOI 10.1016/j.electacta.2009.06.085 (2009).

150 Ji, L. W. & Zhang, X. W. Evaluation of Si/carbon composite nanofiber-based insertion anodes for new-generation rechargeable lithium-ion batteries. *Energy & Environmental Science* **3**, 124-129, doi:Doi 10.1039/B912188a (2010).

151 Jang, S. M., Miyawaki, J., Tsuji, M., Mochida, I. & Yoon, S. H. The preparation of a novel Si-CNF composite as an effective anodic material for lithium-ion batteries. *Carbon* **47**, 3383-3391, doi:DOI 10.1016/j.carbon.2009.07.018 (2009).

152 Wu, H. *et al.* Stable cycling of double-walled silicon nanotube battery anodes through solid-electrolyte interphase control. *Nature nanotechnology* **7**, 309-314, doi:Doi 10.1038/Nnano.2012.35 (2012).

153 Novoselov, K. S. *et al.* Electric field effect in atomically thin carbon films. *Science* **306**, 666-669, doi:DOI 10.1126/science.1102896 (2004).

154 Wang, H. L. *et al.* Graphene-Wrapped Sulfur Particles as a Rechargeable Lithium-Sulfur Battery Cathode Material with High Capacity and Cycling Stability. *Nano letters* **11**, 2644-2647, doi:Doi 10.1021/Nl200658a (2011).

155 Geim, A. K. & Novoselov, K. S. The rise of graphene. *Nat Mater* **6**, 183-191, doi:Doi 10.1038/Nmat1849 (2007).

156 Wu, J. S., Pisula, W. & Mullen, K. Graphenes as potential material for electronics. *Chem Rev* **107**, 718-747, doi:Doi 10.1021/Cr068010r (2007).

157 Zou, Y. Q. & Wang, Y. NiO nanosheets grown on graphene nanosheets as superior anode materials for Li-ion batteries. *Nanoscale* **3**, 2615-2620, doi:Doi 10.1039/C1nr10070j (2011).

158 Tao, H. C., Fan, L. Z., Mei, Y. F. & Qu, X. H. Self-supporting Si/Reduced Graphene Oxide nanocomposite films as anode for lithium ion batteries. *Electrochemistry Communications* **13**, 1332-1335, doi:DOI 10.1016/j.elecom.2011.08.001 (2011).

159 Xin, X. *et al.* A 3D porous architecture of Si/graphene nanocomposite as high-performance anode materials for Li-ion batteries. *Journal of Materials Chemistry* **22**, 7724-7730, doi:Doi 10.1039/C2jm00120a (2012).

160 Chou, S. L. *et al.* Enhanced reversible lithium storage in a nanosize silicon/graphene composite. *Electrochemistry Communications* **12**, 303-306, doi:DOI 10.1016/j.elecom.2009.12.024 (2010).

161 Lee, J. K., Smith, K. B., Hayner, C. M. & Kung, H. H. Silicon nanoparticles-graphene paper composites for Li ion battery anodes. *Chem Commun* **46**, 2025-2027, doi:Doi 10.1039/B919738a (2010).

162 Wang, J. Z., Zhong, C., Chou, S. L. & Liu, H. K. Flexible free-standing graphene-silicon composite film for lithium-ion batteries. *Electrochemistry Communications* **12**, 1467-1470, doi:DOI 10.1016/j.elecom.2010.08.008 (2010).

163 Wong, D. P. *et al.* A stable silicon/graphene composite using solvent exchange method as anode material for lithium ion batteries. *Carbon* **63**, 397-403, doi:10.1016/j.carbon.2013.06.095 (2013).

164 Vickery, J. L., Patil, A. J. & Mann, S. Fabrication of Graphene-Polymer Nanocomposites With Higher-Order Three-Dimensional Architectures. *Advanced Materials* **21**, 2180, doi:DOI 10.1002/adma.200803606 (2009).

165 Zhang, H. F. *et al.* Aligned two- and three-dimensional structures by directional freezing of polymers and nanoparticles. *Nat Mater* **4**, 787-793, doi:Doi 10.1038/Nmat1487 (2005).

166 Zhou, X. S., Yin, Y. X., Wan, L. J. & Guo, Y. G. Facile synthesis of silicon nanoparticles inserted into graphene sheets as improved anode materials for lithium-ion batteries. *Chem Commun* **48**, 2198-2200, doi:Doi 10.1039/C2cc17061b (2012).

167 Obrovac, M. N. & Christensen, L. Structural changes in silicon anodes during lithium insertion/extraction. *Electrochem Solid St* **7**, A93-A96, doi:Doi 10.1149/1.1652421 (2004).

168 Liu, N. *et al.* A Yolk-Shell Design for Stabilized and Scalable Li-Ion Battery Alloy Anodes. *Nano letters* **12**, 3315-3321, doi:Doi 10.1021/Nl3014814 (2012).

169 Zhang, T. *et al.* Preparation and electrochemical properties of core-shell Si/SiO nanocomposite as anode material for lithium ion batteries. *Electrochemistry Communications* **9**, 886-890, doi:DOI 10.1016/j.elecom.2006.11.026 (2007).

170 Lee, D. U., Kim, B. J. & Chen, Z. W. One-pot synthesis of a mesoporous $NiCo_2O_4$ nanoplatelet and graphene hybrid and its oxygen reduction and evolution activities as an efficient bi-functional electrocatalyst. *J Mater Chem A* **1**, 4754-4762, doi:Doi 10.1039/C3ta01402a (2013).

171 Chen, C. M. *et al.* Macroporous 'bubble' graphene film via template-directed ordered-assembly for high rate supercapacitors. *Chem Commun* **48**, 7149-7151, doi:Doi 10.1039/C2cc32189k (2012).

172 Wang, Y. *et al.* Preventing Graphene Sheets from Restacking for High-Capacitance Performance. *J Phys Chem C* **115**, 23192-23197, doi:Doi 10.1021/Jp206444e (2011).

173 Allen, M. J., Tung, V. C. & Kaner, R. B. Honeycomb Carbon: A Review of Graphene. *Chem Rev* **110**, 132-145, doi:Doi 10.1021/Cr900070d (2010).

174 Wang, G. X. *et al.* Facile synthesis and characterization of graphene nanosheets. *J Phys Chem C* **112**, 8192-8195, doi:Doi 10.1021/Jp710931h (2008).

175 Wen, Z. H. *et al.* Silicon nanotube anode for lithium-ion batteries. *Electrochemistry Communications* **29**, 67-70, doi:DOI 10.1016/j.elecom.2013.01.015 (2013).

176 Kim, T., Mo, Y. H., Nahm, K. S. & Oh, S. M. Carbon nanotubes (CNTs) as a buffer layer in silicon/CNTs composite electrodes for lithium secondary batteries. *Journal of Power Sources* **162**, 1275-1281, doi:DOI 10.1016/j.jpowsour.2006.07.062 (2006).

177 Cui, L. F., Yang, Y., Hsu, C. M. & Cui, Y. Carbon-Silicon Core-Shell Nanowires as High Capacity Electrode for Lithium Ion Batteries. *Nano letters* **9**, 3370-3374, doi:Doi 10.1021/Nl901670t (2009).

178 Fransson, L., Eriksson, T., Edstrom, K., Gustafsson, T. & Thomas, J. O. Influence of carbon black and binder on Li-ion batteries. *Journal of Power Sources* **101**, 1-9, doi:Doi 10.1016/S0378-7753(01)00481-5 (2001).

179 Wang, G. X., Shen, X. P., Yao, J. & Park, J. Graphene nanosheets for enhanced lithium storage in lithium ion batteries. *Carbon* **47**, 2049-2053, doi:DOI 10.1016/j.carbon.2009.03.053 (2009).

180 Zhang, X. W. *et al.* Electrochemical performance of lithium ion battery, nano-silicon-based, disordered carbon composite anodes with different microstructures. *Journal of Power Sources* **125**, 206-213, doi:DOI 10.1016/j.jpowsour.2003.07.019 (2004).

181 Wang, W. & Kumta, P. N. Nanostructured Hybrid Silicon/Carbon Nanotube Heterostructures: Reversible High-Capacity Lithium-Ion Anodes. *Acs Nano* **4**, 2233-2241, doi:Doi 10.1021/Nn901632g (2010).

182 Lee, Y. M., Lee, J. Y., Shim, H. T., Lee, J. K. & Park, J. K. SEI layer formation on amorphous Si thin electrode during precycling. *J Electrochem Soc* **154**, A515-A519, doi:Doi 10.1149/1.2719644 (2007).

183 McArthur, M. A., Trussler, S. & Dahn, J. R. In Situ Investigations of SEI Layer Growth on Electrode Materials for Lithium-Ion Batteries Using Spectroscopic Ellipsometry. *J Electrochem Soc* **159**, A198-A207, doi:Doi 10.1149/2.004203jes (2012).

184 Kang, Y. M. *et al.* A study on the charge-discharge mechanism of $Co_3O_4$ as an anode for the Li ion secondary battery. *Electrochimica Acta* **50**, 3667-3673, doi:DOI 10.1016/j.electacta.2005.01.012 (2005).

185 Li, W. Y., Xu, L. N. & Chen, J. $Co_3O_4$ nanomaterials in lithium-ion batteries and gas sensors. *Adv Funct Mater* **15**, 851-857, doi:DOI 10.1002/adfm.200400429 (2005).

186 Boyano, I. *et al.* Preparation of C-$LiFePO_4$/polypyrrole lithium rechargeable cathode by consecutive potential steps electrodeposition. *Journal of Power Sources* **195**, 5351-5359, doi:DOI 10.1016/j.jpowsour.2010.03.029 (2010).

187 Nam, K. T. *et al.* Virus-enabled synthesis and assembly of nanowires for lithium ion battery electrodes. *Science* **312**, 885-888, doi:DOI 10.1126/science.1122716 (2006).

188 Binotto, G. *et al.* Synthesis, characterization, and li-electrochemical performance of highly porous $Co_3O_4$ powders. *Chemistry of Materials* **19**, 3032-3040, doi:Doi 10.1021/Cm070048c (2007).

189 Tummala, R., Guduru, R. K. & Mohanty, P. S. Binder free, porous and nanostructured $Co_3O_4$ anode for Li-ion batteries from solution precursor plasma deposition. *Journal of Power Sources* **199**, 270-277, doi:DOI 10.1016/j.jpowsour.2011.10.048 (2012).

190 Xia, X. H. *et al.* Self-supported hydrothermal synthesized hollow Co3O4 nanowire arrays with high supercapacitor capacitance. *Journal of Materials Chemistry* **21**, 9319-9325, doi:Doi 10.1039/C1jm10946d (2011).

191 Li, Y. G., Tan, B. & Wu, Y. Y. Freestanding mesoporous quasi-single-crystalline $Co_3O_4$ nanowire arrays. *Journal of the American Chemical Society* **128**, 14258-14259, doi:Doi 10.1021/Ja065308q (2006).

192 Wang, J. Q. *et al.* Porous $Co_3O_4$ nanoplatelets by self-supported formation as electrode Material for lithium-ion batteries. *Electrochimica Acta* **55**, 4805-4811, doi:DOI 10.1016/j.electacta.2010.03.048 (2010).

193 Wang, G. *et al.* Nickel Foam Supported-$Co_3O_4$Nanowire Arrays for $H_2O_2$ Electroreduction. *Chemistry of Materials* **21**, 5112-5118, doi:10.1021/cm901928b (2009).

194 Fu, Z. W., Wang, Y., Zhang, Y. & Qin, Q. Z. Electrochemical reaction of nanocrystalline $Co_3O_4$ thin film with lithium. *Solid State Ionics* **170**, 105-109, doi:DOI 10.1016/j.ssi.2004.02.020 (2004).